INDUCED SUPERCONDUCTIVITY IN TWO DIMENSIONAL ELECTRON GAS SYSTEM

A Dissertation

Submitted to the Faculty

of

Purdue University

by

Zhong Wan

In Partial Fulfillment of the

Requirements for the Degree

of

Doctor of Philosophy

June 2018

Purdue University

West Lafayette, Indiana

TABLE OF CONTENTS

Page

LIST OF FIGURES

Figure Page

Figure Page

ABSTRACT

Wan, Zhong , Purdue University, June 2018. Induced superconductivity in two dimensional electron gas system. Major Professor: Leonid Rokhinson.

Recently, interest in superconductor-semiconductor interfaces was renewed by the search for non-Abelian states. One of the possible platform is proximity induce superconductivity into an 1D semiconductor system with strong spin orbit (SO) interaction, such system is predicted to support Majorana excitation. Another candidate is superconductivity coupled to the edge of fractional quantum Hall state, in such system, higher order of non-abelian statistics is predicted. With such non-Abelian states, topological quantum computing can be realized. In this thesis, I'll discuss the approach made by us to investigate such system.

The thesis will begin with a brief review of superconducting proximity effect in semiconductor, including the study of Andreev reflection, multiple andreev reflection and current phase relation in a Josepheson junction. The second part of the introduction will focus on quantum Hall effect and fractional quantum Hall effect, the theoretical and experimental study of $\nu = 2/3$ edge states, and spin polarizations of the $\nu = 2/3$ state.

In chapter 2, I will discuss the the suprconducting proximity effect into a two dimensional electron system in GaAs, where variety of strongly correlated states including fractional quantum Hall effect can be observed. I present the procedure to form transparent superconducting contacts to high mobility two-dimensional electron gas (2DEG) in GaAs using a high critical field superconductor. Induced superconductivity across several microns is demonstrated and supercurrent in a ballistic junction is observed across 0.6 μm of 2DEG. High transparency of contacts are evaluated by measurements of the Andreev reflection at the superconductor/semiconductor interface. We also measured the magnetic field dependence of the critical temperature and transport behaviour of a superconductor in the quantum Hall

and fractional quantum Hall regime. The results shows modification of the Hall voltage at certain filling factors.

In chapter 3, I will discuss the experimental realization of the helical channel between incompressible spin polarized $\nu = 2/3$ and spin unpolarized $\nu = 2/3$. Gate control of spin transitions in the $\nu = 2/3$ regime allows formation of localized domain walls, which consist of counter-propagating edge states of opposite polarization with fractional charge excitations. These time reversal invariant nature of the domain walls can be confirmed by the non vanishing resistance under different direction of the perpendicular magnetic field. The evolution of the domain walls with gate voltage and magnetic field will be also discussed. The experimental realization of the helical channel in $\nu = 2/3$ allows us to further investigate the nature of FQHE, also enable the building of a potential platform of to realize high order non-Abelian exciatations.

In Chapter 4, I present our experimental investigation of S/N/S junctions in Al/InAs/Al system. With the advance of MBE techniques, a thin layer of superconducting Al can be epitaxially grown on top of InAs shallow 2D electron gas, which is a potential candidate for large scale top down approach of a topological quantum computer. Here, we report the fabrication of an InAs based superconducting quantum intereference device(SQUID),which consists of two Al/InAs/Al Josepheson junction(JJ). By using two different top gates, both junction can be tuned continuously from superconducting regime into insulating regime. From oscillations of critical current with external magnetic field, we can deduce that transport is the quasi-balistic through the junction over 150 nm separation of the junctions.

1. Introduction

The concept of a Josephson field effect transistor (JoFET) [1] sparked active research on proximity effects in semiconductors. Induced superconductivity and electrostatic control of critical current has been demonstrated in two-dimensional gases in InAs[2, 3], graphene[4] and topological insulators[5, 6, 7, 8, 9], and in one-dimensional systems[10, 11, 12] including quantum spin Hall edges[13, 14].

Majorana bound states have been proposed as possible building blocks for topological quantum computation. Recently, interest in superconductor-semiconductor interfaces was renewed by the search for Majorana fermions[15, 16], which were predicted to reside at the interfac between superconductor and 1D semiconductor with strong spin orbit interaction[17, 18, 19]. More exotic non-Abelian excitations, such as parafermions (fractional Majorana fermions)[20, 21, 22] or Fibonacci fermions may be formed when fractional quantum Hall edge states interface with superconductivity. By the utilization of these non-Abelian excitations, exotic circuit elements can be constructed[23, 24].

On the other had, the interplay between superconductivity and integer quantum Hall effect is also of interest. Despite the fact that both the superconductor and the quantum Hall fluid have zero resistance, the spin flipping process prohibits the Cooper-pairs injections from the superconductor to quantum Hall edge state. The tunneling current in the superconductor /quantum Hall fluid/superconductor junction is predicted to be significantly suppressed even for a highly transparent interface[25].

Proximity effects in GaAs quantum wells have been intensively investigated in the past and Andreev reflection has been observed by several groups[26, 27, 28, 29]. Unlike in InAs, where Fermi level (E_F) at the surface resides in the conduction band, in GaAs E_F is pinned in the middle of the gap which results in a high Schottky barrier between a 2DEG and a superconductor and low transparency non-ohmic contacts. Heavy doping can move E_F into the conduction band and, indeed, superconductivity has been induced in heavily-doped bulk n^{++} GaAs[30]. In quantum wells similar results were obtained by annealing indium contacts[31], however the critical field of indium is $\sim$ 30 mT which is well below the fields where quantum Hall effect is observed.

In the rest of the report, I will briefly introduce the theoretical background, including the Superconductivity as well as the interface between superconductor (section 1.1), the quantum Hall effect and the fractional quantum Hall effect (section 1.2). After that, I will discuss the experimental progress made by other groups.

1.1 Andreev reflection

Bardeen, Cooper and Schrieffer (BCS) formulated microscopic theory of in 1957 [32].They show that electrons with opposite wave vector and opposite spin can bound in pairs due to a weak attractive interaction . This interaction is mediated by electron-phonon coupling. Cooper pairs, which follow bosonic statistics, are condensed into the lowest energy state.

Lets consider the interface between a normal conductor and a superconductor. When an electron has energy $E < \Delta$, it cannot propagate into superconductor because there is no single particle state available in the gap. However, on the superconductor side instead of having a single particle excitation, a Cooper pair can be formed. Formation of a Cooper pair is compensated by taking an extra electron with vector $-k$ with an opposite spin from the filled Fermi sea in the normal metal side. Thus in the normal metal a hole is reflected with a wave vector $-k$. Note that the electron and the hole have opposite group velocities. The reflected hole follows the same path as the incident electron but in the opposite direction. This process is called Andreev reflection[33].

For $E > \Delta$ single particle states exist in the superconductor. In this regime, both normal electrons transmission and Andreev reflection are allowed. The consequence of the Andreev reflection is the enhancement of conductance since the backscattering of the electron is suppressed. In the ideal case of perfect transmission for $E < \Delta$ all electrons go through the Andreev reflection process and conductance is doubled compared to the case when $E > \Delta$.

Blonder-Tinkham-Klapwijk Model

Blonder, Tinkham, and Klapwijk (BTK) developed a model by using a single transparancy parameter Z to describe the Andreev reflection and normal reflection process at the interface of a normal-conductor/superconductor (N/S) [34] . In their model, shown in figure 1.1.1, a normal conductor ($x < 0$) and a superconductor ($x > 0$) are seperated by a barrier:

$$U_b(x) = \frac{\hbar^2 k_{\mathrm{F}}}{m_e} Z\delta(x) \tag{1.1.1}$$

where $k_{\mathrm{F}} = \sqrt{2m_e\mu/\hbar^2}$ is the Fermi wavevector in the superconductor, μ is the chemical potential. The dimensionless parameter Z describes the strength of the δ-function barrier. This transparency parameter Z is related to the transmission T by $Z = \frac{1}{\sqrt{1-T}}$ where $Z = 0$ corresponds to a completely transparent interface.

Quasiparticle states in this model can be described by the Bogoliubov-de Gennes (BdG) equations where quasiparticle excitations are described as a superposition of electron-like and hole-like excitations[35]. A plane wave solution of the BdG equation can be written as:

$$\begin{pmatrix} H(x) & \Delta \\ \Delta^* & -H(x) \end{pmatrix} \begin{pmatrix} u_k \\ v_k \end{pmatrix} = E \begin{pmatrix} u_k \\ v_k \end{pmatrix} \tag{1.1.2}$$

where $H(x)$ is a single particle Hamiltonian, and Δ is the superconducting gap. The wave functions consist of three components, the incident wave function ψ_{in}, the reflected wave function to the normal-conductor side ψ_r, and the transmission wave function ψ_t:

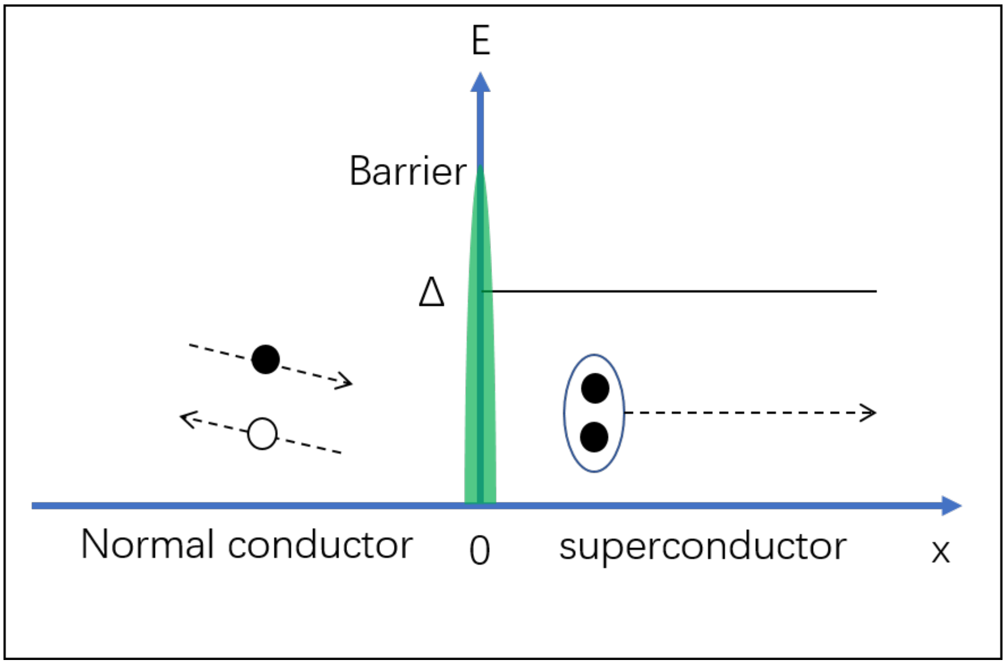

Figure 1.1.1. **Schematic illustration of BTK model.** The incident electron from normal metal travel across the interface between superconductor and normal metal. The formation of the cooper pairs in the superconductor are accompanied by the reflection of holes in the normal conductors.

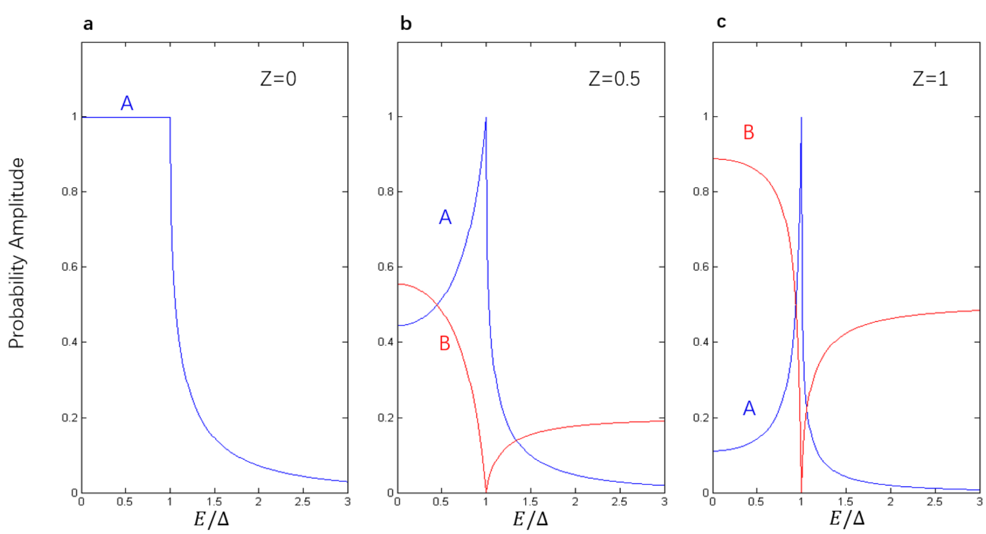

Figure 1.1.2. **Numerical calculation of the Andreev and normal reflection.**a, Andreev reflection for $Z = 0$ where B always equal to zero. b, Andreev reflection for $Z = 0.5$. c, Andreev reflection for $Z = 1$.

$$\begin{aligned}
\psi_{in} &= \begin{pmatrix} 1 \\ 0 \end{pmatrix} e^{(iq^+x)} \\
\psi_r &= a\begin{pmatrix} 0 \\ 1 \end{pmatrix} e^{iq^-x} + b\begin{pmatrix} 1 \\ 0 \end{pmatrix} e^{-iq^+x} \\
\psi_t &= c\begin{pmatrix} u_0 \\ v_0 \end{pmatrix} e^{ik^+x} + d\begin{pmatrix} v_0 \\ u_0 \end{pmatrix} e^{-ik^-x}
\end{aligned} \tag{1.1.3}$$

the +(-) sign denote the spin ↑ (↓), as can be seen from the wave function, the incoming wave function represent the incoming electron from the normal metal with spin ↑ and momentum $\hbar k$, the reflection wave function have two component, the reflection of the electron with momentum $-\hbar k$ and spin↑, as well as the reflection of the hole with momentum $\hbar k$ and spin ↓. The probability amplitudes for the transmission and reflections are:

$$\begin{aligned}
a &= \frac{u_0\nu_o}{\gamma} & A &= aa^* \quad \text{Andreev reflection ,} \\
b &= -\frac{u_0^2-\nu_0^2}{\gamma}(Z^2+iZ), & B &= bb^* \quad \text{normal reflection ,} \\
c &= \frac{u_0(1-iZ)}{\gamma}, & C &= cc^* \quad \text{transmission without branch-crossing,} \\
d &= \frac{i\nu_0 Z}{\gamma}, & D &= dd^* \quad \text{transmission with branch-crossing}
\end{aligned} \tag{1.1.4}$$

where, $\gamma = u_0^2 + (u_0^2 - \nu_0^2)Z^2$. Figure 1.1.2 shows the numerical calculation of A and B using 1.1.4. For $Z = 0$ when $E < \Delta$, all the incident electrons are Andreev reflected, while the normal reflection is suppressed. Differential resistance for different temperatures can be calculated using equation :

$$\frac{dI}{dV}(V) \propto \int_{-\infty}^{\infty} \frac{\partial f_0(E-eV)}{\partial(eV)}[1 + A(E) - B(E)]dE, \tag{1.1.5}$$

where $f_0(E)$ is the Fermi-Dirac function and $A(E)$ and $B(E)$ are energy-dependent Andreev and normal reflection coefficients, respectively. Both coefficients depend on the gap of the superconductor and the interface barrier strength Z. We use this model to analyze transparency of our contacts in chapter.2.

1.2 Previous work on superconductor/semiconductor junctions

Superconductor-semiconductor junctions have been extensively studied theoretically and experimentally, and early development are reviewed in the book[36]. Recent progress includes development of superconducting contacts to topological insulators[5, 6, 7, 8], one-dimensional systems[10, 11, 12] and quantum spin Hall edges[9, 13, 14].

Induced superconductivity and electrostatic control of critical current has been demonstrated in two-dimensional gases in InAs [2, 3, 37]. One of the advantages of InAs is that the Fermi level at InAs interface is pinned inside the conduction band, thus leading to an absence of a Schottky barrier. Therefore, transparent contacts can be formed between superconductors and InAs[38]. Recent experimental progress has enabled the growth of epitaxial layers of Al on 2D InAs/InGaAs quantum wells and forming transparent interfaces between Al and InAs [39]. Although InAs is a good candidate for hosting Majorana states due to its strong spin-orbit coupling, strain and dislocations due to the lattice mismatch in the InAs-based heterostructure result in low mobility compared to GaAs quantum wells, and no fully developed FQHE has been observed in InAs so far [40].

In graphene, induced superconductivity and the specular Andreev reflection has been observed[4]. Because of the chemical inertness of graphene, achieving transparent interfaces is relatively easy. Recently, fabrication of BN-capped high mobility graphene layers enabled observations of the FQHE in graphene [41]. However, due to the relatively high ($> 10T$) B field required to reach the FQHE regime, no experimental observation of the interplay between the FQHE and superconductivity has been published.

Theoretical work suggests that some non-Abelian excitations, such as parafermions (fractional Majorana fermions)[20, 21, 22] or Fibonacci fermions may be formed when fractional quantum Hall edge states interface with superconductivity. Thus, because of the possibility of the existence of these states, the proximity effect in GaAs has regained interest.

For GaAs, the most difficult part is to reduce the Schottky barrier. The Fermi level in GaAs is pinned in the middle of the gap which results in a high Schottky barrier between a

2DEG and a superconductor and low transparency non-ohmic contacts. The transparency of a superconductor/GaAs 2DEG interface depends crucially on fabrication technologies. In the following, I'll briefly review two general approaches to fabricate a SC/GaAs interface.

In reference[26] the Schottky barrier between the metal and GaAs is reduced by using Sn as superconducting contacts which act as shallow donor in GaAs. The oxide layer was removed by wet etching and an intermediate layer of Ti was deposited before the Sn deposition. After annealing, the resulting contact resistances were less than 10 Ω at $T = 80\ mK$ with a contact width of 10 μm. Transport measurements at low temperature show a signature of Andreev reflection. Although the measured contact resistance within the superconducting gap dropped less than a factor of two, the authors suggest that a series resistance contributes to the total resistance. On the other hand, the measured superconducting gap (10 μeV) is much smaller than the superducting gap of Sn (500 μeV at 80 mK). Further achievements were obtained by annealing indium contacts[31], where authors reduced the distance between the two superconducting contacts to $1\mu m$, and observed a supercurrent across the SC/SM/SC junction. Both Sn and In have small critical field ($< 100\ mT$) and cannot sustain fields required to the study of the IQHE or FQHE .

Another way to reduce the Schottky barrier is to introduce a doping layer between a high B_C superconductor and a semiconductor. In reference[29], the authors were able to form ohmic contacts between NbN and an AlGaAs/GaAs heterostructure by inserting an doping material between the two. After Ar plasma cleaning, a 50 nm AuGeNi was deposited on the surface then NbN was deposited on top. After annealing, an alloyed ohmic region was formed below the NbN and the contacts between NbN and GaAs were realized. Similarly, the transparency can be evaluated by the transport measurement across the junction. A clear decrease in the resistance within $V \sim \pm 5\ mV$ was observed. However, peak at $V = 0$ indicates a lower transparency compared to reference [26]. As a result, no supercurrent was observed in this work.

In summary, although the SC/SM interfaces have been extensively studied and various approaches have been tried, forming a transparent interface between a high-B_C superconductor and a high mobility GaAs quantum well has not been achieved. This inhibits the study of the interplay between the superconductor and strongly correlated states in the fractional quantum Hall regime.

1.3 Quantum Hall effect

In a classical two dimensional system, an electron can only move in the x-y plane. When an external magnetic field B is applied along the z-direction and current along the x-direction, a voltage difference in the y-direction is generated due to the Lorentz force. This voltage is referred to as the Hall voltage V_H. The Hall resistance is given by $R_H = \frac{V_{xy}}{I} \propto \frac{B}{ne}$. The longitudinal resistance is given by $R_{xx} = V_{xx}/I$.

The integer quantum Hall effect was first observed by Klaus von Klitzing in 1980[42]. When a strong magnetic field is applied perpendicular to a Si-MOSFET, by changing the gate voltage (which changes the density n), a Hall voltage is measured. It has been found that at certain gate voltages the Hall resistance is quantized, $R_H = \frac{h}{\nu e^2}$, where ν is a integer, and at the same time longitudinal resistance vanishes,$R_{xx} = 0$, see Figure1.3.1.

The quantum Hall effect takes roots in Landau quantization of energy spectrum in magnetic field. The Hamiltonian for the electron in the presence of a perpendicular magnetic field in the Landau gauge $\hat{A} = xB\hat{y}$ is:

$$H = \frac{1}{m^*}\hat{p}_x^2 + \frac{1}{m^*}(\hat{p}_y - qB\hat{x})^2, \tag{1.3.1}$$

where $\hat{p}$ is the momentum operator $\frac{i}{\hbar}\nabla$ and $\hat{A}$ is the electromagnetic vector potential. The eigenvalues of the Landau levels:

$$E_N = \hbar\omega_C(N + \frac{1}{2}), \tag{1.3.2}$$

where N is a positive integer, and $\omega_C = \frac{eB}{m^*}$ is the cyclotron energy, m^* is the effective mass of the electrons and B is the strength of the applied perpendicular magnetic field.

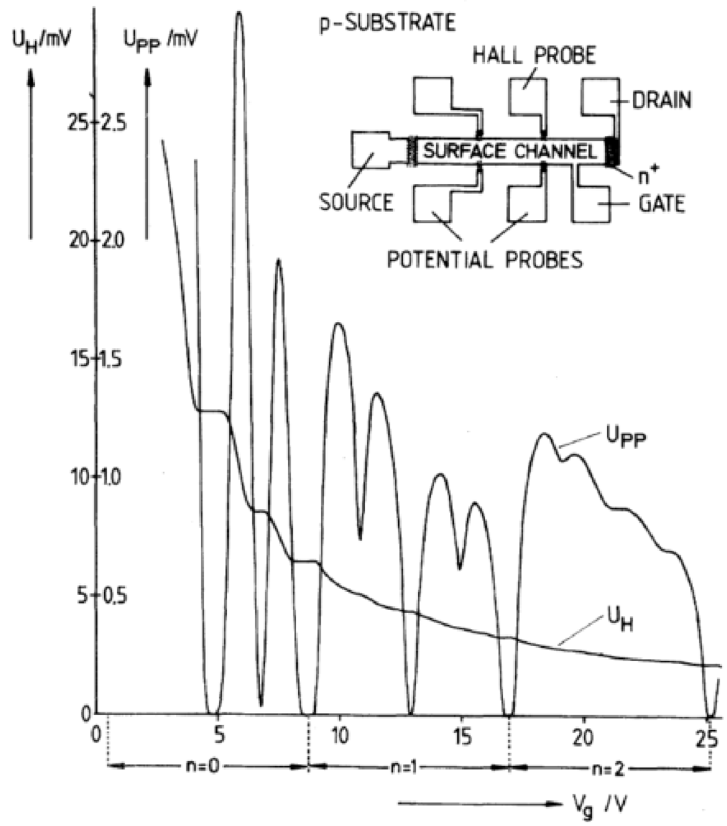

Figure 1.3.1. **The observation of integer quantum Hall effect.** In this case, the Fermi energy is tuned by changing the electron density. At certain values of the density, the Hall conductance is quantized and simultaneously, the longitudinal conductance vanishes. The Figure is taken from reference [42]

In reality, the broadening of the Landau level is the result of both temperature and disorder. Some of the states are localized by disorders due to the Anderson localization, but extended states are allowed and always preserved in the center of each Landau level [43, 44, 45], Figure 1.3.3. When the E_F is near the center of the Landau level where extended states are available, the Hall resistance is not quantized. When the Fermi energy is pinned in the region of localized states, a plateau in the Hall resistance is observed. Thus, the presence of a small but finite amount of disorder is crucial for the existence of quantized Hall effect.

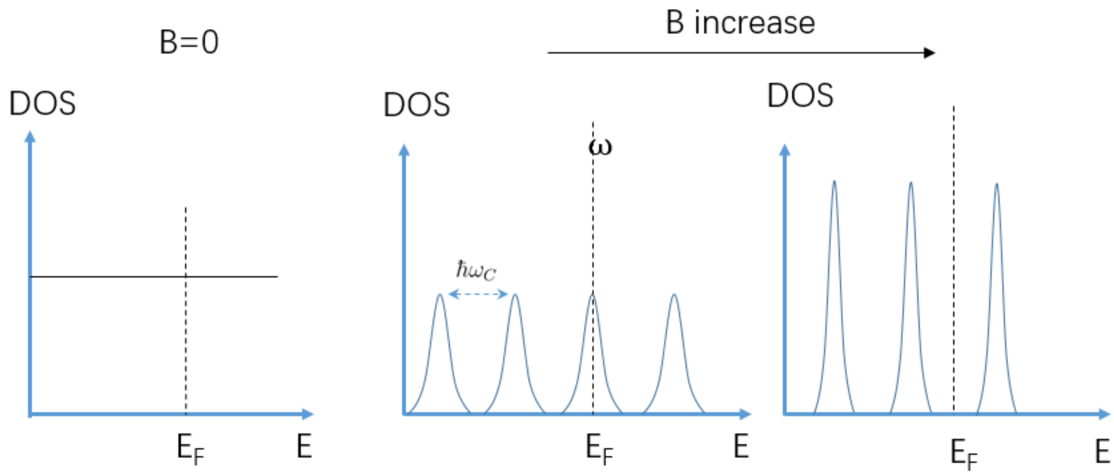

Figure 1.3.2. **Graphic depiction of quantized energy bands at different conditions.** with the presence of B field energy spectrum split in to higly degenerate Landau level. The seperation of the Landau level is $\hbar\omega_C$.

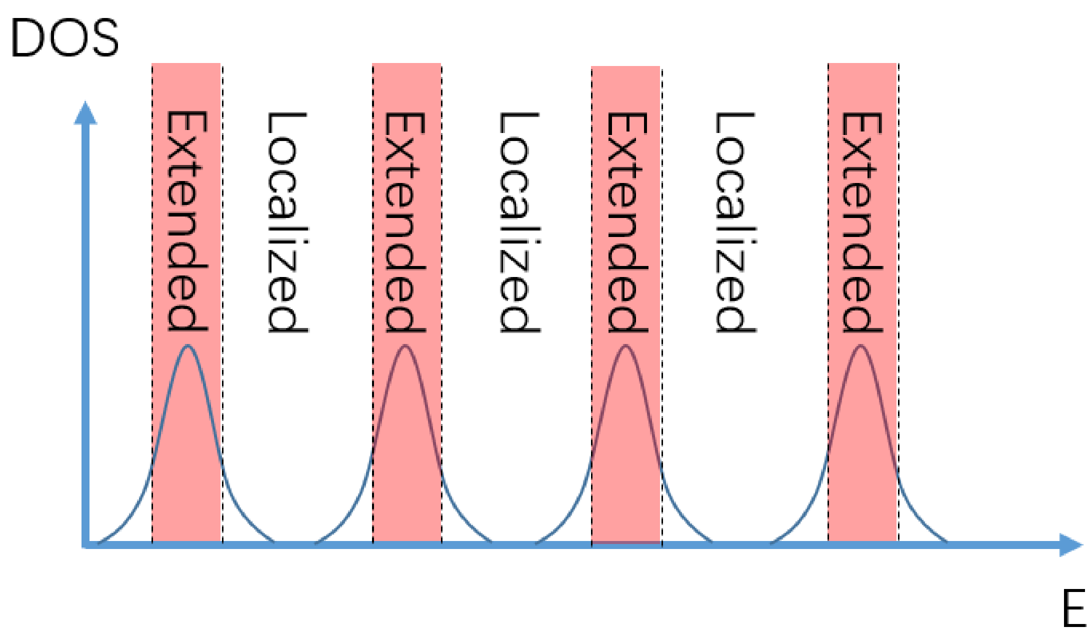

Figure 1.3.3. **Model for the explanation of the Hall plateaux.** Extended states are allowed in the center of each Landau level, while the states in the tails of each Landau level are localized.

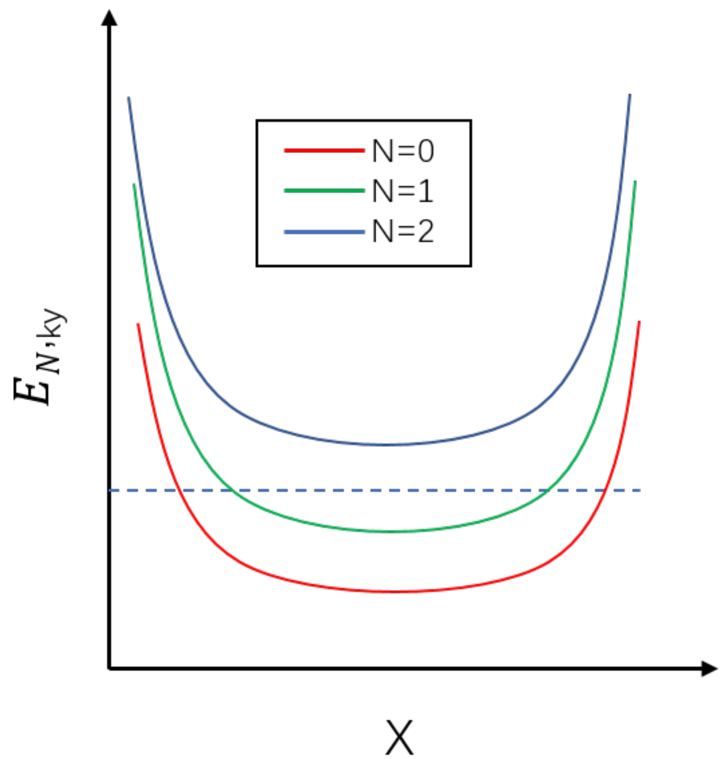

Figure 1.3.4. **Confining potential.**

Due to the impurity potential, mobility gaps are formed[45]. The mobility gaps are similar to the band gaps in a semiconductor but the DOS is non-zero. The wave functions of these states inside the mobility gaps are localized, and do not contribute to the conductance. Only when E_F moves close to the center of the Landau level are extended states allowed, and thus the conductance has a metallic behavior.

Alternatively, the measured quantized Hall resistance can be explained by only introducing the edge states [46]. With a finite sample size, there will be a confining potential at the edges of the sample. The number of edge states in the sample will be determined by the number of Landau levels below the Fermi energy E_F.

If one introduces a confining potential along the x-direction $U(x)$ as shown in figure1.3.4, the eigenvalue becomes :

$$E_{N,k_y} = (N + \frac{1}{2})\hbar\omega_c + \langle \Psi_{N,k_x} | U | \Psi_{N,k_x} \rangle. \tag{1.3.3}$$

In the lowest order perturbation theory, equation (1.3) can be written as

$$E_{N,k_y} = (N + \frac{1}{2})\hbar\omega_c + \langle \Psi_{N,k_y} | U | \Psi_{N,k_y} \rangle \approx (N + \frac{1}{2})\hbar\omega_c + U(x_0(k_y)) \tag{1.3.4}$$

and the velocity as

$$v_{N,k_y} = \frac{1}{\hbar}\frac{\partial U(x_0(k_y))}{\partial k_y} = \frac{1}{\hbar}\frac{\partial U(x_0(k_y))}{\partial x_0}\frac{\partial x_0}{\partial k_y} = \frac{c}{eB}\frac{\partial U(x_0)}{\partial x_0}. \tag{1.3.5}$$

On the edge of the mesa, the potential U is not uniform, which leads to the result $v_{N,k_y} > or < 0$ depending on the sign of dU/dx. In the middle of the mesa, in the simplest case, the potential is constant, which leads to $v_{N,k_y} = 0$ [47, 48].

The measured Hall resistance ρ_{xy} can be explained by the following: the Fermi energies between the source and drain are different: $E_{F_s} - E_{F_d} = -eV$. Therefore, the source has a higher Fermi wave-vector (hence a higher density) than the drain. The 1-D density of the extra electrons on the edge is

$$\delta n = \frac{1}{2\pi}\Delta k_F = \frac{1}{2\pi}\frac{eV}{|dE(k)|/dk} \tag{1.3.6}$$

where $dE(k)/dk = \hbar v_{\mathrm{F}}$. Then the current is:

$$I = -\delta n e v_{\mathrm{F}} = \frac{e^2}{2\pi\hbar}V = R_{Hall}^{-1}V. \tag{1.3.7}$$

Therefore a single channel carries a quantized conductace of e^2/h. Edge states in IQHE regimes have been used to study chiral 1D Luttinger liquid, and the edge states transports have been extensively studied in GaAs 2DEG using different geometries including Hall-bars, Corbino disks as well as Van der Pauw geometries. Transports in the IQHE regime can be modeled using the Landauer-Büttiker formalism. The voltage and current flow in the edge states follow 3 simple rules: 1. The potential of the downstream channel remains the same unless it is equilibrated by the contacts. 2. Each edge states in IQHE have conductance of $g_0 = 2e^2/h$. 3. The conservation of total charge.

In appendix A, one example of of the edge state potential is discussed. Same analysis is used in Chapter 4, where we use this method to distinguish between chiral edge states and helical edge states.

1.4 Fractional quantum Hall effect

Shortly after the discovery of the IQHE, the fractional quantum Hall effect (FQHE) was first observed in an AlGaAs/GaAs heterostructure by D. Tsui, H. Störmer and A. Gossard [49] (Figure 1.4.1). The Hall resistance shows plateaus in ρ_{xy} quantized to the values of $\frac{3h}{e^2}$ accompanied by a reduced ρ_{xx} at $\nu = 1/3$. After that, a large number of fractional quantum Hall states with different fractional filling factors were discovered. The discovery of the fractional quantum Hall states was unexpected since according to the IQHE picture there should be no energy gap below $\nu = 1$. However, the theory for the IQHE excludes electron-electron interactions which are essential for the FQHE. An instructive theory to understand FQHE was developed by Jain [50]. In this theory, an even number (2q) of vortices are bound to each electron forming a new quasiparticle (composite fermion) after vortex attachment transformation. In such a way, a strongly correlated electron system is mapped onto a weakly interacting system of composite fermions (CF). The composite fermions experience a reduced effective magnetic field B_{eff}:

$$B_{\text{eff}} = B_{\text{ext}} - 2n_e\phi_0 \tag{1.4.1}$$

where B_{ext} is the external magnetic field, n_e is the electron density, and $\phi_0 = \frac{h}{e}$ is the magnetic flux quanta.

More precisely, the effective magnetic field B_{eff} is obtained by determining the phase produced by a CF moving around a closed loop of area: $2\pi(\frac{B_{\text{ext}}A}{\phi_0} - 2N_{\text{flux}})$. The first term is the

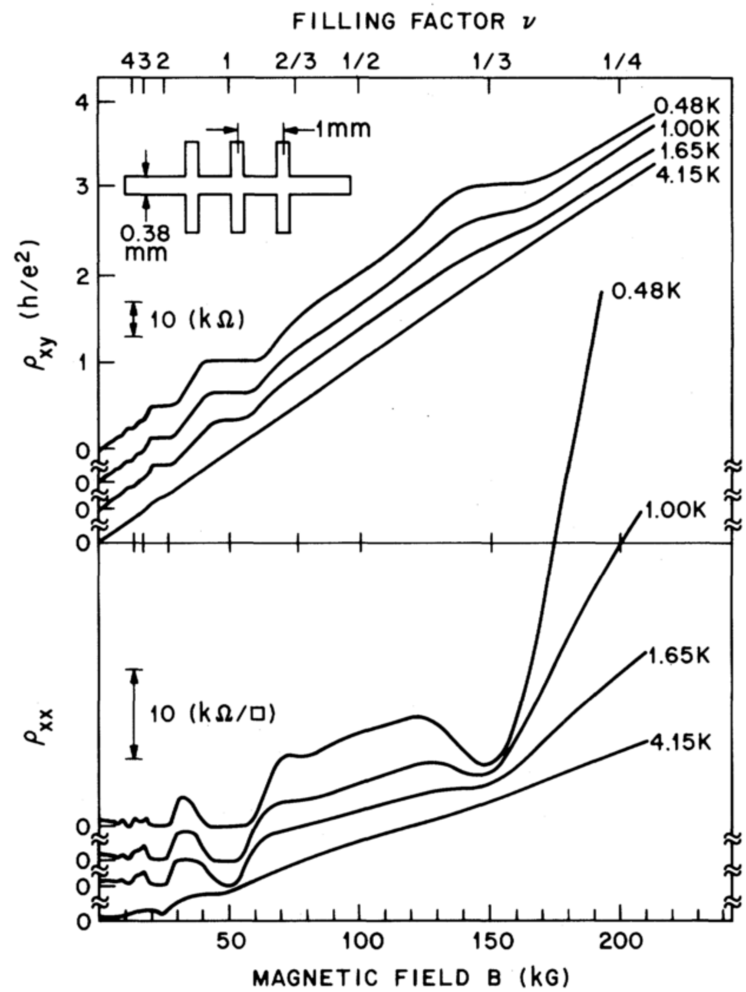

Figure 1.4.1. **The discovery of FQHE.** The fractional quantum Hall effect (FQHE) was first observed in an AlGaAs/GaAs heterostructure using a Hall-bar geometry. The Hall resistance shows plateaus in ρ_{xy} quantized to the values of $\frac{3h}{e^2}$ accompanied by a reduced ρ_{xx} at $\nu = 1/3$. Figure was taken from reference[49]

Aharonov-Bohm phase produced by the external magnetic field, and the second term is the phase produced by N_{flux} which is the number of flux quanta of the other composite fermions enclosed during the loop. In mean-field approach of the composite fermion theory[51], the flux quanta is "attached" to each of the composite fermion $N_{\text{flux}} = n_e A$. Like the Aharonov-Bohm phase, this new phase produced by other composite fermion can be added to the effective magnetic field, which will becomes equation 1.4.1.

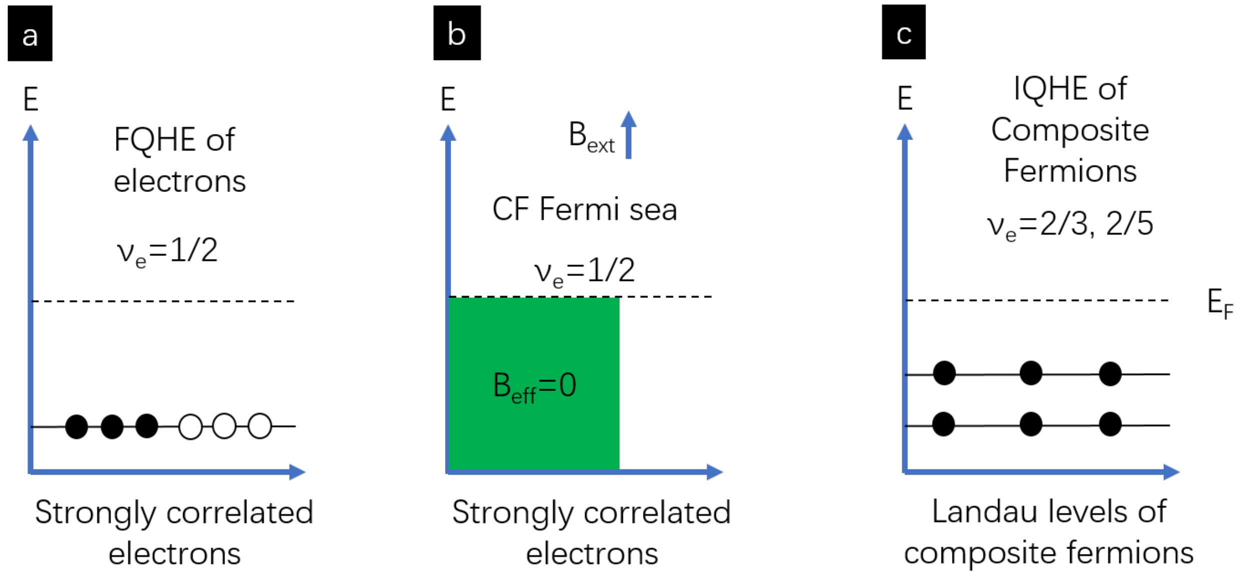

Figure 1.4.2. **Schematic illustration of the composite Fermion model.** Half filled Landau level in the picture of IQHE (a) is transformed into a composite Fermion sea (b) after the flux attachment transformation. When $B_{\text{eff}} \neq 0$, Landau levels of composite fermions are formed (c), resemblance of the case in IQHE.

As shown in figure 1.4.2, at $\nu = 1/2$ the $B_{\text{eff}} = 0$ and a Fermi sea of composite fermions forms [51, 52]. The Fermi wave vector is given by the following relation: $k_{\text{CF}} = (4\pi n_e)^{1/2}$ [53]. Away from $\nu = 1/2$ composite fermions experience non-zero B_{eff} and FQHE can be viewed as IQHE for composite fermions. The composite fermion filling factor can be obtained from the electron filling factor :

$$\nu = \frac{\nu_{\text{CF}}}{2\nu_{\text{CF}} \pm 1} \tag{1.4.2}$$

where the minus sign in the denominator corresponds to situations when B_{eff} is antiparallel to B.

Unlike its IQHE counterpart $\nu = 2$ states, where the edge states transports can be well described by Landau-Büttiker formalism, the edge states in $\nu = 2/3$ have a complicate structures. Theoretically, the edge states of $\nu = 2/3$ have several proposals, MacDonald proposed an edge structure composed of a pair of counter-propagating channels with a down

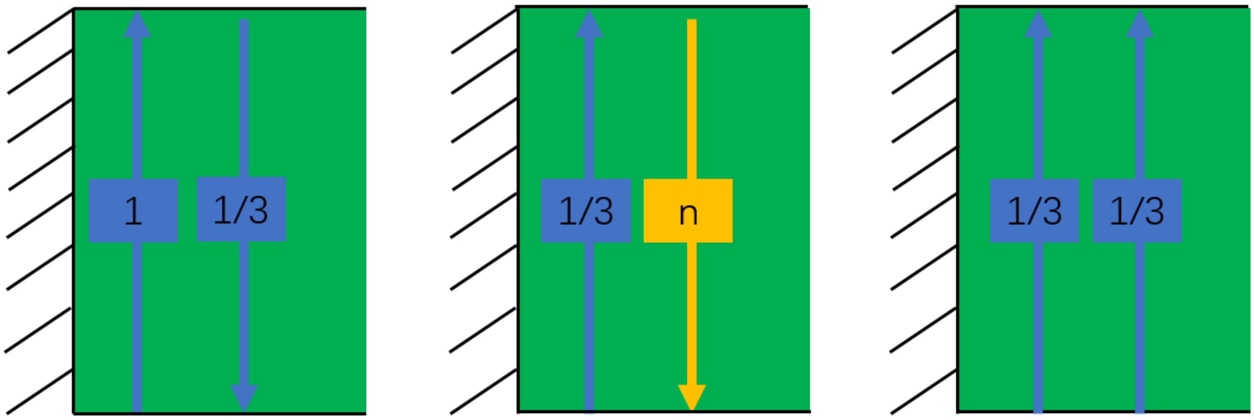

Figure 1.4.3. **Schematic illustration of the edge state construction in $\nu = 2/3$.** (a) edge states of $\nu = 2/3$ with a pair of counter propagating conducting channels, out edge have a conductance of $\frac{e^2}{h}$ and inner edge have a conductance of $-\frac{1}{3}\frac{e^2}{h}$. (b) edge states of $\nu = 2/3$ with a down stream conducting channel of $\frac{2}{3}\frac{e^2}{h}$ and a up stream neutral mode. (c) edge states of $\nu = 2/3$ with two down stream channels of $\frac{1}{3}\frac{e^2}{h}$.

stream conductance of $\frac{e^2}{h}$ and a upstream conductance of $-\frac{1}{3}\frac{e^2}{h}$[54]. This proposal is based on the fact that $\nu = 2/3$ state can be regarded as a hole conjugate state of $\nu = 1/3$ on top of $\nu = 1$. In this scenario, the two terminal resistance in Van-de-pauw geometry in $\nu = 2/3$ state should be $\frac{4h}{e^2}$. However, in experiments, no upstream electrical conductance is observed, nor a $\frac{4h}{e^2}$ resistance plateau is observed. Kane *et al*[55] proposed that after taking account of the inter-channel interaction and inter-channel scattering, a single downstream charge channel with $g = \frac{2}{3}\frac{e^2}{h}$ can be realized with an upstream neutral mode. Experimental observation of upstream thermal transport confirmed the existing of upstream neutral modes [56, 57]. Other proposals by Beenakker and Chang consisted of a pair of downstream edge channels, each with conductance $g = \frac{1}{3}\frac{e^2}{h}$ [58]. Recent experiments show that two co-propagating $\nu = 1/3$ charge modes exist at the edge of a sample. These two channel are weakly interacting and can be spatially separated [59].

The study of the edge state construction in $\nu = 2/3$ regime also invokes interest in studying the spin phase transition in the FQHE regime. Conventionally, if only the lowest

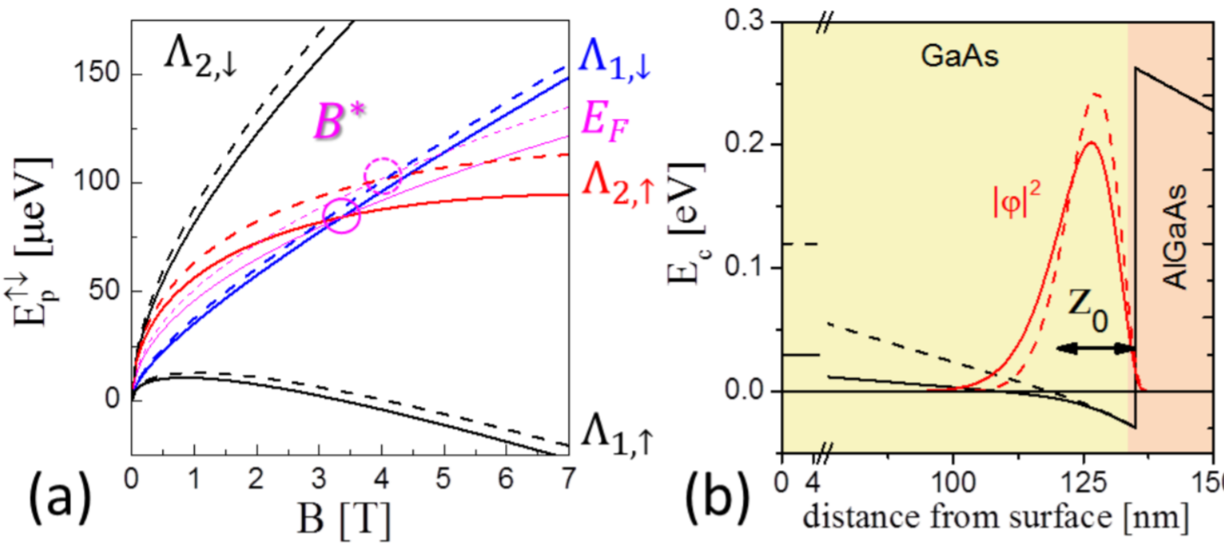

Figure 1.4.4. **Schematic illustration of the spin transition in $\nu = 2/3$.** (a)

spin-split LL is occupied by electrons (when $\nu \leq 1$), it is natural to assume that the spin degeneracy is lifted and the system is fully polarized. However due to the strong e-e interaction, the lowest energy charged excitations of the $\nu = 1$ quantum Hall state may have a complicate structure. Such excitations are called Skyrmion, which is extications that have spin down at the center and gradually turning up away from the center [60, 61, 62, 63]. Moreover, at all fractional filling factors except $\nu = 1/m$ states, ground states of different spin polarizations exist. Transitions between these states have been theoretically explained [64, 65]. Experimental work have been made using different technique, including the study of the activation gap [66, 67, 68], the study of photoexcitation [69] and the study of the electron spin and nuclear spin coupling via hyperfine interactions [70, 71, 72, 73].

Spin transitions in the FQHE regime can be readily understood within the framework of the theory of composite fermions [50], where FQHE states at filling factors $\nu = \frac{\nu^*}{(2\nu^* \pm 1)}$ for $1/2 < \nu < 1$ are mapped onto integer QHE states with a filling factor ν^* for CFs. The energy spectrum of CF Λ-levels with an index $p = 1, 2, 3...$ can be written as:

$$E_p^{\uparrow\downarrow} = \hbar\omega_c^{\mathrm{cf}}(p - \frac{1}{2}) \pm g\mu_B B \tag{1.4.3}$$

The composite fermion cyclotron energy $\hbar\omega_c^{\rm cf}$ is proportional to the charging energy:

$$E_c = \frac{e^2}{\sqrt{l_m^2 + z_0^2}} \tag{1.4.4}$$

where $l_m \propto \sqrt{B_\perp}$ is the magnetic length, $B_\perp = B\cos\theta$ is the out-of plane component of the magnetic field B, and z_0 is the extend of the wavefunction in the out-of plane direction. Due to the difference in B-dependences of the two terms, the composite fermions Landau level $\Lambda_{p,\downarrow}$ and $\Lambda_{p+1,\uparrow}$ cross at $B^* > 0$. Thus, in the composite fermion picture, for $\nu^* = 2$ the top energy level undergoes a spin transition at B^* and the $\nu = 2/3$ state is unpolarized for $B < B^*$ and fully polarized for $B > B^*$.

In GaAs, the electron reduced mass is much smaller than the free electron mass ($m^* = 0.067m_e$) and the effective g-factor is $g^* = -0.44$ instead of the free electron g-factor 2.03. Under these conditions, in the IQHE regime, the Zeeman energy E_Z is ≈ 60 times smaller that the cyclotron energy. Thus the lowest Landau level in the IQHE is expected be spin polarized. However, at several ground states of the FQHE, the Zeeman energy $\pm g\mu_B B$ of the composite fermion will be similar to the quasi-particle energies which depend on the exchange part of the Coulomb energy E_c. Thus, the favorable ground state depends on the interplay between the Zeeman and Coulomb energies, see figure 1.4.4.

As mentioned previously, studies on $\nu = 2/3$ states confirm the existance of the chiral edge state which can be spatially separated [59], also the ground state of $\nu = 2/3$ can undergo a spin phase transition [70]. Thus, a domain wall formed between two spin polarized domains can be formally constructed from two counterpropagating $\nu = 1/3$ chiral charge modes with opposite spin polarization at $\nu = 2/3$ spin transition, similar to the domain walls formation in the integer quantum Hall ferromagnetic transition [74].

2. Experimental investigation of the induced superconductivity in GaAs 2DEG

2.1 Heterojunction design and sample fabrication

In conventional quantum well structures AlGaAs barrier adds another 0.3 eV to the Schottky barrier if contacts are defused from the surface, while for side contacts exposed the AlGaAs layer increases surface density of pinning centers due to oxidation of aluminum. We alleviated these problems by growing an inverted heterostructure, where a 2D electron gas (2DEG) resides at the GaAs/AlGaAs interface but the AlGaAs barrier with modulation doping is placed below the 2DEG, see Figure 2.1.1. The inverted heterostructures have been use successfully inject cooper pair into InAlAs/InGaAs 2DEG system [3]. This design increase the contact area of side contacts compared to quantum well structures by utilizing all GaAs layer above the heterointerface for carrier injection (130 nm in our inverted heterostructure vs $20 - 30$ nm in typical quantum wells).

Superconducting contacts were patterned using standard electron beam lithography techniques. First, a 120 nm - deep trench was created by wet etching. Next, samples were dipped into HCl:H_2O ($1:6$) solution for 2 s and loaded into a thermal evaporation chamber, where Ti/AuGe (5nm/50nm) was deposited. Finally, 70 nm of NbN was deposited by DC magnetron sputtering in Ar/N_2 (85%/15%) plasma at a total pressure of 2 mTorr. The deposition conditions were optimized for producing high quality NbN films ($T_c = 11$ K and $B_c > 15$ Tesla with minimal strain[77]). The contacts were annealed at 500° C for 10 min in a forming gas. The measurements were performed in a dilution refrigerator with the base temperature < 30 mK, high temperature data was obtained in a variable temperature ^{3}He system.

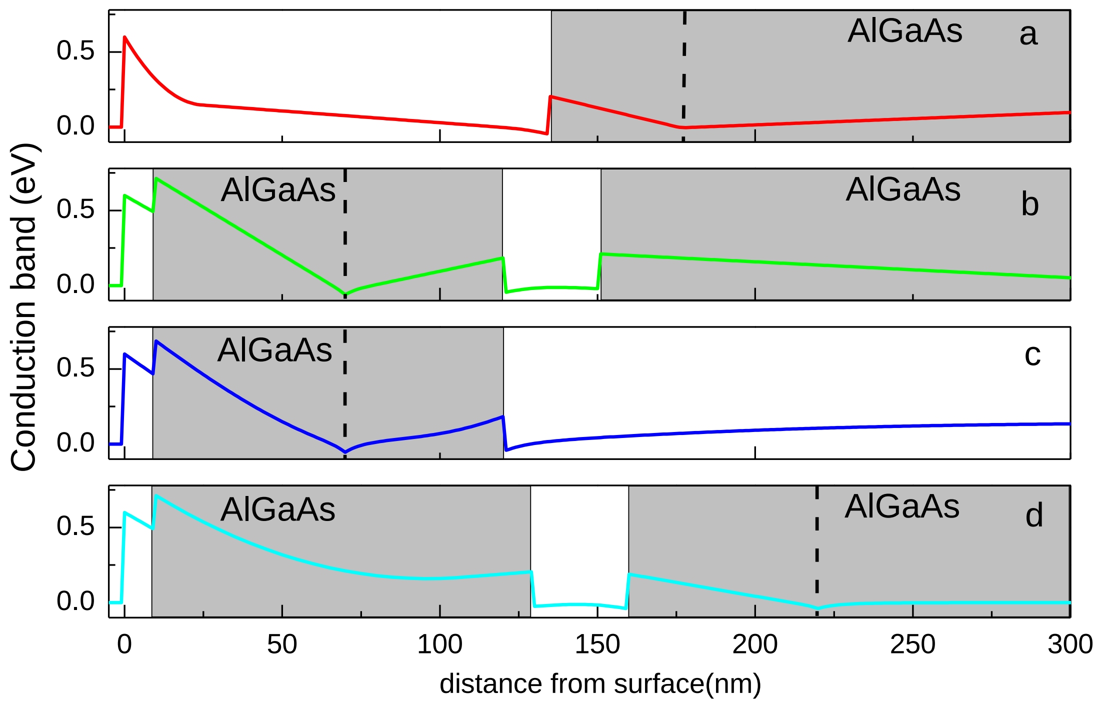

Figure 2.1.1. **Comparison between conventional heterostructure and inverted single interface heterojunction.** Conduction band profile is plotted for (a) inverted single interface heterojunction used in our experiments and typical (b) modulation-doped quantum well, (c) single heterojunction, and (d) inverted quantum well. Dash lines indicate position of modulation doping.

The induced superconductivity was observed in two devices from different wafers LE23 and LE25. The detailed infromation about the wafer are shown in Appendix A. Sample A is fabricated from wafer LE23 and has long (70 μm) contacts separated by 1.6 μm of 2DEG, for sample B contacts are formed to the edge of a mesa with 0.6 μm separation.

When cooled down to 4 K in the dark both samples show resistance in excess of 1 MΩ. After illumination with red light emitting diode (LED) a 2DEG is formed and 2-terminal resistance drops to $< 500\Omega$. As shown in Figure 2.1.2d sample resistance R^B_{3-4} gradually decreases upon cooldown from 4 K to the base temperature and the S-2DEG-S junctions becomes superconducting at $T_c \sim 0.3$ K.

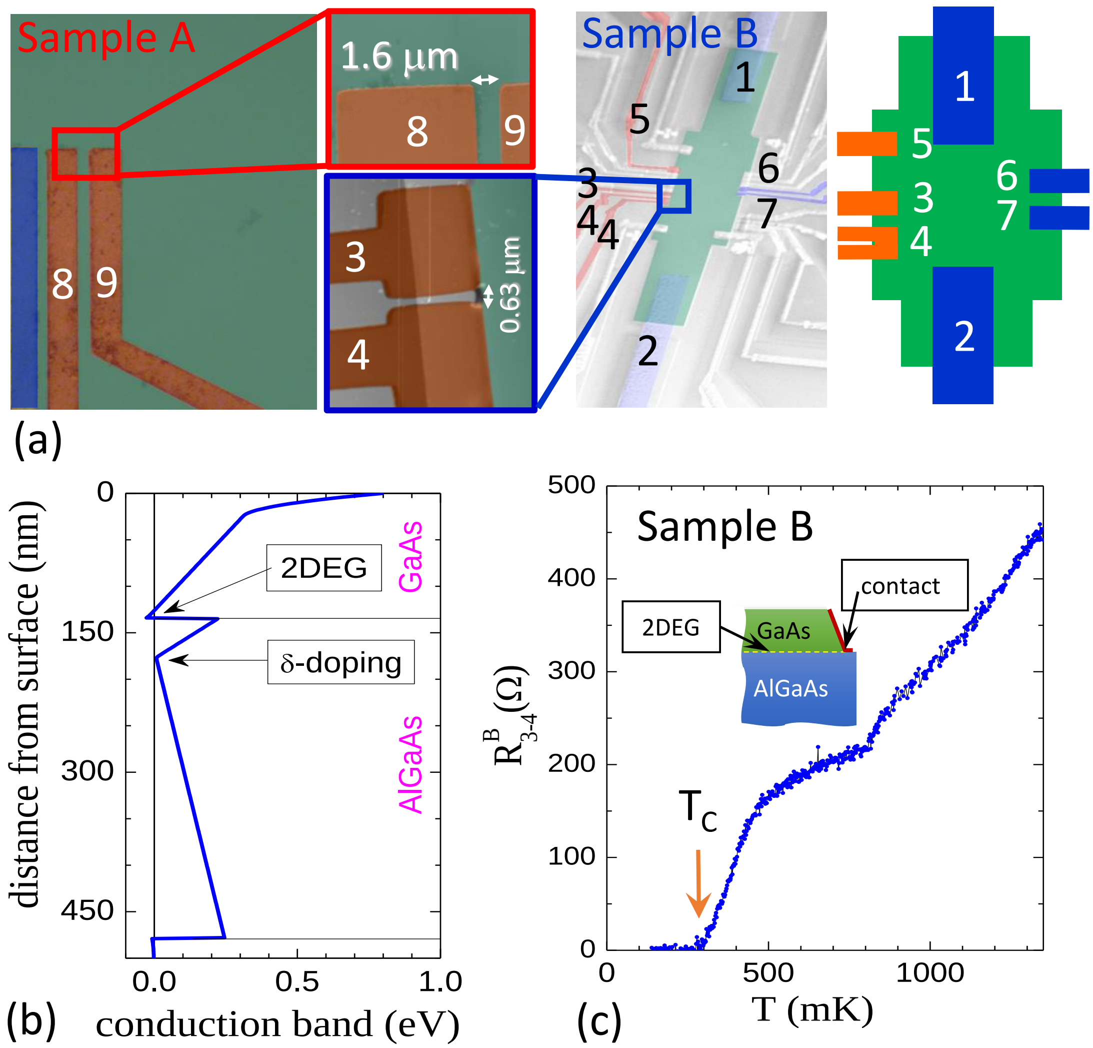

Figure 2.1.2. **Devices design and superconducting transition.** (a) Scanning electron microscope (SEM) images of test devices similar to samples A and B. Enlarged region for sample B is an atomic force microscope (AFM) image of a real sample. 2D gas regions are false-color coded with green, superconducting and normal contacts are coded with orange and blue, respectively. (b) Simulation of the conduction band energy profile in the heterostructure[75, 76]. (c) T-dependence of resistance between contact 3 and 4 in Sample B measured with 10 nA ac excitation. Superconducting transition is observed at $T_c \approx 290$ mK.

2.2 Voltage-current characteristics for superconducting junctiong

Voltage-current $V(I)$ characteristics for two S-2DEG-S junctions (contacts 8-9 for sample A and between 3-4 for sample B) are shown in Figure 2.2.1. Both samples show zero

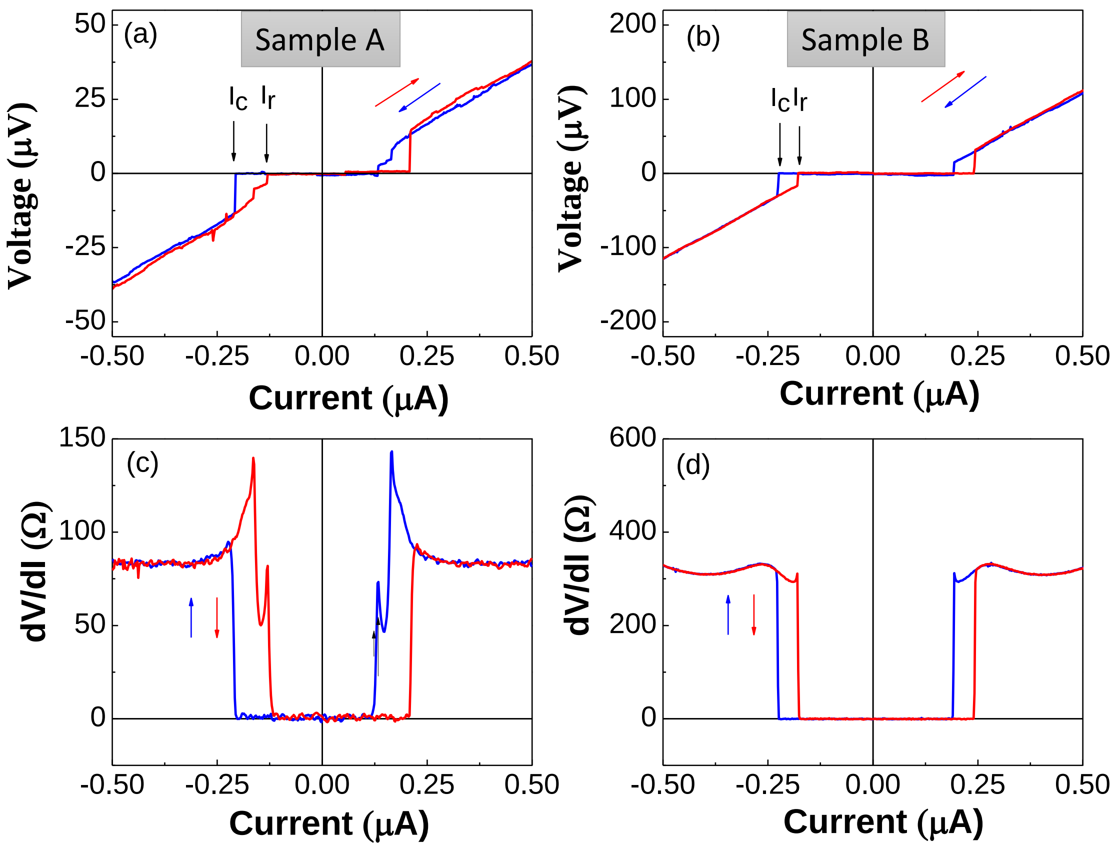

Figure 2.2.1. **Induced superconductivity in a high mobility 2D electron gas in GaAs.** Voltage-current characteristics and differential resistance are measured between 8-9 for sample A and between 3-4 for sample B at base temperature , dV/dI is measured with $I_{ac} = 1$ nA. Induced superconductivity with zero voltage is observed with critical currents $I_c \sim 220$ nA for sample A and $I_c \sim 230$ for sample B.

resistance state at small currents with abrupt switching into resistive state at critical currents $I_c = 0.22$ μA and 0.23 μA for samples A and B respectively. $V(I)$ characteristics are hysteretic most likely due to the Joule heating in the normal state.

The most attractive property of a high mobility 2DEG is large mean free path $l \gg \xi_0$. Here in sample B, $l = v_F \mu m_e/q = 24$ μm. The BCS coherence length is $\xi_0 = \hbar v_f/\pi\Delta = 0.72$ μm. Here $v_f = \hbar\sqrt{2\pi n}/m$ is the Fermi velocity, $n = 1.3 \cdot 10^{11}/cm^2$ is a 2D gas density for wafer LE25, $m = 0.063 m_e$ is the electron effective mass in GaAs, and $\Delta = 1.76 k_B T_C = 46$ μeV is the induced superconducting gap. Evolution of $V(I)$ with T is shown Figure 2.3.1a.

Experimentally obtained T-dependence of I_c is best described by the Kulik-Omelyanchuk theory for ballistic junctions ($L \ll l$)[78], the blue curve on Figure 2.3.1b. For comparison we also plot $I_c(T)$ dependence for the dirty limit $L \gg \sqrt{l\xi_0}$ [79], which exhibits characteristic saturation of I_c at low temperatures.

In short ballistic junctions $L \ll \xi_0 \ll l$ the product $I_c(0)R_N = \pi\Delta/e$ does not depend on the junction length L. For $L \sim \xi_0$ this product is reduced by a factor $2\xi_0/(L + 2\xi_0)$ [80]. In our experiment, the junction length $L = 0.63$ μm, mean free path $l = 24$ μm and BCS coherence length $\xi_{\ 0} = 0.72\mu m$. therefore $L \sim \xi_0 \ll l$, theoretically estimated $I_cR_N = \pi\Delta/e \cdot 2\xi_0/(L + 2\xi_0) = 90$ μV. The measured $I_cR_N = 83$ μV for sample B is in a good agreement with an estimate For sample A the $I_cR_N = 19$ μV while the estimated product is ≈ 50 μV. We speculate the reduction is related to the geometry of sample A, where a region of the 2DEG with induced superconductivity is shunted by a large region of a 2DEG in a normal state.

2.3 Transparency of the junction

2.3.1 Temperature dependence of the critical current

Transparency of superconducting contacts can be estimated from the suppression of the superconducting gap in the S-2DEG-S junction. Haberkorn et al.[81] generalized Kulik-Omelyanchuk current-phase relations[78, 79] to the case of arbitrary transparency of a tunnel barrier D inserted into the Josephson junction by directly solving Gor'kov's equations. They obtain the following current-phase relation:

$$I_s(\phi, T)R_N = \alpha\frac{\pi\Delta(T)}{2e}\frac{\sin(\phi)}{\sqrt{1 - D\sin^2(\phi/2)}}\tanh\frac{\Delta(T)}{2k_BT}\sqrt{1 - D\sin^2(\phi/2)}, \qquad (2.3.1)$$

where $\Delta(T)$ is the BCS gap. For $\alpha = 1$ this equation interpolated between diffusive ($D = 0$) and ballistic ($D = 1$) junctions. Critical current can be found as $I_c(T)R_N = max[I_s(\phi, T)R_N]$. Coefficient α is introduced to account for the reduction of the critical

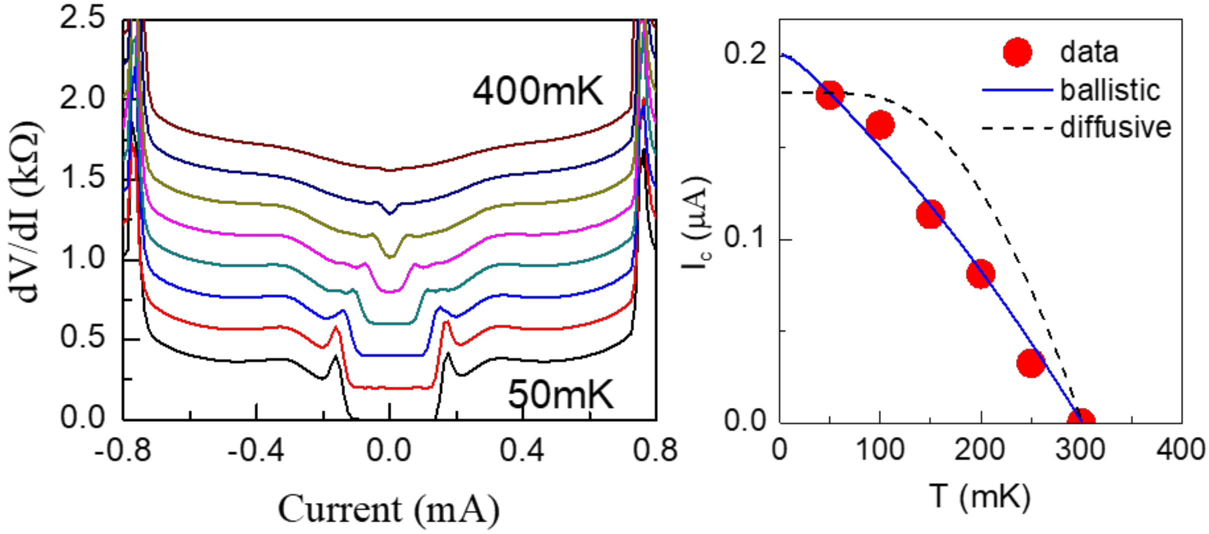

Figure 2.3.1. **Temperature dependence of superconductivity in a ballistic junction.** (a) Evolution of the induced superconductivity with T for sample B. The $R(I)$ curves are offset proportional to T for $T > 50$ mK. (b) Temperature dependence of critical current $I_c(T)$ is extracted from (a) and compared to the expected T-dependence for ballistic and diffusive regimes (reduced I_c compared to Figure 2.2.1 is due to larger $I_{ac} = 10$ nA used in this experiment).

current due to the finite length of the junction L, $\alpha = 2\xi/(L + 2\xi)$ [80]. The best fit of the experimental $I_cR_N(T)$ dependence assuming both α and D as free parameters is obtained for $D = 1(Z = 0)$ and $\alpha = 0.7$, see Figure 2.3.2(a,b). For the contact spacing $L = 0.63$ μm this α corresponds to $\xi = 0.76$ μm, consistent with the BCS coherence length $\xi_0 = \hbar v_f/\pi\Delta = 0.72$ μm. And the fit sets the upper limit on Z, $Z < 0.1$. The quality of the fit parameters can be assessed from Figure 2.3.2(c), where rms error for the best fit with a fixed D and α as a free parameter (rms deviation)$^2 = \sum_i \{[I_c(T_i)R_N]^{theory} - [I_c(T_i)R_N]^{exp}\}^2$ is plotted for different D. The rms deviation has a clear global minimum at $D \to 1$. Note that the coherence length for $D < 1$, obtained from the fitting parameter α, becomes smaller than the estimated ξ_0.

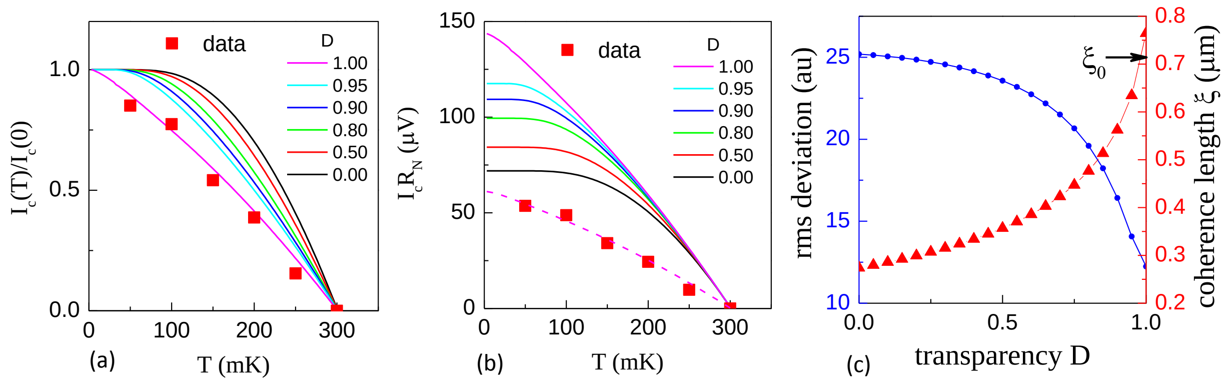

Figure 2.3.2. **Analysis of the temperature dependence of the critical current.** Scaled (a) and unscaled (b) product I_cR_N is calculated using Eq. (2.3.1) for different transparencies D and $\alpha = 1$. Red dots are experimental data. Dashed line in (b) is for $\alpha = 0.7$ and $D = 1$. In (c) root-mean-square deviation between the best fit and the experimental data is shown for different D, coherence length ξ obtained from the best fit are red triangles.

The voltage dependence of the differential resistance are shown in figure 2.3.3, here differential resistance are measured in different field at $T = 50\ mK$ as well as at high temperature $T = 13\ K$ with zero field. At base temperature with zero B field, we observed several resistance peak. For the largest 6 peaks, they are located at $V = \pm 2\ mV, \pm 4\ mV, \pm 6\ mV$, with $\Delta V = 2mV$. These resonances are also observed in $I(V)$ characteristics of a single S-2DEG interface (measured in the S-2DEG-N configuration between contacts 3-6, see Figure 2.3.4). Similar sharp resonances has been observed previously [82, 83]. In reference [82] where authors attributed their appearance to the formation of Fabry-Pérot resonances between superconducting contacts. However differential resistance does not change substantially across resonances, ruling out transport through a localized state. In reference [83], author suggest that those resistance peak are related to McMillan-Rowell like oscillations (MRO) [84], with $\Delta V = hv_f/4ed$ where d is the distance of the normal region. Typically, MRO occurs in a S/N/I junction, where Andreev bound state can have several coherence reflection between N/I interface. In our system, due to the highly transparent S/N interface with minimal normal reflection, MRO should not happen. Also, with our junction parameter, the calculated $\Delta V = 3.1mV$, this does not match the measured $\Delta V = 2\ mV$. We speculate

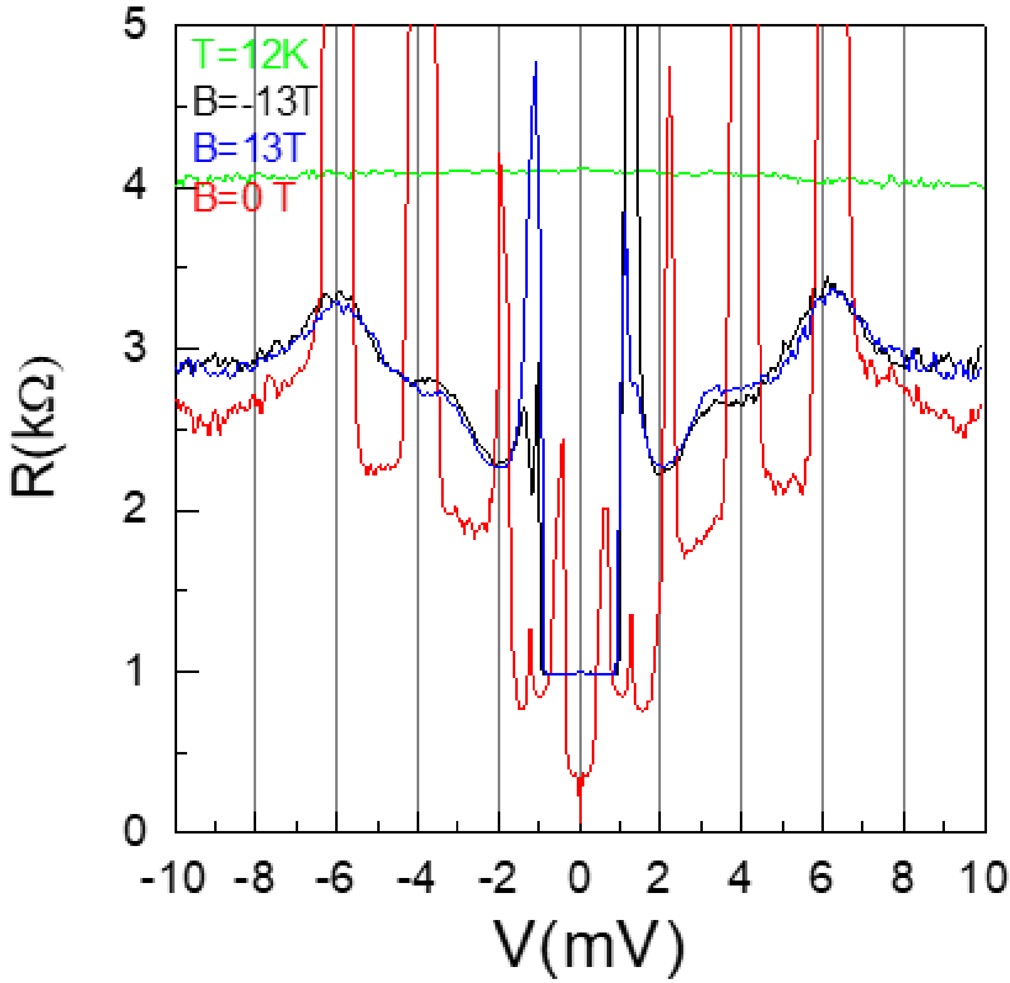

Figure 2.3.3. **Voltage dependent of the differential resistance.** Differential resistance as a function of applied voltage bias. Red, blue, black, resistances measured at $T = 50\ mK$ at B=0,B=13 T, B=-13 T, respectively. Green, resistances measured at 13 K at zero field.

that in the contacts where these resonances are observed superconductivity is carried out by quasi-1D channels, and jumps in I/V characteristics are due to flux trapping at high currents. This scenario is consistent with the observation that peaks shift to lower currents at higher fields, see Figure 2.4.1. Within the superconducting gap of NbN (V=1.8 mV), further resistance drop are observed. We attribute this reduction to the multiple Andreev reflection between two closely-spaced contacts, for contacts with larger separation ($20\mu m$) multiple Andreev reflection is suppressed and the reduction of resistance by a factor of 2 is observed, see Figure 2.3.4. Another feature is the Andreev reflection measured at high field. Although no supercurrent is observed when $B > 0.2\ T$, andreev reflection still remain up to 13 T. This is indicated by the blue and black lines in figure 2.3.3, at $V = 0.9\ mV$ a factor of 2 reduction of resistance is observed. The field dependent of the superconductin gap $\Delta_B = \Delta_0\sqrt{1-(\frac{B}{B_0})^2} = 0.9mV$, where $B_0 = 15T$ is the critical field of NbN. When $B = 13\ T$, $V = 0.9\ mV$. Both the reduction and the voltage matches the theoretically calculated value. This suggest that Andreev states exist at high field and transparency of the contacts is also preserved, which allows us to study the interplay between SC and FQHE.

2.3.2 Analysis of excess current above the induced superconductivity gap

In one-dimensional junctions the induced gap $\Delta = \Delta_0\frac{\Gamma}{\Gamma+\Delta_0}$ depends on the broadening of Andreev levels within the semiconductor[85] $\Gamma = \frac{\hbar v_f}{L_{eff}}D_1D_2$, contacts transparencies D_1 and D_2 are introduced. We assume for simplicity that $D = D_1 = D_2 = 1/(1+Z^2)$, where $0 < Z < \infty$ is a interface barrier strength introduced in section 1.1, and Bagwell's effective channel length $L_{eff} = L + 2\xi_0$[80]. Transparency of the superconductor-semiconductor interface can be estimated from the shape of the $dV/dI(V)$ characteristic, where competition between Andreev and normal reflections results in a peak in differential resistance when a tunneling barrier is present at the superconductor-semiconductor interface. Differential resistance for different temperatures can be calculated using BTK theory introduced in section 1.1. Both Andreev and normal reflection coefficients depend on the gap of NbN $\Delta_0 = 2.02k_BT_C^0$ with $T_c^0 = 11$ K and the interface barrier strength Z. In Figure. 2.3.4 we plot differential resistance for different values of Z. At low T for $Z = 0$ the barrier is transparent ($D = 1$) and all incident electrons are Andreev reflected, which leads to the a reduction of differential resistance by a factor of 2 within the energy gap Δ_0. When Z is finite, part of the incident electrons undergoes normal reflection which results in the increase of the resistance within the gap.

Similar values of Z can be estimated from the analysis of the shape of $dI/dV(V)$ characteristics at elevated temperatures, as shown in Figure 2.3.4. At $T < T_c^0$ Andreev reflection at S-2DEG interfaces results in an excess current flowing through the junction for voltage biases within the superconducting gap Δ_0/e and corresponding reduction of a differential resistance dV/dI by a factor of 2. In the presence of a tunneling barrier normal reflection competes with Andreev reflection and reduces excess current near zero bias, resulting in a peak in differential resistance. Within the BTK theory a flat $dV/dI(V)$ within Δ_0/e, observed in our experiments, is expected only for contacts with very high transparency $Z < 0.2$. For larger $Z > 0.2$ a peak at low biases is expected.

The exact shape of experimental curves differ from the shape predicted by the BKT theory, the most important deviation being sharp minima near $V = 0$ observed at T close to T_c^0 as compared to a much smoother BKT dependence. To account for a similar sharpening of a zero-bias peak in less transparent contacts ($Z > 2$) it has been assumed that a thin normal region is formed between NbN contacts and a 2DEG[86]. This more elaborate theory introduces two more fitting parameters for the superconducting-normal and normal-2DEG interfaces, but does not change the main qualitative prediction of a simpler BTK theory: appearance of a peak near $V = 0$ for $Z > 0.2$ in $dV/dI(V)$ characteristics.

Experimentally, we observe no zero-bias peak in $dV/dI(V)$ characteristics measured between two superconducting contacts R_{3-4} (S-2DEG-S) or between superconducting and normal contacts R_{8-9} (S-2DEG-N), see figure 2.3.4, thus we can set an upper limit $Z < 0.2$ and lower limit $D > 0.96$ for our contacts.

2.4 B field dependence of the induced superconductivity

Finally, we present magnetic field dependence of induced superconductivity. The low-field data is shown in Figure 2.4.1a,b, where black regions correspond to zero differential resistance. Induced superconductivity is suppressed at ≈ 0.2 T in both samples. In sample A a narrow region of a 2DEG with induced superconductivity is confined between large NbN

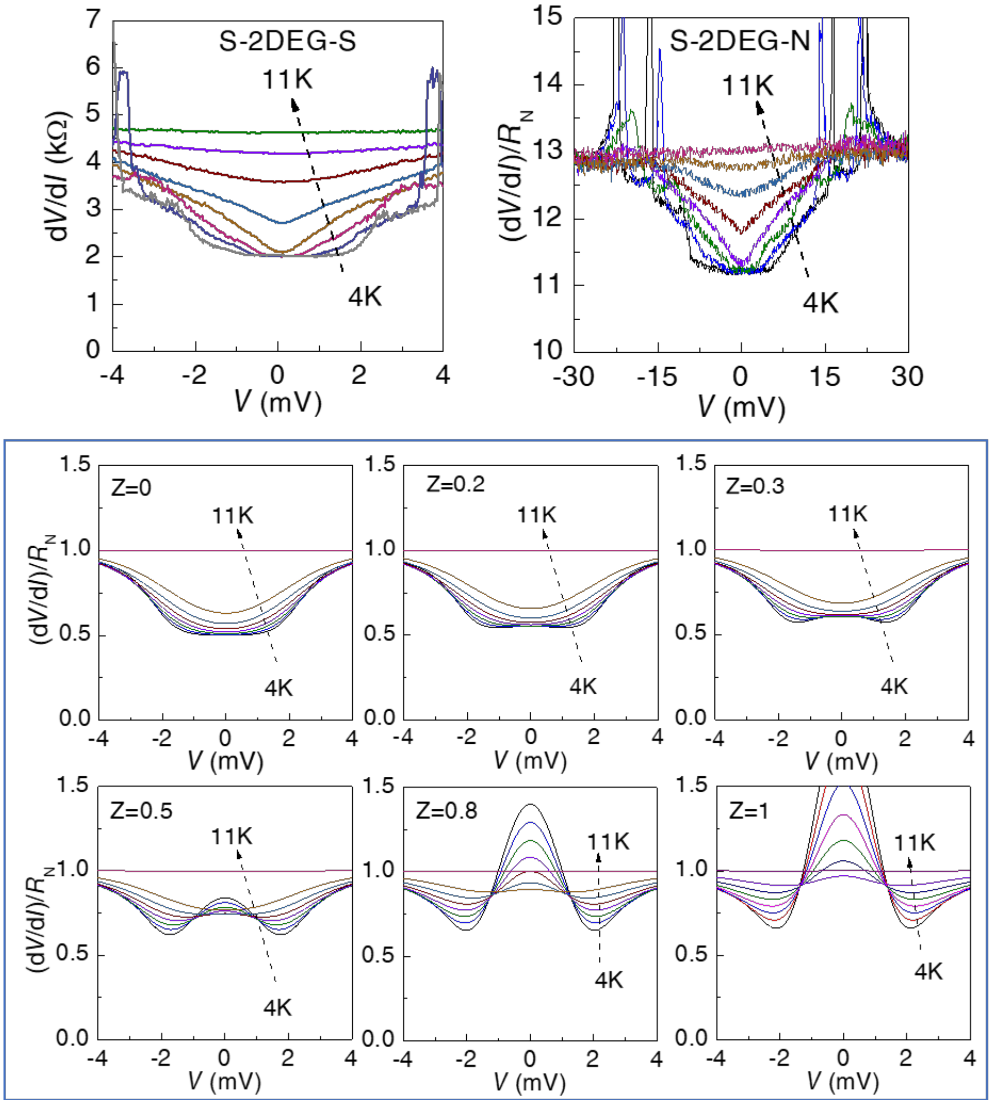

Figure 2.3.4. **Temperature dependence of differential resistance.** Left 6 plots: normalized differential resistance is calculated using BKT theory, Eq. 1.1.5 for different barriers Z and temperatures between 4 and 11 K with a step of 1 K. Right 2 plots: experimentally measured differential resistance between two superconducting contacts (R_{3-5}) and a normal-superconducting contact (R_{4-7}) in sample B (the normal contact has high resistance).

superconducting leads with rigid phases. Perpendicular magnetic field twists the phase in the 2DEG resulting in Fraunhofer-like oscillations of the critical current. In this sample, though, the 2DEG extends beyond the narrow region between the contacts, therefore I_c does not decrease to zero, at the node point around 0.15 mT and 0.9 mT. Abrupt jumps in I_c

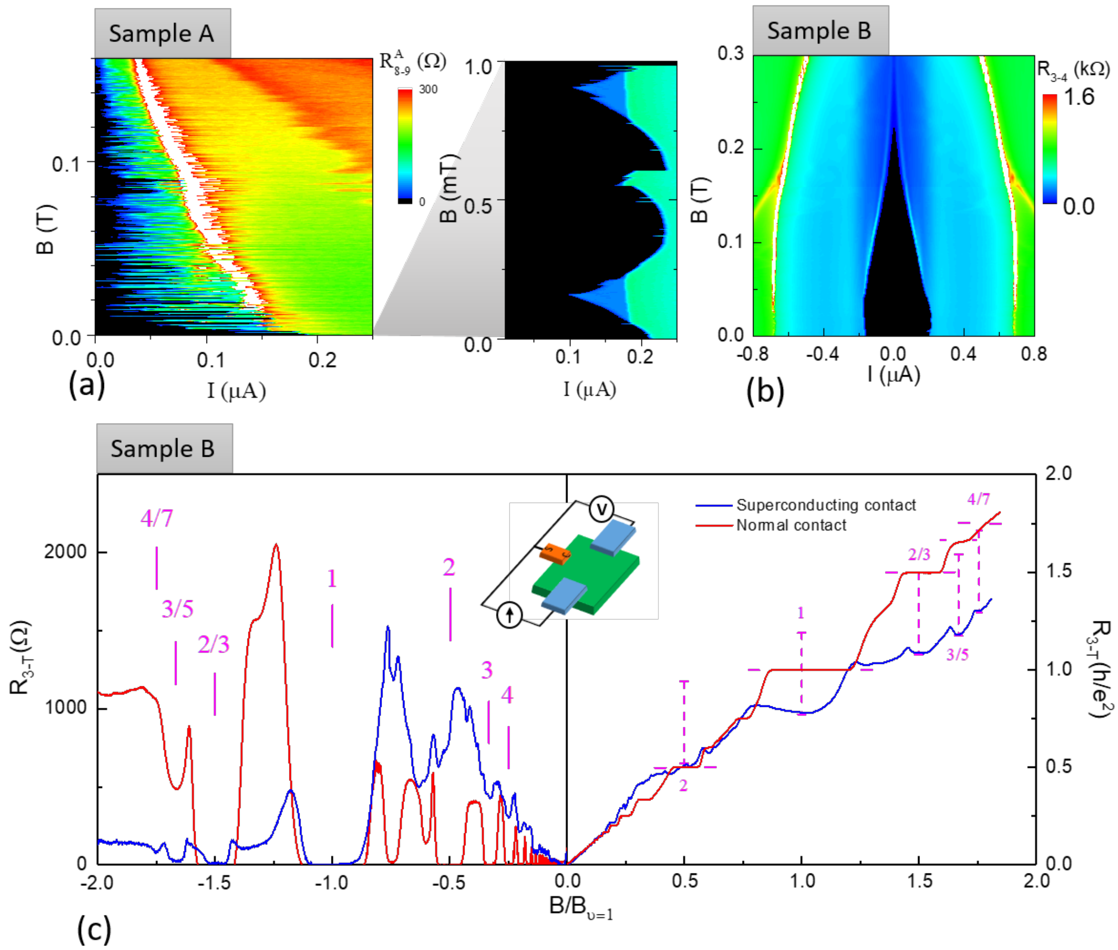

Figure 2.4.1. **Magnetic field dependence of induced superconductivity.** (a,b) Differential resistance is measured as a function of B and I_{dc} for two samples at 40 mK. Induced superconductivity (black region) is observed up to 0.2 Tesla in both sample. (c) 3-terminal resistance for a sample with all normal contacts (red) and between normal and superconducting contacts in sample B [I $(2-4)$ and V $(4-1)$ in Figure 2.1.2] is measured at 70 mK and 40 mK respectively. $B<0$ ($B>0$) induces clockwise (counterclockwise) chiral edge channels, note resistance scales difference for two field directions.

reflect the abrupt phase jump in the induced superconducting gap, which indicate that flux trapping and de-trapping occurs dutring the field scan. The period of oscillations is ~ 0.75 mT which corresponds to an area of 2.7 μm^2, much smaller than the area of the 2DEG between the contacts (≈ 120 μm^2). This observation is consistent with the reduced I_cR_N product measured for this sample as discussed above. In sample B contacts are fabricated along the edge of the mesa and 2D gas is not enclosed between the contacts. Consequently, I_c is a smooth function of B.

Competition between superconductivity and chiral quantum Hall edge states is shown in Figure 2.4.1c, where resistance is measured in a 3-terminal configuration over a wide range of magnetic fields. Simple Landauer-Buttiker model of edge states predicts zero resistance for negative and quantized Hall resistance for positive field direction for IQHE and FQHE states, which is clearly seen in a sample with all normal ohmic contacts (red curve). Here, we refer R_{-} as resistance measured in negative field and R_{+} as resistance measured in positive field. with normal contacts, R_{+} is well quantized in several IQHE and FQHE, and $R_{-} = 0$ in those states. This results are in consistant with Landauer-Buttiker model of edge states.

When a superconducting contacts serves as a current injector (figure2.4.1 blue curve), we observed a clear deviation from the measurement performed in normal contacts. At low field ($\nu > 5$), the R_{+} measured with superconducting contacts are similar to the one measured in normal contacts. In IQHE regime, at low fields states $\nu = 3, 4 and 5$, R_{-} have resistance minima for $B < 0$ indicating partial equilibration of chiral edge currents with the superconducting contact, while resistance near $\nu = 2$ has a maximum. On the other hand, in $\nu = 1$ plateau, $R_{-} = 0$ and $R_{+} = 0.75 R_0$ indicated a developed QH state with the reduction of Hall resistance. The differences behaviour of those IQH states has been been theoretically studied previously [25], where author suggested that spin polarization in the edge states could result a different behaviour between polarized states and un-polarized state. But in our measurement, zero resistance at $\nu = 1$ and large resistance at $\nu = 2$ are in contrast to the theoretical prediction that $\nu = 2$ state should be stronger coupled to a superconducting contact than $\nu = 1$.

in FQHE regime, $\nu = 2/3$ and $3/5$ states are well developed for $B < 0$. In the same states at $B > 0$, R_{+} are not quantized at proper QHE values. If we assume that current injection via superconducting contact results in an extra voltage offset at the contact $V_{off} \approx \Delta_{ind}/e$, the measured voltage will be reduces by V_{off}. The magenta bars for $B > 0$ indicate corrected resistance $(V - V_{off})/I$ for $V_{off} = 140\ \mu$V. While this offset may explain the measured values for fractional states, a twice smaller V_{off} is needed to reconcile the resistance at $\nu = 1$. The modification of Hall voltage in FQHE has been discussed in reference [20, 87], the author suggest that between the domain of superconducting coherence tunneling and normal tunneling, the edge state of FQHE can support non-abelian static. The 2 terminal conductance for such geometry would be modified by the Andreev reflection. In the perfect case, quantum conductance would be doubled to its original with the help of superconducting contacts. In our measurement, the R_+ shows 70% of its normal value, which is in contract to the theory.

To summary, by using the top down approach, we managed to induced superconductivity in high-mobility 2DEG in GaAs. Highly transparant contacts have been achieved and characterized by Andreev reflection. Supercurrent with characteristic temperature dependence of a ballistic junction has been observed across 0.6 mm, a regime previously achieved only in point contacts but essential to the formation of well separated non-Abelian states. The modification of Hall voltage with superconducting contacts shows evidence of interplays between superconductivity and strongly correlated states in a 2DEG at high magnetic fields.

3. Experimental investigation of the induced superconductivity in InAs 2DEG

3.1 Introduction

Majorana modes have been therotically predicted to reside in an 1 D superconducting wire with lifted spin degeneracy[88, 89]. It has been realized experimentally in a 1 D semiconductor wire with strong spin-orbit interaction and proximity induced superconductivity [16, 15]. A high transparency contact between superconductor and semiconductor is need to avoid quasi-particle poisoning and improve the coherence length [90]. Therefore in-situ epitaxial growth of SC material on semiconductor using MBE is prefered. This has been realized in 1-D system, and experimental characterization of the junction confirmed the highly transparant contacts between sc and semiconductor [91]. In order to achieve a functional Majorana devices, network of several Majorana modes is required, which is difficult in 1D system [92]. Recent technology progress in MBE growth of III-V semiconductor allow us to access high mobility 2-D system via heterostructure design [93]. Motivated by the idea of epitaxial growth of Al on heavily doped n+ GaAs [94, 30], epitaxial growth of Al is realized in InAs as well as other III-V semiconductor with strong spin-orbit interaction [39, 95, 96, 97]. Despite the rising interest in MBE grown SC/InAs JJs, the CPR and transport types of such junction remains unknown. Here we report fabrication of an InAs superconducting quantum interference device (SQUID) using MBE-grown Al/InAs 2-D system. The SQUID consist of two Al/InAs/Al Josepheson junction(JJ) which can be tuned with individual gates. By measuring the current phase relation (CPR), we can evaluate the transparency of the interface and transport through the junction.

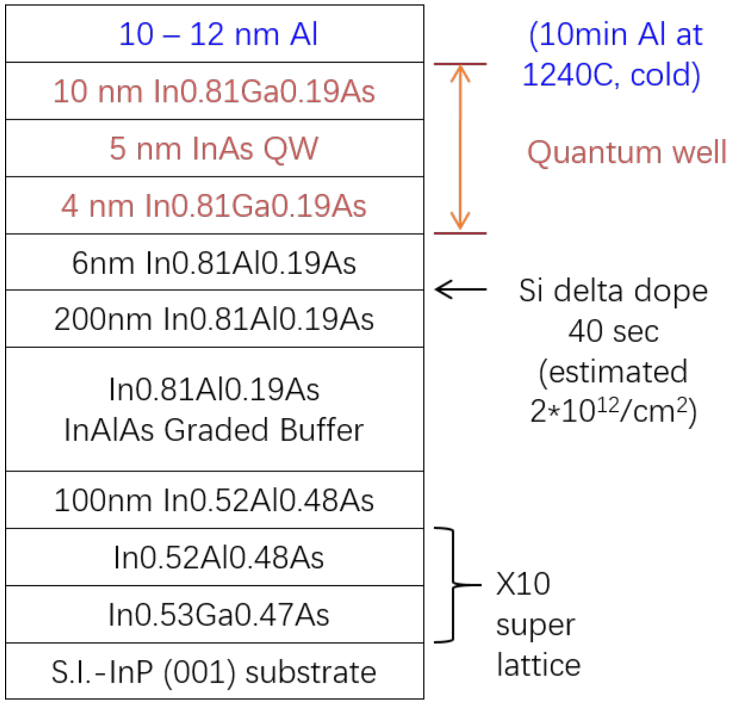

Figure 3.2.1. **Growth sequence of the of the InAs/Al wafer used in the experiments.** Schematic of the MBE growth. The wafers are grown by our collabrator professor Shabani at NYU

3.2 Device fabrication

Figure. 3.2.1 shows the schematic of the wafer design, InAs/InGaAs heterostructure was growth by MBE. First, 10 layers of superlattice was grown to compensate the defects in the substrate. The $In_{0.81}Al_{0.19}As$ buffer layer was grown to relax the lattice mismatch between InP and InAlAs, the Si δ doping is located 35 nm below the surface, the quantum well was form by a sandwich structure of $In_{0.81}Al_{0.19}As/InAs/In_{0.81}Al_{0.19}As$ close to the surface. Last, with reduced temperature to avoid Al diffusion, a 10 nm Al layer was grown on the surface. The shallow 2DEG is located 15 nm below Al layer. The mobility $\mu = 1200$ cm^2/V $\cdot$ s and the density $n = 1.5 \cdot 10^{12}$cm^{-2}.

Figure. 3.2.2 (a) shows the process flow for fabricating SQUID using top down approaches. First, we define the contacts using e-beam lithography. Then a thin layer of Ti/Au (5/10 nm) is deposited as etching masks to etch Al. The Al etching was done using transcend-D Al

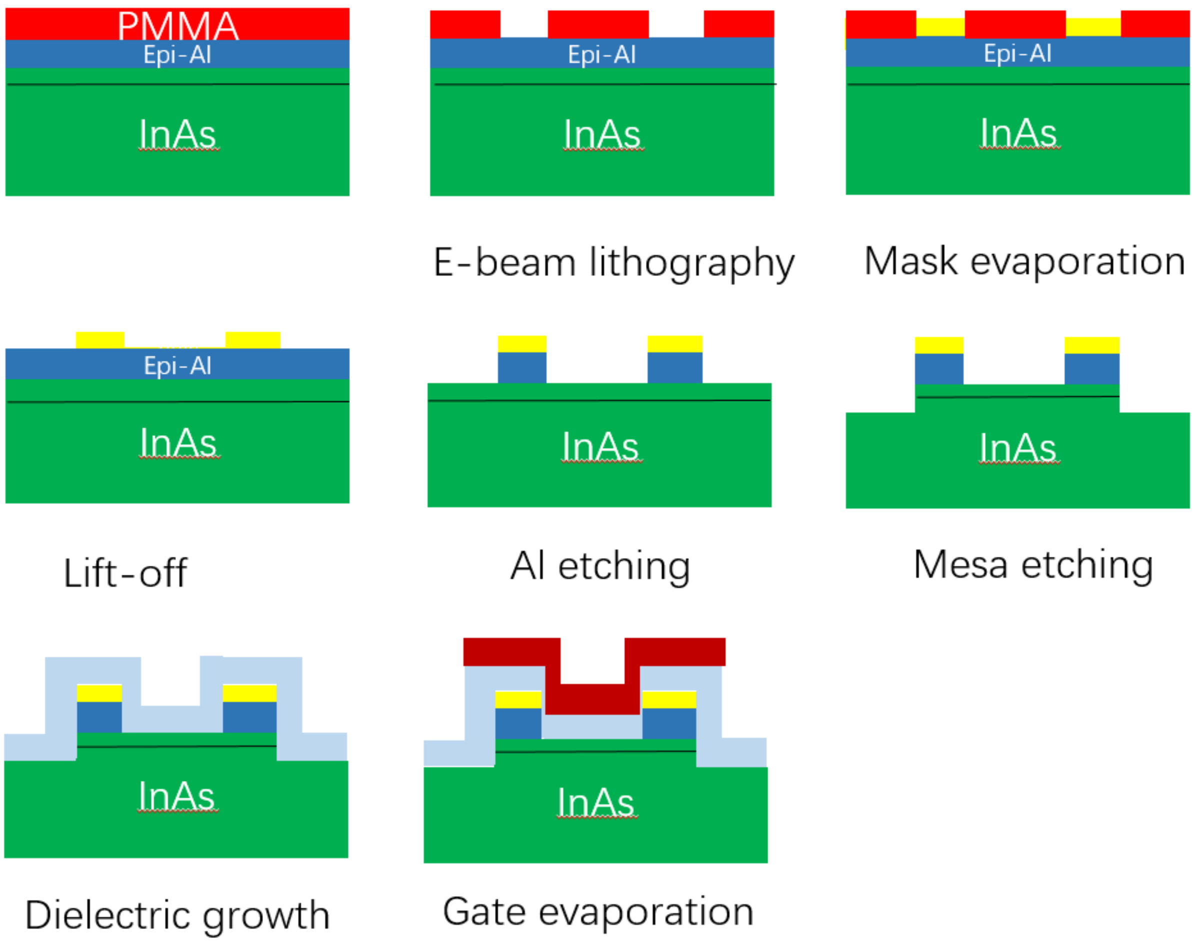

Figure 3.2.2. **Schematic of the fabrication process.**

etchant with a bath temperature of 40°C, the total etching time is 40 seconds, with the first 30 seconds to remove the Al and last 10 sec to ensure a complete removal of Al. Second, we define mesa area and use PMMA as an etching mask to chemically remove the InAs 2DEG outside the mesa. The mesa etching was done using standard III-V semiconductor etchant, a diluted Piranha solution $H_2O_2 : H_2SO_4 : H_2O = 1 : 8 : 1000$. The etching time is 90 seconds, results in a 90 nm etching depth. Third, we use low temperature (150°C) ALD to grown 45 nm of Al_2O_3, this relative low temperature growth prevent the potential Al diffusion into InAs, and the formation of InAlAs. Last, two metal gates are deposited on top of each

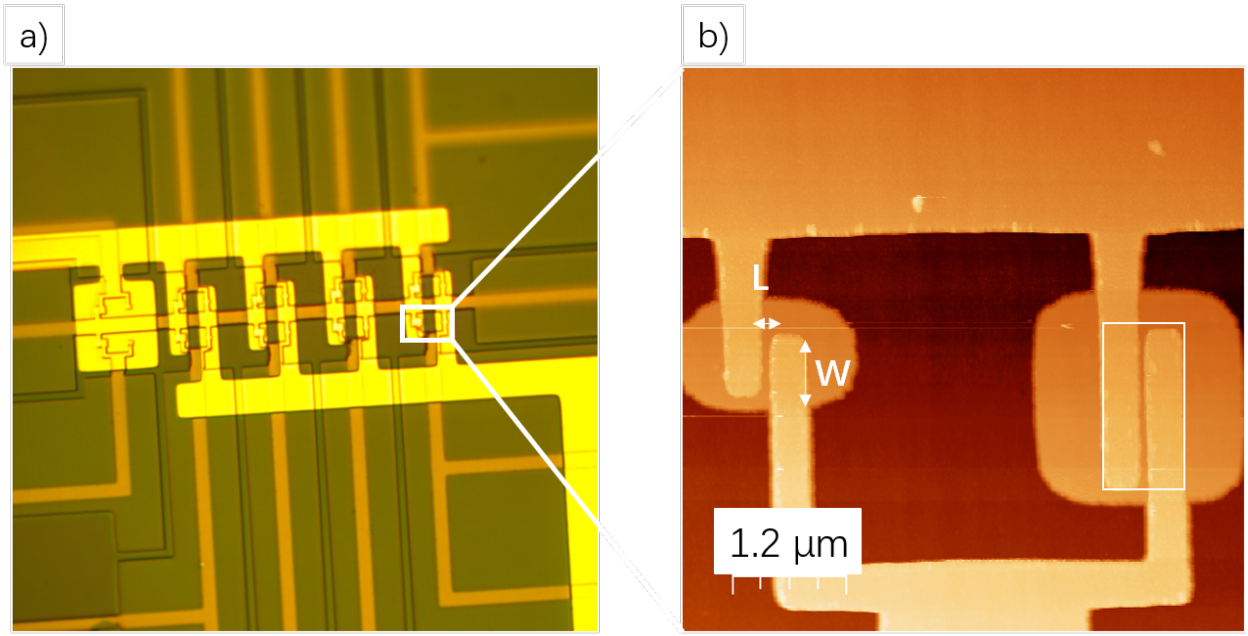

Figure 3.2.3. **A microscopic image and an AFM image of Device.**(a). A microscopic image of the devices Typical device of an InAs SQUID, 8 SQUIDs are fabricated on the same chip, those SQUIDs are seperated by mesa etching. The dark orange regions are the Al contacts. The light yellow regions are the gates. (b) An AFM image of the Device. the larger JJ has a width of 1.2 μm, the smaller JJ has a width of 0.5 μm. The gap between Al in each junction for the device we measured is 120 nm and the whole area of the SQUID is about 9 μm^2.

SQUID to individually control junctions. The gates allow each Jpsepheson junction in the SQUID to be tuned from a superconducting weak links into tunnelling regime.

Figure 3.2.3 (a) shows a microscope image of a device we used for measurements. Here, 8 SQUIDs are fabricated on the same chip, those SQUIDs are seperated by mesa etching. The dark orange regions are the Al contacts which becomes superconducting below 1.5 K. The light yellow regions are the gates. Figure 3.2.3 (b) shows an AFM imagine of one of the SQUIDs before Al_2O_3 deposition. The left arm (JJ-1) has a width of 500 nm and the right arm (JJ-2) has a width of 1.2 μm , the gap between Al in each junction for the device we measured is 120 nm and the whole area of the SQUID is about 9 μm^2.

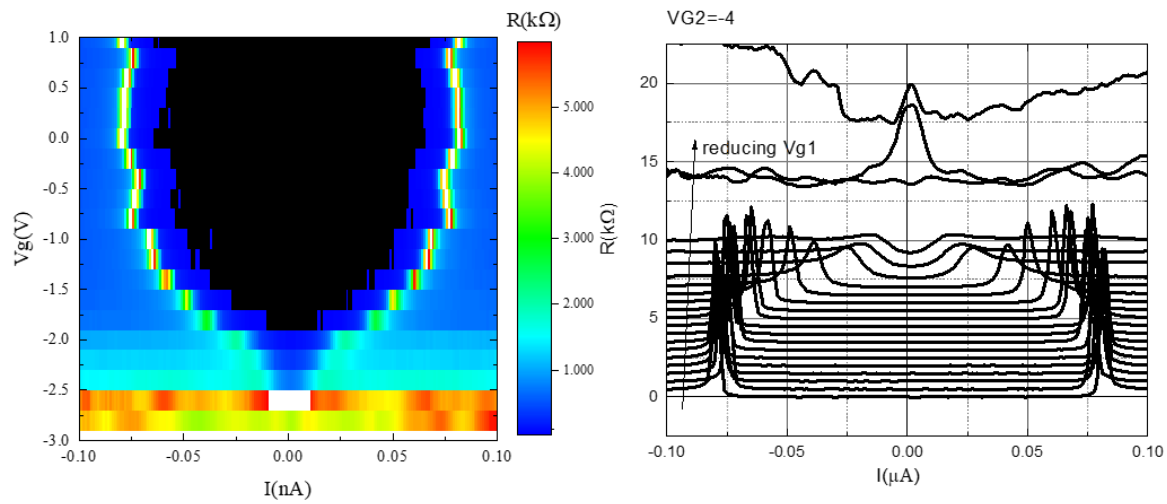

Figure 3.3.1. **Gate dependent of the critical current of individual Josepheson junction.**(a)Gate and current dependence of the JJ-2. (b) Current dependence of the R in JJ-1 at different gate voltage, the data is off-setted by 0.5 $k\Omega$.

3.3 Transport measurement of Josepheson junctions

The gate dependence of the resistances studied in junction JJ-2 is shown in figure 3.3.1. To characterize JJ-2, we apply negative $V_{g1} = -4\ V$ to fully deplete JJ-1 into a tunnelling regime ($R > 100k\Omega$), therefore the measured resistance is dominated by the resistance of JJ-1. In such a way, we found that the critical current (I_c) of JJ-2 at zero gate voltage is 75 nA. When Vg1 is larger than -0.6 V, I_C does not change with the gate voltage, indicating that the onset gate voltage of I_C is -0.6 V. When the V_{g2} is less than -1.8 V, the JJ-1 becomes non-superconducting. When the V_{g2} is less than 2.5 V, the JJ-2 became a tunnelling junction, this is indicated by the sharp resistance peak at zero bias. In the voltage bias, this is corresponding to a $\Delta V = 0.25\ \mu$V. The superconducting gap of Al: $2\Delta_{Al} = 2 \cdot 1.72 k_B T_c = 0.45\ \mu$eV, here the superconducting temperature T_c of Al is 1.7 K in our measurement. The measured gap we measured are smaller than the superconducting gap of Al, suggesting that the induced gap is smaller than the superconducting gap of Al. On the other hand, at

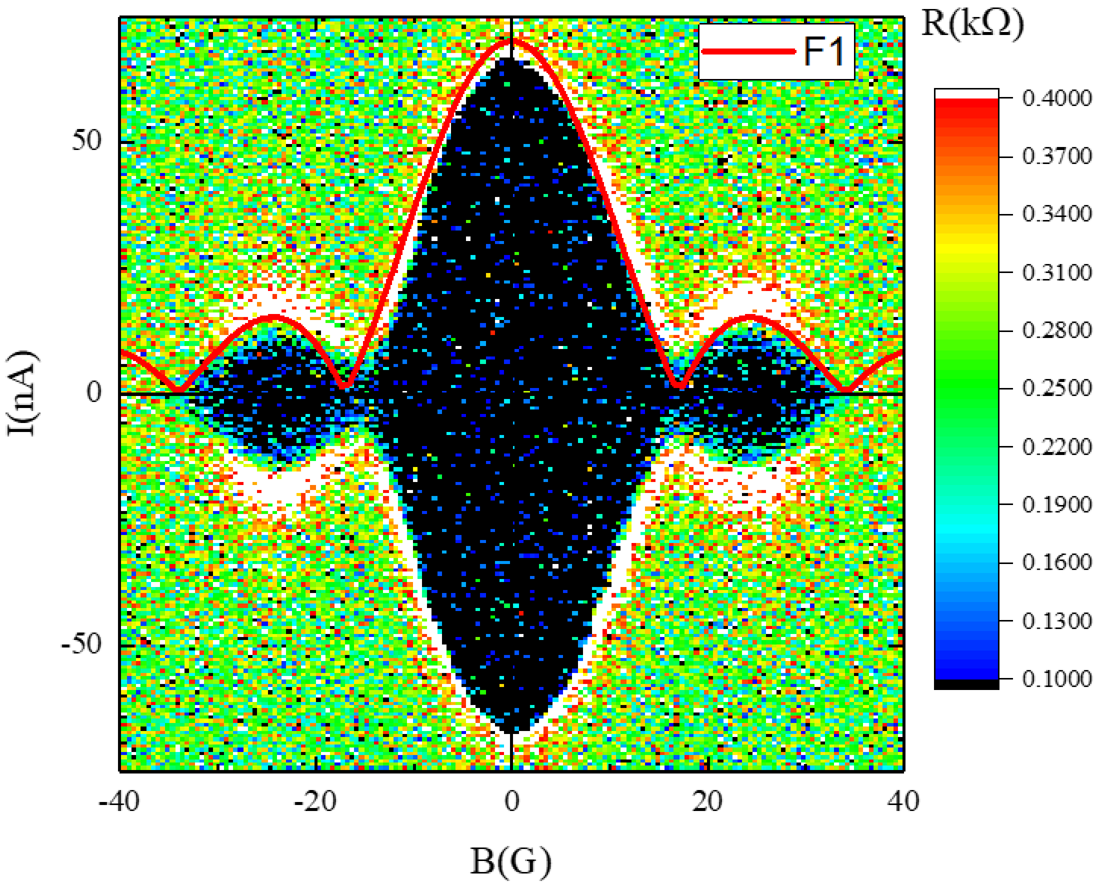

Figure 3.3.2. **Field dependent of the critical current of individual Josepheson junction.**The Field dependent of the JJ-2 shows a typical Fraunhofer pattern. Red line is the fitting of the Fraunhofer pattern with Ic=70 nA and an area of 1.2 μm^2.

zero gate voltage, the product of critical current and normal resistance $I_c R_n = 0.035\ \mu$V is about 6 times smaller than the Al superconducting gap, also indicate that the induced superconducting gap is much small the the gap of Al, and the transparancy of the junction is less than 100%.

When a perpendicular field is applied, flux focusing results in aperiodic node spacings in field dependence of critical currents known as Fraunhofer patterns:

$$I_C(B) = I_c^0 \Big| \frac{sin(\pi\phi/\phi_0)}{\pi\phi/\phi_0} \Big|. \tag{3.3.1}$$

Where I_c^0 is the critical current at zero field, ϕ_0 is the magnetic flux quanta, $\phi = B \cdot S$and S is the area in InAs where supercurrent has been proximity induced. Figure 3.3.2 shows the field dependence of the resistance with $V_{g1} = -4$ V, the black region is the superconducting state. Here we observed the critical current oscillates with the field when $B < 35$G, due to the small induced gap we observed in our JJ-2, the critical field of our JJ-1 is $B_C \approx 35$G, which is also much smaller than the critical field of Al. The red line in the figure is a fit of critical current using equation 3.3.1, here we use $I_c^0 = 70$]nA. From the separation of the first two nodes, we can obtain the total area $S = \phi/B = 1.2$ μm^2. The rectangular frame in figure 3.2.3 shows a size of 1.2 μm^2, this rectangular frame is much larger than the normal region separated by Al contacts, this means that not only the area within the gap becomes superconducting, but also the area under two Al leads become superconducting.

3.4 Current phase relation of an InAs/Al SQUID

Next, we tuned both junction into superconducting regime and measure magnetic field dependence of the critical current. The SQUID are tuned into a symmetric regime where the critical current of individual junction $I_{C1} = I_{C2}$. As shown in figure 3.4.1 for a variety combination of V_{g2} and V_{g1}, a symmetric SQUID can be achieved, in those configuration, the modulation of $I_C \approx 100\%$. The critical current of the SQUID $I_C = I_C \cdot \mid sin(\pi\phi/\phi_0) \mid$. Here $\phi = B \cdot S$ is the total flux enclosed by the SQUID loops. the period of the oscillation for the symmetric SQUID is 3.1 G, corresponding to an area of 6.5 μm^2.

By reducing V_{g1} and increasing V_{g2}, I_{C1} is reduced and I_{C2} is increased, thus SQUID is tuned into an asymmetric regime. With $I_{C1} > I_{C2}$, the phase difference across JJ-2 is very

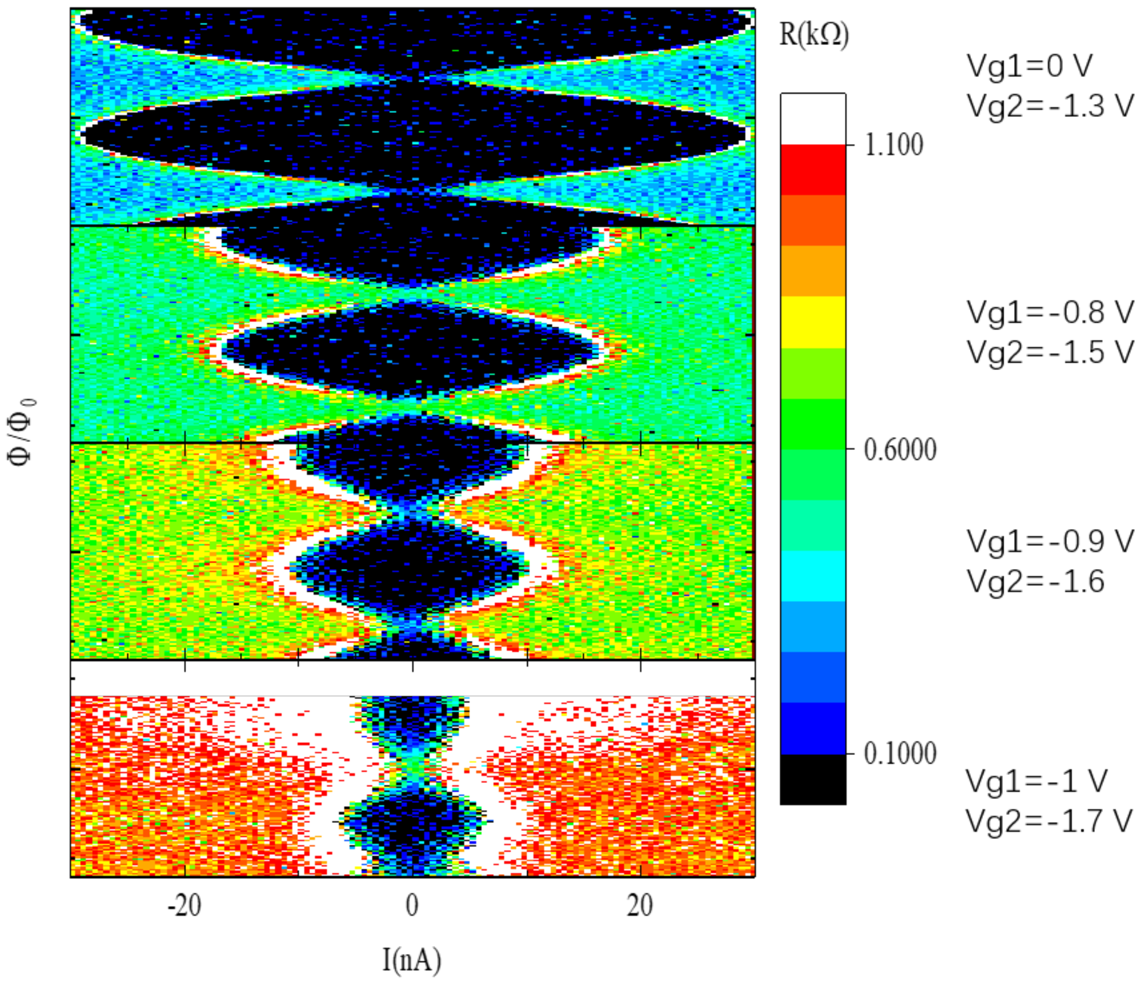

Figure 3.4.1. **Current phase relation of symmetric SQUID.**(a)Gate dependent of the larger JJ which has a width of 1.2 μm, Gate dependence of the smaller JJ which has a width 0.5 μm.

close to $\pi/2$. Thus the total critical $I_C = I_{C1} + I_{C2}(2\pi\phi/\phi_0 + \pi/2)$. For a junction with arbitary transparency, the current phase relation can be written as:

$$I_C(\phi, T) = I_C(\phi = 0, T)\frac{\sin(\phi)}{\sqrt{1 - D\sin^2(\phi/2)}} \times \tanh\frac{\Delta(T)}{2k_BT}\sqrt{1 - D\sin^2(\phi/2)}, \qquad (3.4.1)$$

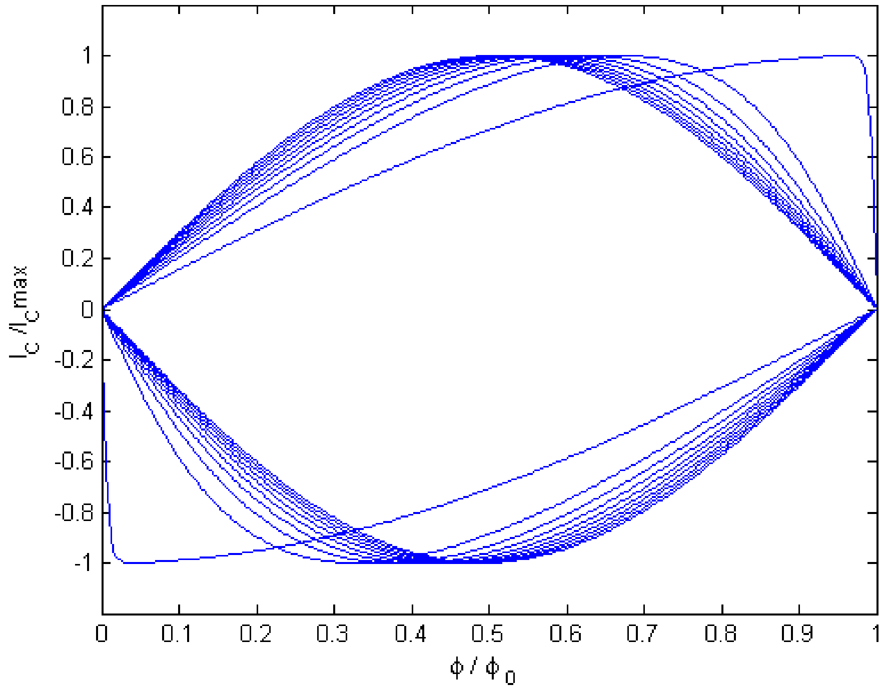

Figure 3.4.2. **Numerical calculation of CPR in a SQUID with different D.** The transparancy parameter D interpolated from D=0.1 to D=1, for a more ballistic junction, the more forward skewness can be observed.

This equation interpolated between diffusive ($D = 0$) and ballistic ($D = 1$) junctions. The numerical calculation of the CPR with different D is shown in figure 3.4.2, the signature of a ballistic transport across the Josepheson junction is the forward skewness in the CPR, and with the reduction of the transparency, the CPR becomes more and more sinusoidal.

Figure 3.4.3 (a) shows the resistance as a function of current and magnetic field in the asymmetric regime, figure 3.4.3 (b) is the extracted CPR of the SQUID from (a). In this regime with $I_{C2} > I_{C1}$, we observed a small shift between positive critical current(I_{C+}) and negative critical current (I_{C-}), this shift is attributed to the skewness of CPR from a perfect sinusoidal function. Figure 3.4.3 (c) shows the amplitude of the FFT calculated from figure 3.4.3 (b), the amplitude of higher order harmonic is clearly observed. The skewness can be quantified by the total harmonic distortion (THD) of the current phase relation in an asymetric SQUID. The THD is defined as $\mathrm{THD} = \sqrt{\frac{\Sigma_{i=2}^{\infty} A_i}{A_1^2}}$. Here, A_i is the amplitude of

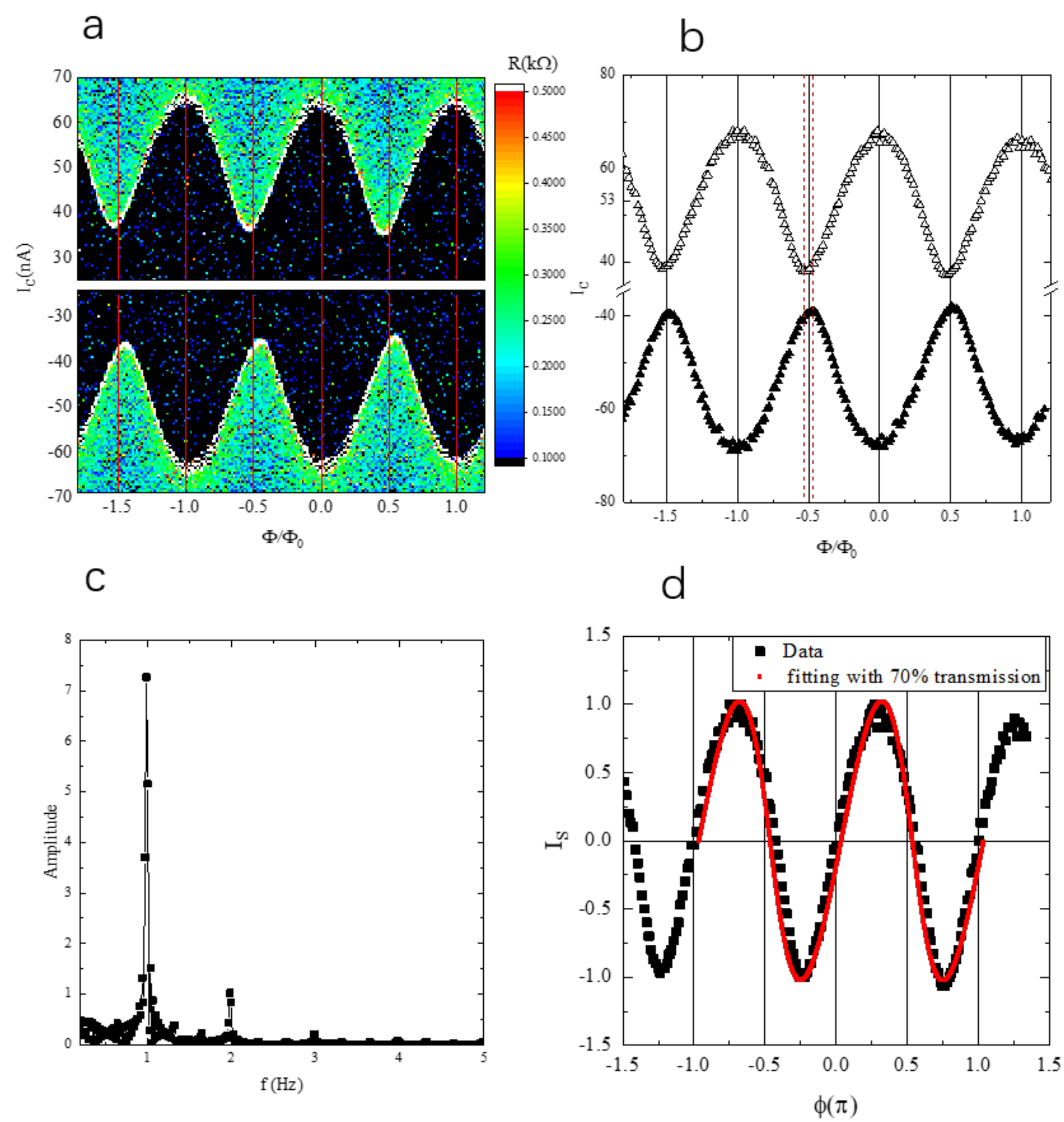

Figure 3.4.3. **Current phase relation of the SQUID.**(a)Gate dependent of the larger JJ which has a width of 1.2 μm, Gate dependent of the smaller JJ which has a width 0.5 μm.

the i^{th} harmonic in the CPR measurements. In our experiment, for simplicity, we ignored A_i for $i > 3$,since the amplitude is less than 1% of A_1 when $i > 3$. The experimental obtained THD = 15%, which correspond to $D = 0.7$. In a ballistic limit when $D = 1$, THD = 55%. Figure 3.4.3 (c) shows the fitting of CPR with $D = 0.7$, here we rescale I_C to $I_S = (I_C - I_{C2})/I_{C1}$ after converting flux Φ to phase ϕ. In such ways, we show that the InAs/Al SQUID is in a quasi-ballistic regime.

3.5 Conclusion

In summary, we have fabricated a SQUID on InAs/Al substrates using top down technique. We use these SQUIDs to study the CPR of in the Al/InAs/Al Josehpeson junction. The fully gate-tunable SQUIDs allow us to investigate the junction from a superconducting regime to a tunneling regime. We shows that in a asymmetric SQUID, the CPR of the SQUID is slightly non-sinusoidal which indicates that the Josehpeson junction of the SQUID is in a quasi-ballistic regime. Such transparancy can be further improved in order to eliminate quasi-particle poisoning and reduce the normal reflection which is detrimental to the measurement of Majorana bound states. We believe that the simplicity of our device architecture and measurement scheme should make it possible to use such devices for further studies of the CPR in topologically non-trivial InAs/Al Josephson junctions.

4. Formation of helical domain walls in the fractional quantum Hall regime

4.1 Introduction

Topological qunatum computation can be performed with Majorana fermion(MF)[98], but MF-based qubits are not computationally universal. Parafermions(PFs)[99], higher order non-Abelian excitations, are predicted to have denser rotation group and their braiding enables two-qubit entangling gates [100, 24]. A two-dimensional array of parafermions can serve as a building block for a system which supports Fibonacci anyons with universal braiding statistics[21], a holy grail of topological quantum computing. In an important conceptual paper, Clark et al. proposed that PF excitations can emerge in the fractional quantum Hall effect (FQHE) regime if two counter-propagating fractional chiral edge states with opposite spin polarization are brought into close proximity in the presence of superconducting coupling[20]. In this chapter, we demonstrate experimentally that in a triangular quantum well a 2D system can be tuned across a spin transition at a filling factor $\nu = 2/3$ using electrostatic gating. We also demonstrate formation of conducting channels at boundaries between incompressible polarized and unpolarized $\nu = 2/3$ states. These channels are formed from two counter-propagating $\nu = 1/3$ states with opposite spin orientations, we refer to them below as fractional helical domain walls (fhDW) in analogy to helical channels formed along the edges in the quantum spin Hall effect. Local control of polarization allows formation of a reconfigurable network of fhDWs with fractionalized charge excitations and, potentially, parafermion manipulation and braiding.

Helical channels are commonly associated with the quantum spin Hall effect[101], topological insulators[102] or nanowires with spin-orbit interactions[18, 103], where Coulomb interactions are not strong enough to fractionalize charges. A natural system to look for PFs is a 2D electron gas (2DEG) in the FQHE regime, where edge states support fractionally charged excitations. In the conventional QHE setting, though, edge modes are chiral. Helical channels can potentially emerge as domain walls during a quantum Hall ferromagnetic transition. It has been predicted that domain walls formed in the integer QHE regime at a filling factor $\nu = 1$ have helical magnetic order[104]. Experimentally, local electrostatic control of domain walls in the integer QHE regime at $\nu = 2$ was recently demonstrated in magnetic semiconductors [74], and their electronic and magnetic structure has been calculated[105]. In the FQHE regime spin transitions have been observed at a filling factor $\nu = 2/3$ as well as other fractions[68, 70]. At the transition, the 2DEG spontaneously phase separates into regions of different spin polarizations, and conducting domain walls are formed along the domain boundaries[106, 107]. An experimental challenge is to devise a system where spin transitions in the FQHE regime can be controlled locally, allowing formation and manipulation of DWs. Theoretically, neither magnetic nor electronic structure of these domain walls is known [13].

4.2 Observation of helical edge state between polarized and un-polarized $\nu = 2/3$ state

In order to demonstrate electrostatic control of polarization, a number of wafer with inverted GaAs/AlGaAs interface have been grown by our collaborator Professor Loren Pfeiffer's group. The details of the wafers is listed in appendix A. These Inverted GaAs/AlGaAs heterojunctions are grown by molecular beam epitaxy, the top layer is 130-230nm thick GaAs, Si δ-doping placed 70-300 nm beneath the heterojunction interface. The top 25 nm of GaAs are lightly doped to reduce the surface pinning potential. In the following experiment, the data was taken on devices fabricated from LE40. Inverted heterostructures allow electrostatic gating of a shallow 2D gas with no hysteresis, also in a similar wafer proximity-induced superconductivity has been reported in chapter 2. Ohmic contacts are formed by annealing Ni/Ge/Au 30nm/50nm/100nm, in a H_2/N_2 atmosphere. 10 nm-thick Ti gates are separated from GaAs and from each other by 50 nm Al_2O_3 grown by an atomic layer deposition (ALD).

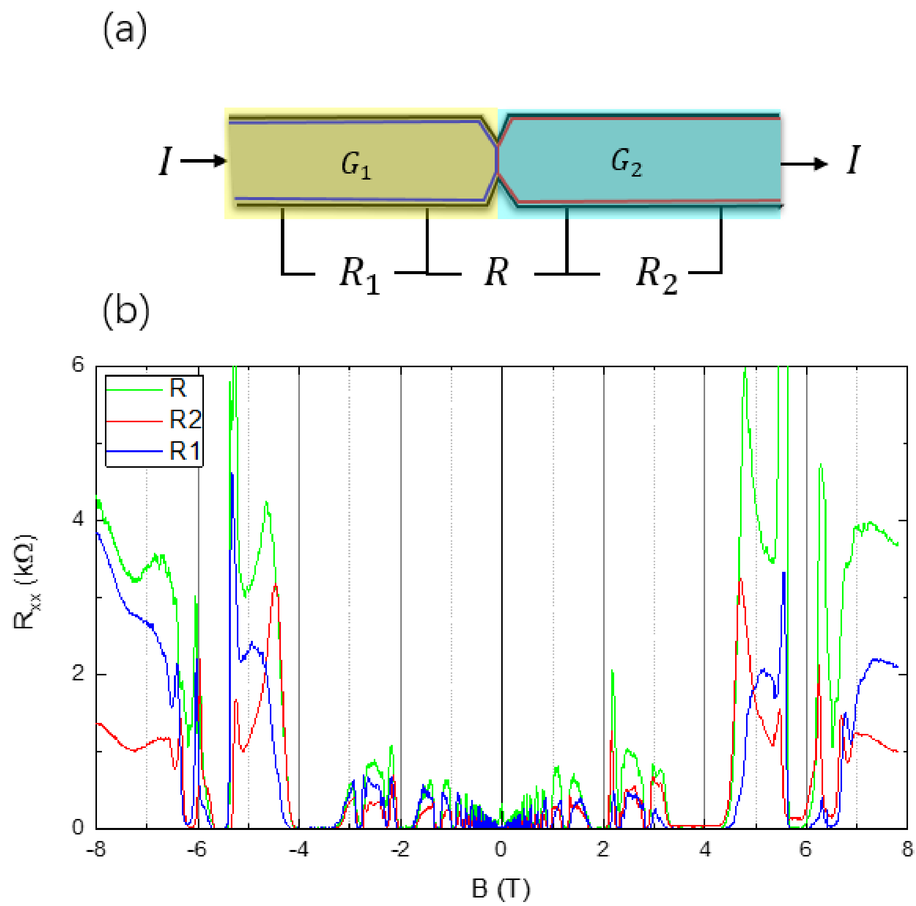

Figure 4.2.1. **Device schematic and low temperature transport.** (a) The schematic of the device layout. Current is passed from source to drain with R_1 measure R_{xx} under V_{g1}, R_2 measure R_{xx} under V_{g2} and R measure R_{xx} across the boundary of V_{g1} and V_{g2}, the constriction between two edges is varying from 2 μm to 7 μm. (b), magnetic field dependence of R_1, R_2 and R, at zero gate voltage $T = 18\ mK$.

The Ti and Al_2O_3 are fabricated to be semi-transparent and a 2D electron gas is created by shining red LED at $\sim$ 4. Measurements were performed in a dilution fridge with the base temperature $T \approx 18mK$ using a standard lock-in technique with excitation current $I_{ac} = 0.1 - 10nA$.

The schematic of the device layout is shown in figure 4.2.1. Devices are patterned into Hall-bar geometry. Current is passed from source to drain with R_1 measuring R_{xx} under G_1, R_2 measuring R_{xx} under G_2 and R measuring R_{xx} across the boundary of V_{g1} and V_{g2}. Figure

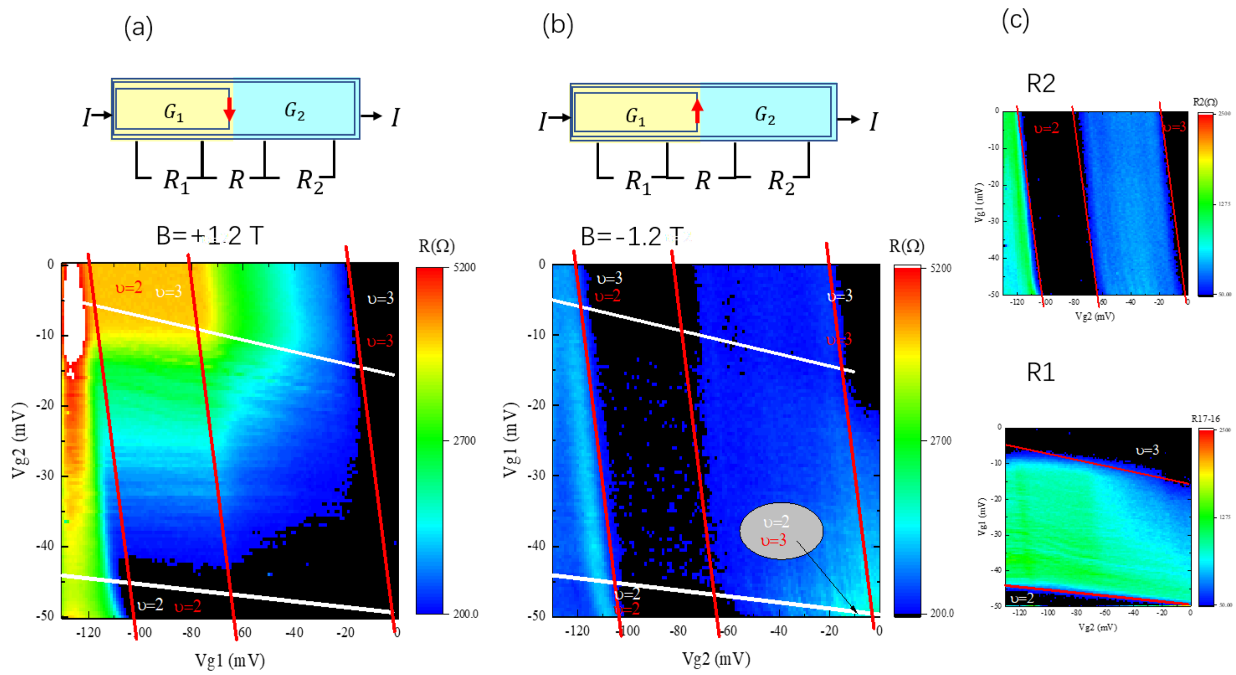

Figure 4.2.2. **Formation of chiral edge channel in gated Hall bar device.** (a)Top, the schematic of the formation of edge state. Bottom, R as a function of V_{g1} and V_{g2} under positive magnetic field, the resistance of the top right corner is 4300 Ω. (b) Top, the schematic of the formation of edge state. Bottom: R as a function of V_{g1} and V_{g2} under negative magnetic field, the resistance of the top right corner is $R = 0$ Ω. (c) Top, R_1 as a function of V_{g1} and V_{g2}. Bottom, R_2 as a function of V_{g1} and V_{g2}.

4.2.1 shows the results of R_{xx} measurement at $T = 18\ mK$. With no gate voltage applied on V_{g1} and V_{g2} gate voltage, R_1, R_1 and R show plateau at same B field, which suggests that the density of 2DEG is uniform across the Hall-bar. The nominal 2DEG density is $n_0 = 0.89 \cdot 10^{11}/cm^2$, and mobility $\mu = 5 \cdot 10^6 cm^2/Vs$.

By applying negative gate voltage the 2DEG density can be reduced. The gate dependence of the density under G_1 is $n_1(cm^{-2}) = n_0 + 4.93 \cdot 10^8 \cdot V_{g1}(mV)$, and under G_2 is $n_2(cm^{-2}) = n_0 + 3.16 \cdot 10^8 \cdot V_{g2}$, where $n_0 = 0.89 \cdot 10^{11}\ cm^{-2}$ is the 2DEG density with zero gate voltage.

First, the measurements are performed in IQHE with $\nu = 2$ under G_1 (G_2), $\nu = 3$ under G_2 (G_1). With fixed $B = 1.2\ \ T$, by changing the V_{g1} and V_{g2}, the $\nu = 2$ and $\nu = 3$ states can be observed in the same B field under both gates. As shown in figure 4.2.2 (c), the black region is where R_1 and R_2 becomes zero, which is the signature of $\nu = 2$ and $\nu = 3$ states. At the same time, R is also recorded as a function of V_{g1} and V_{g2}: when both n_1 and n_2 are in $\nu = 2$ or $\nu = 3$ regime, R becomes 0, as shown in figure 4.2.2 (a) and (b), the top right and bottom left corner. These zero resistance states in R show that density difference across the gate boundary does not result in the formation of a conducting channel. The chirality of the edge state is shown in figure 4.2.2 (a) and (b), in the top left corner of the color map. Under positive B field, with n_1 is tuned to $\nu = 3$ and n_2 is tuned to $\nu = 2$, the measurement of R shows a 4.3 $k\Omega$ plateau which is approximately $h/6e^2$. With the same measurement configuration but under negative B field, R becomes zero. The formation of an edge state between IQHE can be well understood within the Landauer-Büttiker formalism. For $B > 0$, $R = \frac{h}{e^2}(\frac{1}{\nu_1} - \frac{1}{\nu_2})$, in our case, $\nu_1 = 2$ and $\nu_2 = 3$, $R = 4.3$ kΩ [74]. For $B < 0$, R is zero.

4.3 Domain wall in $\nu = 2/3$ plateau

As mentioned in chapter 3, the composite fermion cyclotron energy $\hbar\omega_c^{cf}$ is proportional to the charging energy $E_c = E^2\sqrt{l_m^2 + z_0^2}$, where $l_m \propto \sqrt{B_\perp}$ is the magnetic length, $B_\perp = B\cos\theta$ is the out-of-plane component of the magnetic field B, and z_0 is the extend of the wavefunction in the out-of plane direction. Due to the difference in B-dependences of the two terms, the composite LL $\Lambda p, \downarrow$ and $\Lambda p + 1, \uparrow$ cross at $B^* > 0$. Thus, in the composite fermion picture, for $\nu^* = 2$ the top energy level undergoes a spin transition at B^*. Thus, the $\nu = 2/3$ state is unpolarized for $B < B^*$ and fully polarized for $B > B^*$.

Conventionally, spin transitions in $\nu = 2/3$ state are studied in tilted magnetic fields, where controlling the ratio of B and $B_\perp$ allows us to control B and B^*. In the triangular GaAs/AlGaAs quantum well, z_0 is gate dependent. Thus, local control with individual gate allows us to tune E_c and B^* at fixed $B_\perp$. Within the Fan-Howard approximation of the wavefunction in a triangular well, $z_0 = 3/b$, where $b \propto n^{1/3}$ is a function of electron density.

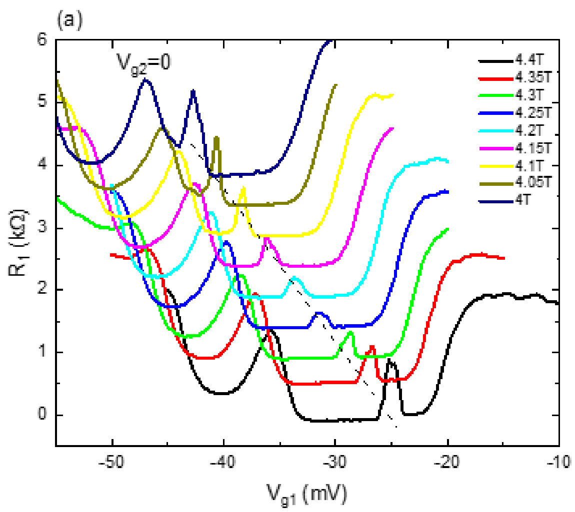

Figure 4.3.1. **gate and field dependence of spin transition around $\nu = 2/3$.**(a)Gate dependence of spin transition under G_1 with $V_{g2} = 0$.(b) gate dependence of spin transition under G_2 with $V_{g1} = 0$. Dash lines mark the trend of spin transition. Data are off-setted by 0.5 $k\Omega$ for clarity.

For GaAs parameters and $B^* \approx B_{\nu=2/3} \approx 4 - 6\ T$, the field B^* becomes density and gate dependent: $\delta B^*/B^* \approx 0.3\delta n/n$, $\delta n/n = \delta V_g/V_g$. The field position of the $\nu = 2/3$ state is also density and gate dependent,$\delta B_{\nu=2/3}/B_{\nu=2/3} = \delta n/n$. Thus, for a well-developed wide $\nu = 2/3$ state and a sharp spin transition, there should be a range of magnetic fields where spin polarization of the top level can be tuned locally by electrostatic gating.

Figure 4.3.1 shows the gate and field dependence of the R_1 and R_2 around $\nu = 2/3$ plateau . Each line was taken by scanning the gate dependent of R_1 and R_2 with a fixed magnetic field. Here, we observed a $\nu = 2/3$ plateau on both R_1 and R_2, these plateaus are interrupted by a small peak in each scan in the localized region of $\nu = 2/3$ with polarized state on one side of the peak and unpolarized state on the other side of the peak. The height of these peaks has strong current dependence, as well as hysteresis with respect to the field sweep and gate sweep direction with high excitation currents. These characteristics are consistent with previous studies of spin phase transitions [73], thus we identify these peak as a signature of spin transition in our samples. Most importantly, the broadening of the transition peak is narrow compared to the width of the $\nu = 2/3$ plateau. For example, under G_1, at $B = 4.2$ T with $I_{ac} = 1$ nA, the width of $\nu = 2/3$ plateau is 11 mV, and the width of the peak is 3 mV, corresponding to only 27% of the total plateau. By measuring spin phase transition in 2D bulk, we shows that under each gate, with a fixed magnetic field, spin polarization can be locally controlled with gate. Therefore, it is possible to tune our 2DEG system into a regime where spin polarizations are different across the boundary.

4.4 Transport study of the Domain wall in $\nu = 2/3$ plateau

The transport studies of the spin polarization transition across the boundary are shown in figure 4.3.2. Resistances R_1 and R_2 for the 2DEG under G_1 and G_2 are combined into a single plot in middle of (a) in order to visualize regions in the V_{g1} V_{g2} coordinate where FQHE states on both sides of the boundary overlap. A small coupling between the gates results in slightly non-orthogonal evolution of the features, but this does not affect our main claim in the following measurements.

First observation in our measurements is the chiral channel formed between $\nu = 2/3$ states and $\nu = 3/5$ states. In the region outlined red, incompressible 3/5 states are formed on both sides of the gate boundary and $R = R_1 = R_2 = 0$. A chiral channel is formed between 2/3 and 3/5 states (two regions outlined black). In this case resistance is gradient and field direction-dependent: $R = 0$ or $R = \frac{1}{6}R_q$ where $R_q = h/e^2$. This case is similar to the transition between $\nu = 2$ and $\nu = 3$ in IQHE as mentioned in the previous section. Thus the resistance $R = \frac{h}{e^2}(\frac{1}{\nu_1} - \frac{1}{\nu_2})$ with $\nu_1 = 2/3$ and $\nu_2 = 3/5$.

Within the $\nu = 2/3$ state, a small bump in the middle of $\nu = 2/3$ state in $R_1(R_2)$ is the spin transition which seperates spin polarized state (marked as "p" in figure 4.3.2 a) and spin unpolarized state (marked as u in figure 4.3.2 a). These two bumps in R_1 and R_2 separate the $\nu = 2/3$ region into four quadrants with different polarizations across the gate boundary. The top right corner refer as uu is the region where both hall-bar are unpolarized, the top left corner refer as "pu" is the region where hall-bar under G_1 is polarized and hall

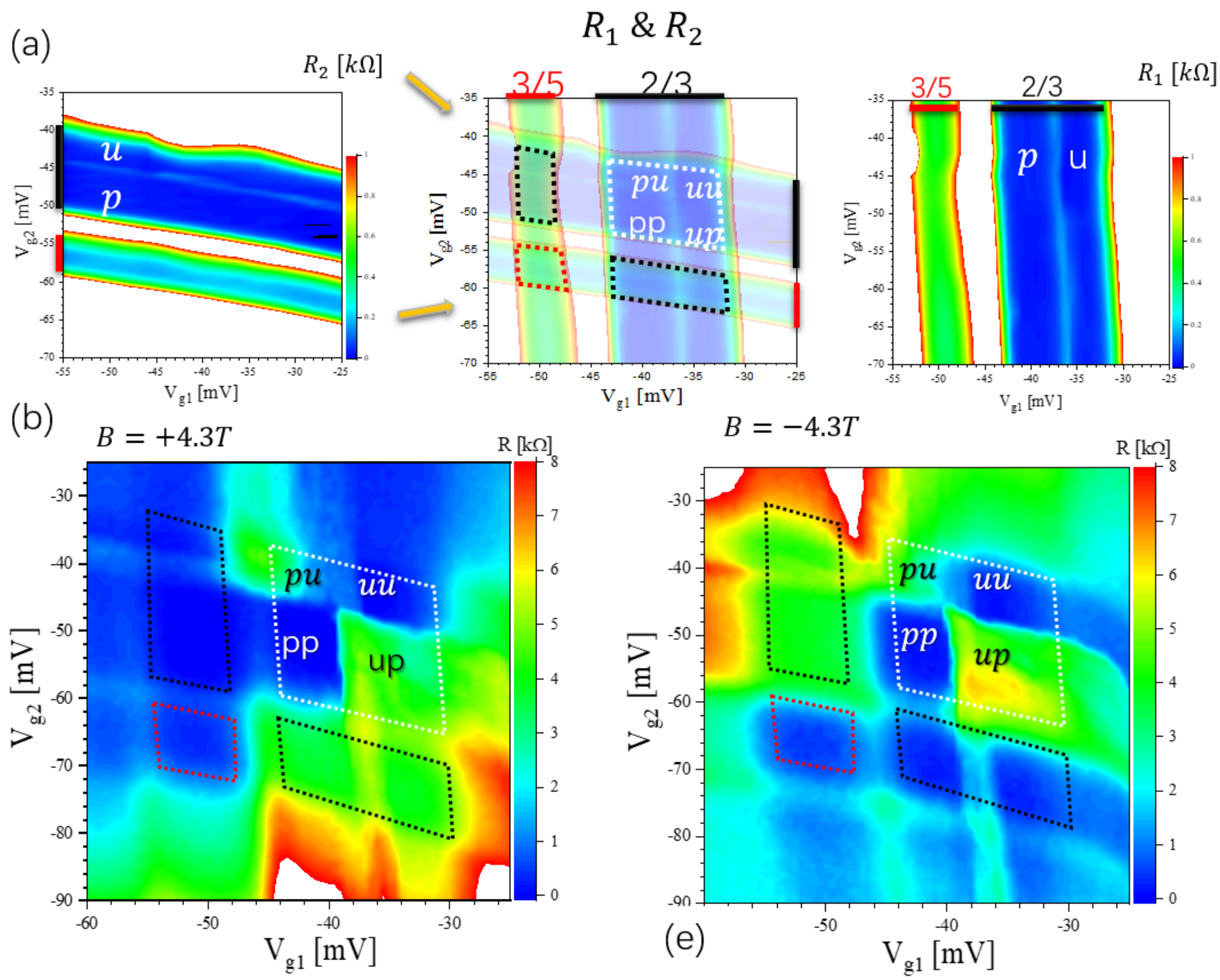

Figure 4.3.2. **Helical domain wall at $\nu = 2/3$.** (a)left and right: Resistance R_1 and R_2 is measured as a function of gate voltage V_{g1} and V_{g2} respectively.Letter u and p mark unpolarized and polarized states. Middle: R_1 and R_2 are plotted on top of each. The region where $\nu = 2/3$ under both gates is outlined with a white dotted line. (b) Resistance R across the gate boundary is plotted for two field directions. Non-zero R in (up) and (pu) quadrants indicate formation of a conducting domain wall between polarized and unpolarized $\nu = 2/3$ states. Lithographical length of the gate boundary is 7 μm. Resistance in (a) is measured with $I_{ac} = 1.3$ nA in (b) with $I_{ac} = 0.13\ nA$.

bar under G_2 is unpolarized, the bottom right corner refer as "up" is the region where hall-bar under G_1 is unpolarized and hall-bar under G_2 is polarized. the bottom left corner refer as "pp" is the region where both hall-bar are polarized. In (b) resistance measured across the gate boundary is plotted as a function of both gate voltages. R=0 when both side of the boundary is fully polarized (or fully unpolarized). When polarization of the 2/3 state changes across the gate boundary, R becomes non-zero indicating formation of a conducting channel. Resistance $R \sim 3-5k\ \Omega$ does not depend significantly on the gradient of the density and polarization gradient(up or pu) nor on the magnetic field direction. This is consistent with the formation of a helical domain wall. In the current geometry resistance of the fhDW is not measured directly, within Landauer Büttiker formalism, we extract(10-20)R_q channel resistance for 2-7 μm- long fhDWs with no clear scaling with the length. The lack of scaling may indicate that scattering predominantly occurs in hot spots formed at tri-junctions where fhDW merges with the edge states.

Field evolution of a $7\mu m$ long domain wall in the boundary is shown in figure 4.4.1 . Here, resistance across the boundary R is recorded as a function of ν_1 and ν_2 at different B field, where ν_1 (ν_2) is the filling factor under G_1 (G_2). For $B = 3.8\ T < B^*$ (the lower right corner), the $\nu = 2/3$ state is unpolarized on both side of the boundary. Therefore, even though n_1 and n_2 are slightly different, there is no back scattering between two edges of the FQHE, R is zero in $\nu = 2/3$ state. Similar situation happens when $B > B^*$ on both side of the boundary, where $\nu = 2/3$ is fully polarized, R is zero. By increasing the B field, the center of the spin transition is moving along the diagonal line in the $\nu = 2/3$ plateau from high ν side to the low ν side. Figure 4.4.2 (a) plots the corresponding ν where the center of the DW is located as a function of B field, in which $B = B^*$. Figure 4.4.2 (b) plots the R as a function of B field where ν under both gates are at exact 2/3, from this plot, we can see that the spin phase transition in this device is 4.4 T.

Next we switch to a different coordinate to measure the DW. Previously, we used V_{g1} and V_{g2} to individually control the density n_1 and n_2. Transition from “up” to “pu”(or from “pu” to “up”) cannot be realized by a single scan of V_{g1} or V_{g2}. This time, we define a overall global gate $V_g = 0.61Vg_1 + 0.33V_{g2}$, and density difference Δn is control by $\Delta V_g = 0.39V - g1 - 0.33V_{g2}$. In such a way, the global density on both sides of the boundary is changed by V_g, and the density gradient across the boundary is changed by ΔV_g. Figure

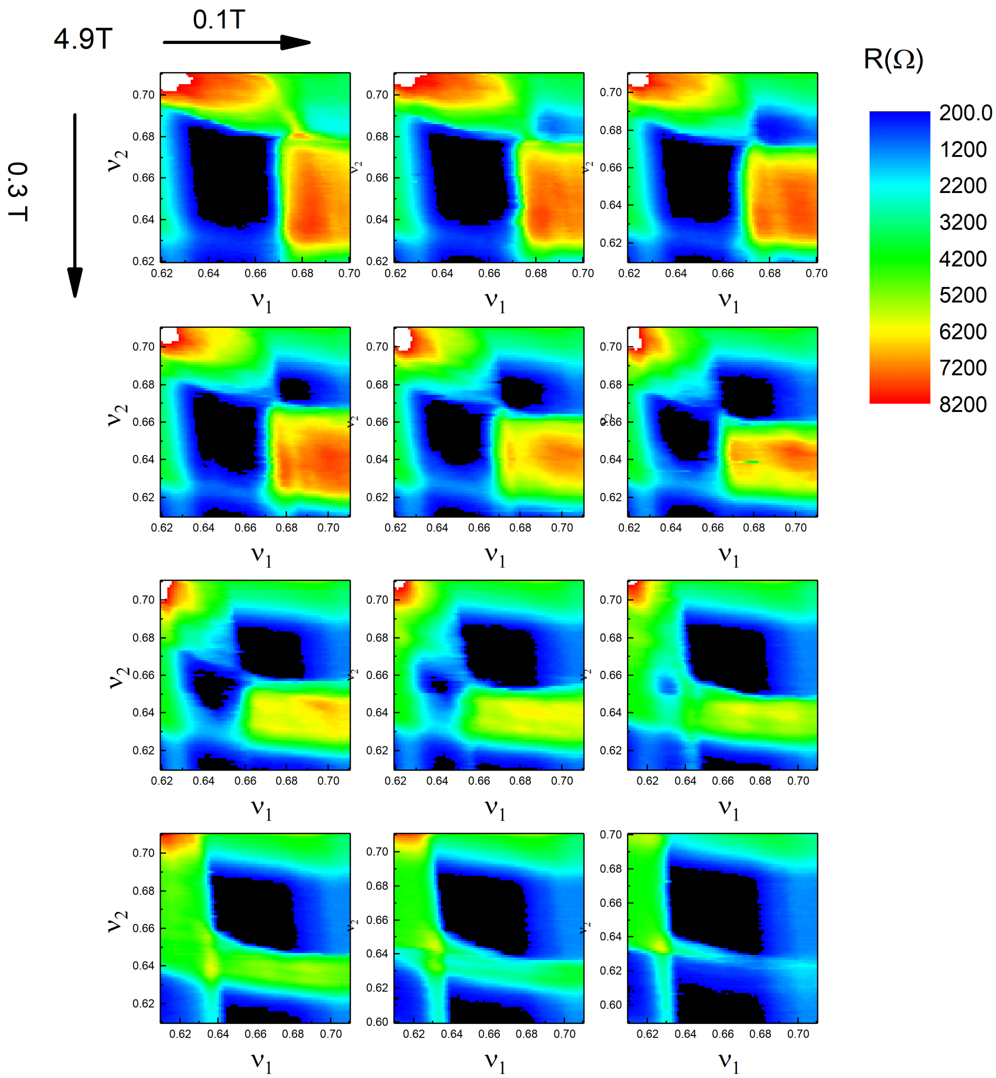

Figure 4.4.1. **Magnetic field evolution of spin transition around $\nu = 2/3$.** (a)Resistance R is measured as a function of filling factor ν_1 and ν_2 under different magnetic field B. The top left corner of the plot is taken in $B = 4.9T$, and the bottom right corner of the plot is taken in $B = 3.8T$, the change between each row is 0.3 T and between each column is 0.1 T.

4.4.3 (a) shows the measurement of R before the transformation and figure 4.4.3 (b) shows the measurement of R after the transformation. Effectively, the plot is rotated by 45°.

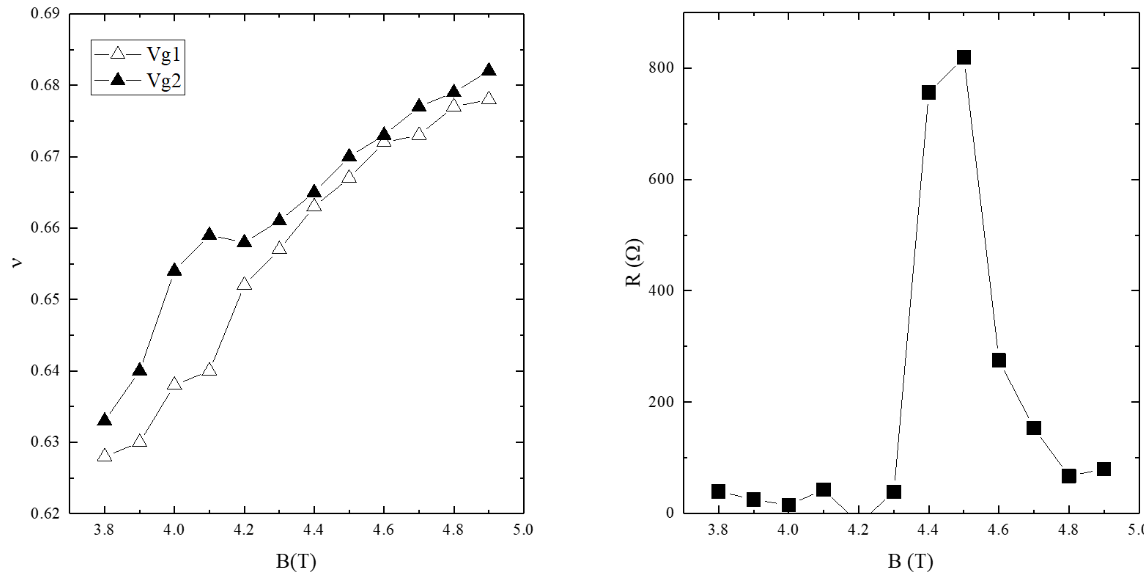

Figure 4.4.2. **Spin transition as a function of B field in $\nu = 2/3$ state.** (a)The shifting of the boundary as a function of B field, at low field $\nu = 2/3$ plateau are fully un-polarized, at high field, $\nu = 2/3$ plateau are fully polarized. (b) Resistance as a function of B at exact $\nu = 2/3$ under both gate. At $B \approx 4.5\ T$, transition occur at $\nu = 2/3$.

4.5 Activation Measurements

Figure 4.5.1 shows the gate dependent of the resistance R_1, R_2 and R using the new coordinate. With fixed $\Delta V_g = -1.5\ mV$, and a fixed field at 4.3 T, when $V_g < -39\ mV$ Hall bar under G_1 is a spin unpolarized $\nu = 2/3$ state, when $V_g > -46 mV$ Hall bar under G_2 is a spin polarized $\nu = 2/3$ state. Therefore when $-46\ mV < V_g < -39\ mV$, a non-vanishing R is observed, indicating the formation of the domain wall within $\nu = 2/3$ plateau. Outside this region, where $V_{g1} < -45\ mV$ and $V_{g2} < -41\ mV$, both sides of the boundary are in polarized $\nu = 2/3$, the R is zero. Same situation happened when $V_{g1} > -45\ mV$ and $V_{g2} > -41\ mV$, both sides of the boundary are in unpolarized $\nu = 2/3$, thus R is zero as well.

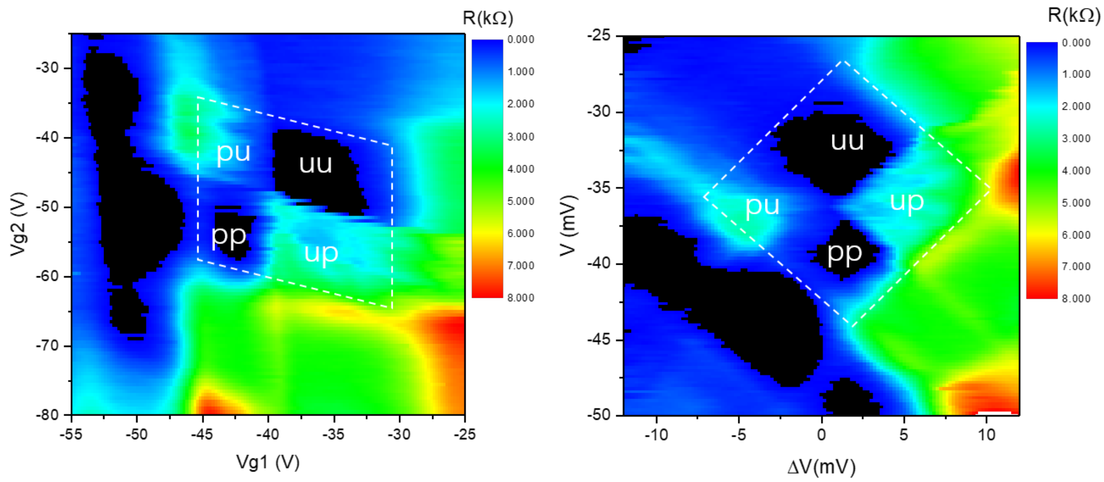

Figure 4.4.3. **Gate and field dependence of spin transition around $\nu = 2/3$.** (a) The measurement of domain wall resistance using V_{g1} and V_{g2} coordinate. (b) The measurement of domain wall resistance using V_g and ΔV_g coordinate.

One of the important prospectives to understand transport property in the domain wall is to study the temperature dependence of the resistance. The resistance across the boundary R is measured as a function of V_g with fixed $\Delta V_g = -1.5\ mV$ and fixed $B = 4.3\ T$ for several temperatures from 18 mK to 272 mK. Figure4.5.2 (b) shows the activation gaps at different gate voltages. The values of the activation gaps are calculated using data extracted from Arrhenius plot with $\ln R(\propto \frac{\Delta}{2k_BT})$ vs $1/T$ at fixed V_g. From the linear fit, the values of the activation gaps are determined. The measurement of activation gaps of the spin transition in $\nu = 2/3$ state has been previously studied [67] by using tilted magnetic field or global gate control to tune the system into a single spin phase transition. In [] the author observed a vanishing resistance peak at the lowest temperature ($T \approx 22\ mK$), they explained that by reducing the temperature, the size of the domain walls is reduced, at low temperature regime, the domains are localized therefore backscattering is suppressed. In our case, the formation of the domain wall is very well defined at the boundary and is robust against density fluctuation and disorder due to a spin polarization difference between each sides of the boundary.

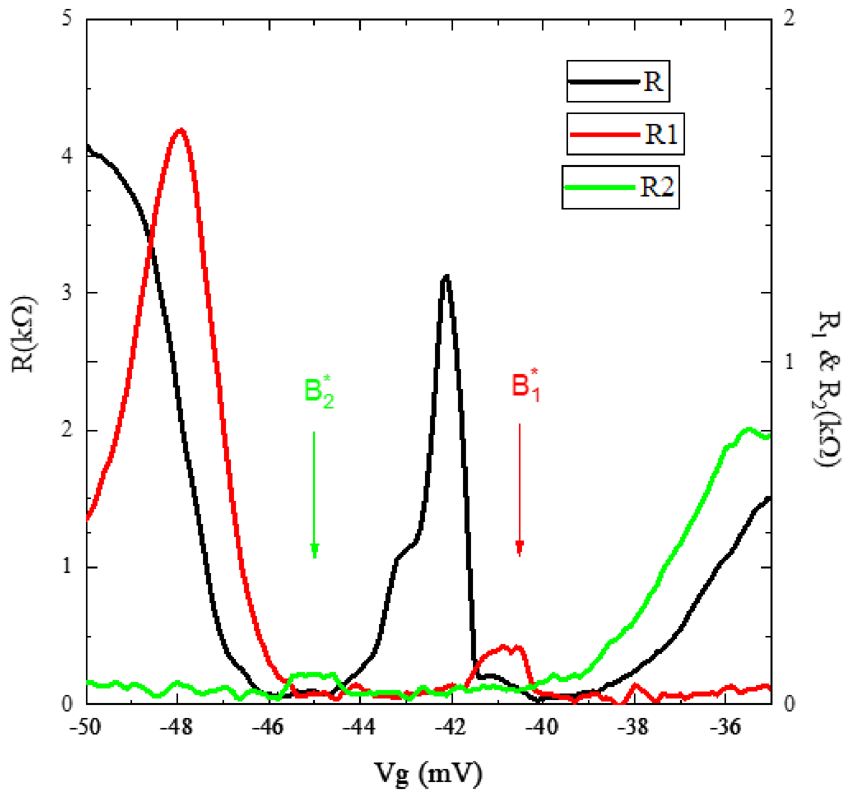

Figure 4.5.1. V_g **dependence of spin transition around** $\nu = 2/3$**.** V_g dependence of spin transition under G_1 (red), under G_2 (green) and across boundary (black).ΔV_g is fixed at -1.5 mV, B=4.3 T.

Another observation in our measurement is the relatively abrupt reduction of the activation gaps within the domain wall. It has been shown experimentally in IQHE where a double quantum well is used [108]. In their experiments, measurements were performed between $\nu = 3$ and $\nu = 4$ where two pseudopin levels crossed, a sharp peak with a reduction in the activation energy was also observed. The author attributed the reduction of the activation gap to the formation of skyrmion which may trapped between the domain wall. These skyrmion which would have low-energy excitation will result in the reduction of the activation gaps.

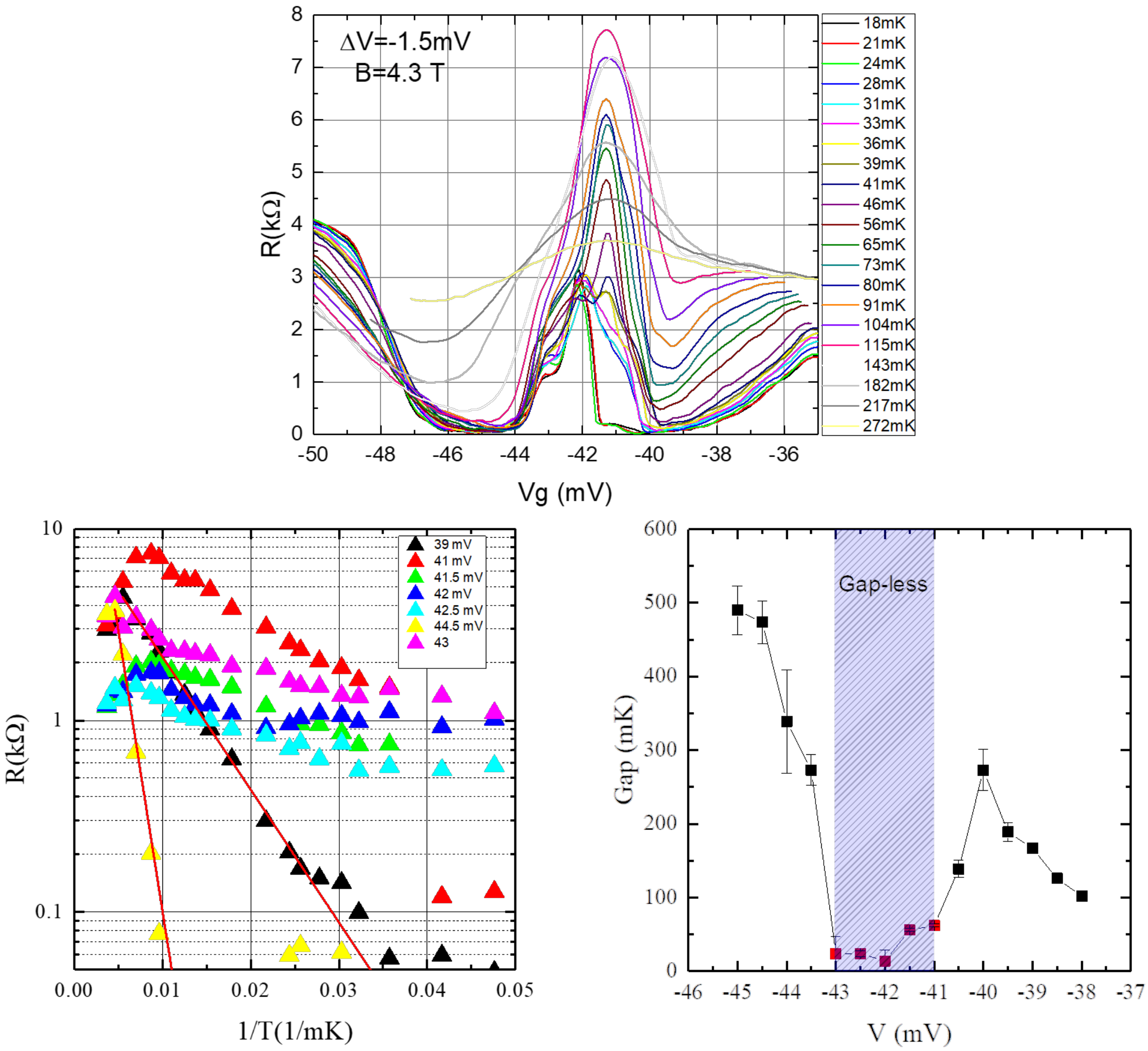

Figure 4.5.2. **Activation gap in the edge states.** (a), V_g dependence of spin transition around $\nu = 2/3$ at different temperatures. ΔV_g is fixed at -1.5 mV, B=4.3 T. (b), activation gap extracted from the temperature dependence of the R at different V_g.

4.6 Spin pumping with DC current

Due to the momentum conservation, the spin flipping process in the transport measured in domain wall has to be mediated by spin-orbit coupling, or electron-nuclear hyperfine

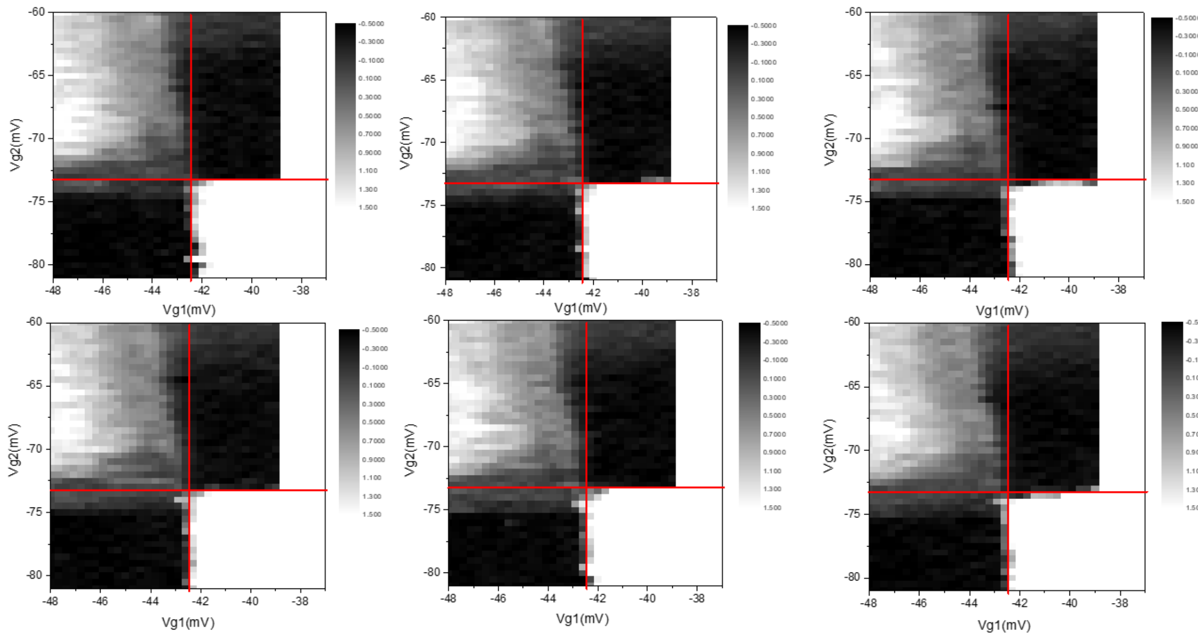

Figure 4.6.1. **stability of the gate dependence of the domain wall.** V_g dependent of spin transition around $\nu = 2/3$. These plots was taken on after another for a total of 90 mintues time period. Red cross indicates the initial boundary of the domain wall, no considerable boundary shifting with times.

interaction. In the previous study of the spin phase transition in IQHE as well as FQHE, it is suggested that the nuclear system takes a crucial role. Next, we'll discuss another interesting phenomenon which arises from the spin pumping within the domain wall.

In these series of measurements, we switch back to the V_{g1}, V_{g2} coordinate and focus on a small region within $\nu = 2/3$ plateau. Before we did the spin pumping measurement, we did a careful check on the stability of the gate dependence of the domain wall. Figure 4.6.1 shows the results for continuous scans which were taken on after another. Each scan took 15 minutes, for a total of 90 minutes time period, there is no considerable boundary shifting with time. This proves the gate stability and reproducibility of the domain wall structure.

Next, we reset our system by reducing both gate voltages to zero and wait for 30 minutes, thus the system is out of the $\nu = 2/3$ regime. This process allows us to relax the spin and therefore initialize the system. Then V_{g1} and V_{g2} are set to an assigned coordinate where

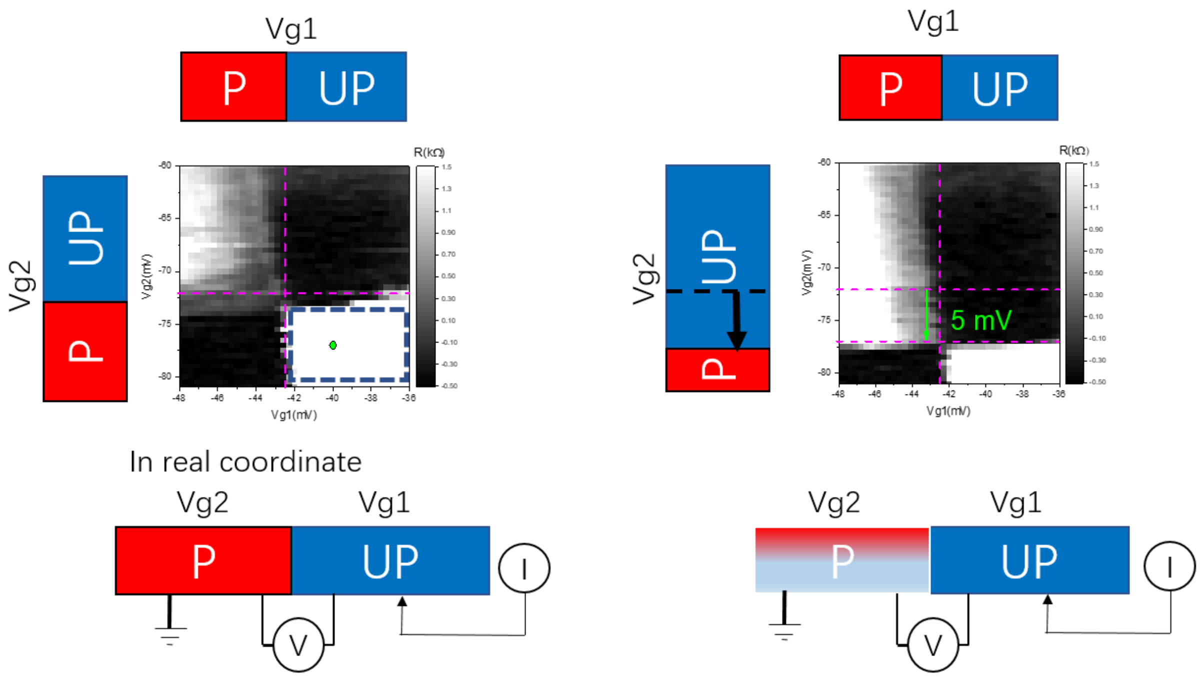

Figure 4.6.2. **Spin pumping in $\nu = 2/3$ domain wall.** (a)Resistance as a function of V_{g1} and V_{g2}, before spin pumping. (b)Resistance as a function of V_{g1} and V_{g2}, after spin pumping.

both gates are tuned within $\nu = 2/3$ plateau, but with different polarizations. A DC current is applied from source to drain and will undergo a polarization change from one side of the domain wall to the other side of the domain wall. Due to the momentum conservation, the spin flipping process in the electron will be mediated by the hyperfine interaction, in which nuclear spin will be polarized as well. After that, the DC current is switched off, and measurement is performed with standard AC lock-in measurement with $I_{ac} = 0.13\ nA$ to investigate the gate dependence of the domain wall boundary after the spin pumping.

Figure 4.6.2 (a) shows the results with spin pumping current $I_{dc} = 0\ nA$ and figure 4.6.2 (b) shows the results with $I_{dc} = 1\ nA$. The schematic drawing in figure 4.6.2 (a) and (b) shows the polarization of the domain in V_{g1} and V_{g2} coordinate. During the spin pumping stage, we set $V_{g1} = -40\ mV$ and $V_{g2} = -77\ mV$ (marked as cyan dot in figure 4.6.2 (a)), so that spin is unpolarized under G_1 and polarized under G_2, as shown in figure 4.6.2 (c)

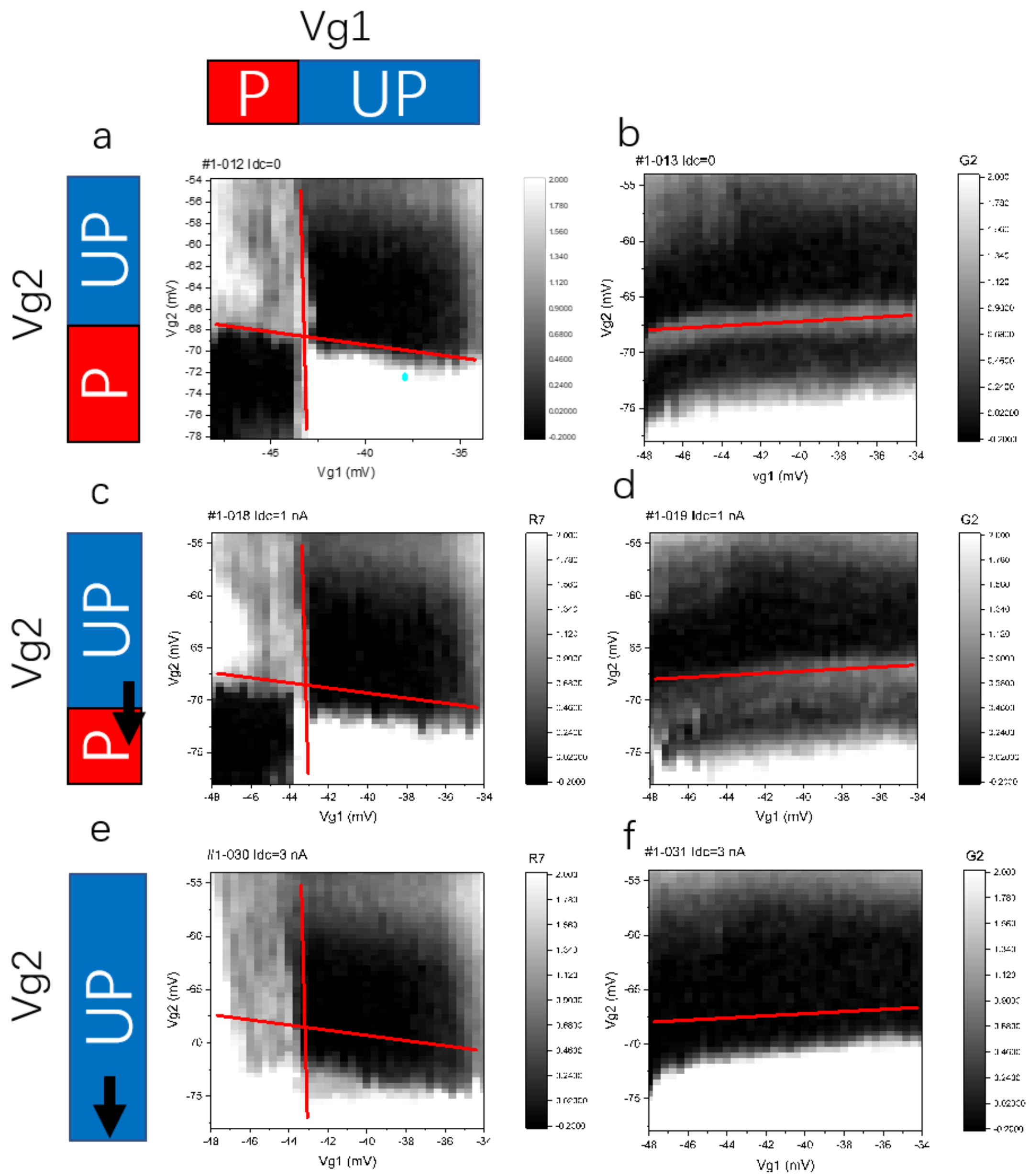

Figure 4.6.3. **Spin pumping in $\nu = 2/3$ domain wall with larger current.** (a), (c), (e)R measured as a function of V_{g1} and V_{g2} after pumping with $I_{dc} = 0, 1, 3$ nA for 40 minutes. (b), (d), (f) R_2 measured as a function of V_{g1} and V_{g2} after pumping with $I_{dc} = 0, 1, 3$ nA for 40 min. Cyan dot represents the point where gate voltage are fixed during the pumping. red cross indicates the domain wall boundary with $I_{dc} = 0$.

bottom. With $I_{dc} = 0nA$, the domain wall boundary remain the same place in V_{g1} and V_{g2} coordinate, as shown in figure 4.6.2 (a). After a $I_{dc} = 1$ nA is applied for 40 minutes, the boundary of V_{g2} is shifting downward by 5 mV. The bottom part of figure 4.6.2 shows the schematic drawing of the device layout and polarization condition in the real coordinate. With the pumping condition mentioned above, the injecting current is unpolarized, after the spin pumping with DC current, the unpolarized region under V_{g2} is enlarged by 5 mV, which corresponding to a reduction of the effective B field under V_{g2}. From the previous experiment of the field evolution of spin transition, we can see that this 5 mV shifting of V_{g2} will correspond to a $B* = 0.2\ T$. In contrast to the shifting of the domain wall boundary with V_{g2}, the boundary of overall $\nu = 2/3$ plateau barely shifts, which can be inferred in the grey region in the upper right corner of the color map.

In order to investigate the polarization mechanism, we perform a more throughout test. This time, after the spin pumping, we measure both R across the boundary as well as R_2 which is R_{xx} under V_{g2}, the results are shown in figure 4.6.3. With different pumping current, the R vs V_{g1} and V_{g2} show qualititatively similar results as previous measurement where the G_2 polarized region within $\nu = 2/3$ is encroached by the unpolarized region. The shifting is more and more downward as the pumping current increased. Remarkably, the polarized region under G_2 also becomes more and more unpolarized, as can be seen in figure 4.6.3 (d), (e), (f). While keep the same pumping time, with large enough pumping current, the 4 sections of the gate-dependent domain wall map become 2 sections, with G_2 always fixed in un-polarized state regardless of the change in V_{g2}, as shown in figure4.6.3 (c) and (f). From the field evolution, as shown in figure 4.4.1, the fully unpolarized state under V_{g2} can be reached when $B < 3.9\ T$, which indicates that the effective $B*$ due to the nuclear polarization is as large as 0.4 T.

Another interesting phenomenon arises from the the spin pumping is shown is figure 4.6.4. During the spin pumping stage, we also record the R as a function of time. With $I_{dc} = 0$, R is stable and no time dependent within the period in which the measurement was performed, this further proves the stability of the domain wall. When a DC current is applied , the R starts to fluctuate over the time. With $I_{dc} = 0.5\ nA$ pumping current, the resistance slowly reduced, when a $I_{dc} = 1\ nA$ pumping current is applied, the resistance drop to zero, which indicates that both sides of the boundary have the similar polarization after

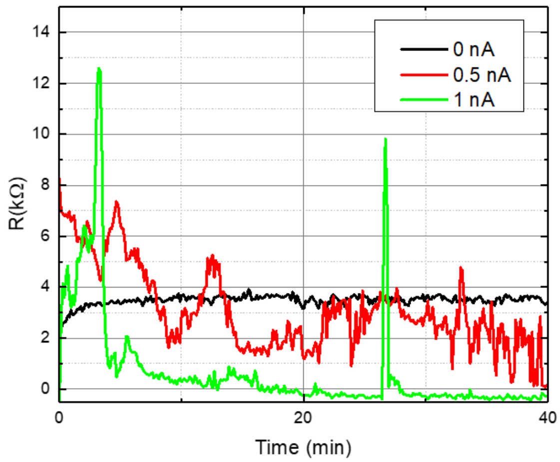

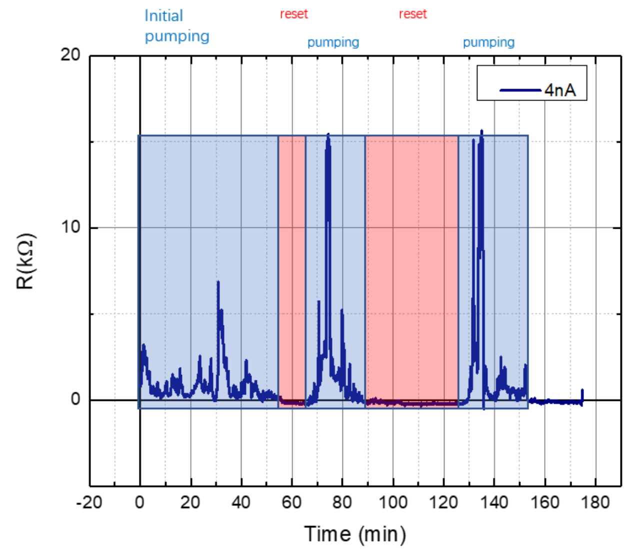

Figure 4.6.4. R **vs time during spin pumping stage with larger pumping current.** (a)Time dependence of R with different pumping currents. Black, red, green line represents pumping with $I_{dc} = 0, 0.51\ nA$ respectively. (b) Time dependence of R with $I_{dc} = 4nA$, blue shadows mark the region during the pumping stage, red shadows mark the region during the reset stage.

pumping for some time, thus the pumping is stopped. The nuclear spin relaxes for some time after the pumping is stopped, then the boundary is shifted back and re-initialized the pumping again. This can be seen more clearly by pumping with $I_{dc} = 4\ nA$ for 175 min, which is shown in figure 4.6.4 (b). The initial pumping takes 52 minutes, then the pumping is switched off automatically due to the boundary shift, and spin relaxation takes place for 10 minutes, the system again forms the domain wall thus restarts the pump. The typical length scale for the spin relaxation is between 10-30 minutes. In reference [109], author observed a relaxation time which is of the order of 10-25 min in GaAs/AlGaAs heterojunction.

4.7 Conclusion

In summary, we propose that domain walls formed during ferromagnetic spin transitions in the fractional quantum Hall effect regime can be used as building blocks to form topological superconductors that support parafermion excitations. We demonstrate that in triangular quantum wells spin transitions can be controlled locally by electrostatic gating and conducting helical domain walls can be formed in multi-gate devices. Such local control allows formation of reconfigurable networks of domain walls. In the presence of proximity-induced superconducting coupling the system becomes a reconfigurable network of one-dimensional topological superconductors with parafermion excitations. With the evolution of the domain wall boundaries with magnetic field as well as spin pumping mechanism, extra control nobs can be added to move the domain walls boundary, thus a on-off switch can be realized in the our domain wall structure. Furthermore, the polarization change due to the spin pumping propagates through all the area under the Hall bar. This may help us to better understand the e-e correlation and thus understand the construction of $\nu = 2/3$ FQHE.

5. SUMMARY AND PERSPECTIVES

5.1 Experimental invetigation of the superconducting contacts in the IQHE and FQHE

The realization of the highly transparent SC/SM interface in GaAs enables investigation of the interplay between superconductivity and states in the integer quantum Hall and fractional quantum Hall regimes. For the integer quantum Hall effect, the lowest Landau level is spin polarized. Reference [25] suggested that additional suppression of the tunneling conductance due to the Pauli exclusion principle may occur, and the tunneling conductance will vanish as a power law of temperature $G \sim T^{4/\nu-2}$ for ν an odd integer. In our preliminary study, the experimental data in Figure2.4.1 contradicts this prediction. Further experiments are needed to demonstrate the tunneling mechanism in these regimes. Recent theoretical work[21] suggests that when a pair of counter-propagating edges modes of a Laughlin fractional quantum Hall state is coupled to a superconductor, a set of fractionalized Majorana modes which exhibit non-Abelian statistics can emerge. A 2π periodicity in the fractional Josephson effect can be measured in such a case. In reference [110], authors suggest that when a superconductor is coupled to the edge of $\nu = 2/3$, transport phenomenon in a SC/SM junction will be modified by the Andreev conversion process. In this process, the outgoing quasihole continues in the same direction around the edge instead of backscattering.

5.2 Experimental investigation of the superconducting contacts in the FQH regime

APPENDICES

Appendix A. Analysis of potential of edge state in IQHE and FQHE

A.1 Analysis of potential of edge state in IQHE

For a sample with uniform density, the longitudinal resistance R_{xx} is zero when the all the area within the Hall-bar has the same integer filling factor. For a sample in which density can be varied, as shown in figure .0.1, with $\nu = n$ on one side of the boundary and $\nu = n+1$ on the other side, the R_{xx} may not always be zero due to the formation of 1D chiral channel between two different filling factors. Let's assume that 4 ohmic contacts are placed at the corner of the sample as shown in figure .0.1, and current i is passed from 1 to 2 and voltage is measured between 3 and 4. Due to the presence of ohmic contacts at 1,2,3,4, the edge states are equilibrated at those points, thus the potential between inner edge and outer edge channel at those point are all the same, from the Kirchhoff's circuit laws we have:

$$\begin{cases} point\ 1 : (n+1)gV_1 - gV_4 - ngV_2 - i = 0 \\ point\ 2 : ngV_2 - ngV_3 = 0 \\ point\ 3 : ngV_4 - ngV_3 = 0 \\ point\ 4 : (n+1)gV_4 - (n+1)gV_1 = 0 \\ potential\ 2 : V_2 = 0. \end{cases}$$

Here, we assign the B field direction in such way that current flows is counterclockwise figure .0.1 (a). Also, in each point the out-going current is positive and incoming current is negative. V_1, V_2, V_3 ,V_4 are the potential of the point 1, 2, 3, 4 ,respectively. $g = \frac{e^2}{h}$ is the conductance quantum, n is the Landau level integer. The first 4 equations are derived from current conservation, summing up of any 3 equations out of these 4 equations will give us the

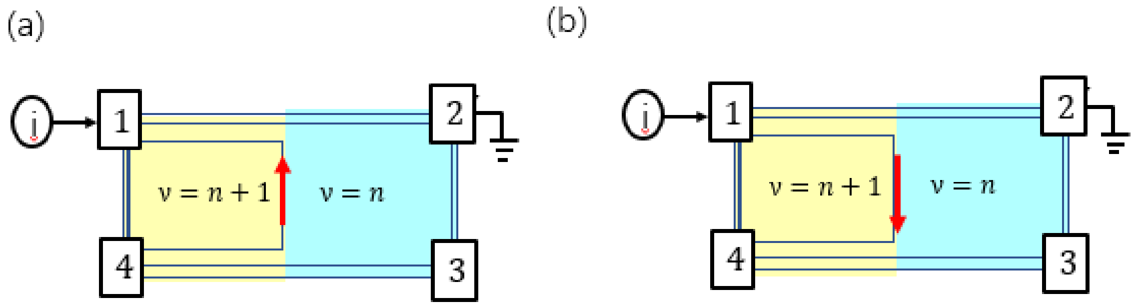

Figure .0.1. **Chiral edge states in IQHE.**

forth one, the last one is the potential of V_2 which is zero in our measurement configuration. In this case:

$$R_{xx} = \frac{V_4 - V_3}{i} = 0. \tag{.0.1}$$

In the opposite B field direction, where current flows clockwise, as shown in figure .0.1 (b) the set of equations can be written as:

$$\begin{cases} point\ 1 : (n+1)gV_1 - (n+1)gV_4 - i = 0 \\ point\ 2 : ngV_2 - ngV_1 = 0 \\ point\ 3 : ngV_3 - ngV_2 = 0 \\ point\ 4 : (n+1)gV_4 - ngV_1 - ngV_3 = 0 \\ potential\ 2 : V_2 = 0. \end{cases}$$

Here, resistance across the boundary:

$$R_{xx} = \frac{V_4 - V_3}{i} = \frac{1}{n(n+1)}\frac{1}{g} = \frac{1}{n(n+1)}\frac{h}{e^2}. \tag{.0.2}$$

By comparing equation .0.1 and equation .0.2, we can see that the resistance R_{xx} across the boundary of different filling factor is B field direction dependent, which is the direct consequence of the chiral channel in the IQHE regime.

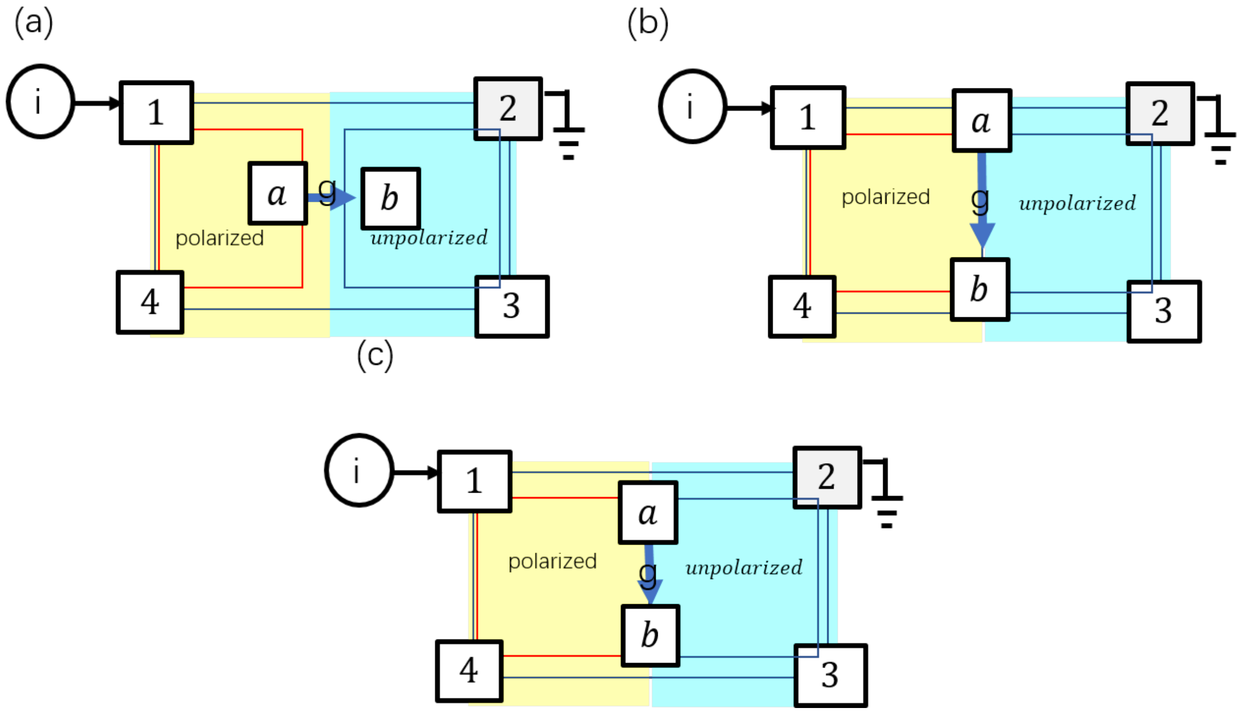

Figure .0.2. **Chiral edge states in IQHE.**

A.2 Analysis of potential of edge state in FQHE

The conductance of an integer quantum Hall state edge is $g = e^2/h$. A fractional quantum Hall state with filling factor $\nu = n/(2np-1)$ can be viewd as composite Fermion liquid with n CF Landau levels being filled and each CF is an electron with 2p vortices attached. For $\nu = 2/3$ states, there are 2 identical edge states, each has a conductance of $g_0 = e^2/3h$ [58, 59].

The schematic view of the device is shown in the figure. The current is injected from contact 1 and drained at contact 2 while voltage is measrued between contacts 3 and 4. The resistance across the domain wall is $R = (V_4 - V_3)/i$. There are two distinct regions: one which is spin polarized where two CFs with spin up are occupied and a spin unpolarized area where there two filled CF levels, on with up and one with spin down.

In the first case the lowest composite Fermion edge goes around the sample, while one spin up edge goes around spin polarized area and one spin down edge goes around spin unpolarized area. from the Kirchhoff's circuit laws we have:

$$\begin{cases} point\ 1: 2gV_1 - 2gV_4 - i = 0 \\ point\ 2: 2gV_2 - gV_1 - gV_b = 0 \\ point\ 3: 2gV_2 - 2gV_3 = 0 \\ point\ 4: 2gV_4 - gV_a - gV_3 = 0 \\ point\ a: gV_a - gV_1 - g_{dw}(V_b - V_a) = 0 \\ point\ b: gV_b - gV_3 - g_{dw}(V_a - V_b) = 0 \\ potential\ 2: V_2 = 0. \end{cases}$$

In this case

$$R = \frac{3(3 + R_{DW})}{2(9 + R_{DW})} \frac{h}{e^2} \tag{.0.3}$$

In the second case the edges hibridized in the domain wall and scattering processes provide resistance:

$$\begin{cases} point\ 1: 2gV_1 - 2gV_4 - i = 0 \\ point\ 2: 2gV_2 - 2gV_a = 0 \\ point\ 3: 2gV_3 - 2gV_2 = 0 \\ point\ 4: 2gV_4 - 2gV_b = 0 \\ point\ a: 2gV_a - 2gV_1 - g_{dw}(V_b - V_a) = 0 \\ point\ b: 2gV_b - 2gV_3 - g_{dw}(V_a - V_b) = 0 \\ potential\ 2: V_2 = 0. \end{cases}$$

In this case

$$R = \frac{9}{6 + 4R_{DW}} \frac{h}{e^2} \tag{.0.4}$$

In the third case, one edge goes around the sample but the ones going near DW hibridize.

$$\begin{cases} point\ 1: 2gV_1 - 2gV_4 - i = 0 \\ point\ 2: 2gV_2 - gV_a - gV_1 = 0 \\ point\ 3: 2gV_3 - 2gV_2 = 0 \\ point\ 4: 2gV_4 - gV_b - gV_3 = 0 \\ point\ a: gV_a - gV_1 - g_{dw}(V_b - V_a) = 0 \\ point\ b: gV_b - gV_3 - g_{dw}(V_a - V_b) = 0 \\ potential\ 2: V_2 = 0. \end{cases}$$

In this case

$$R = \frac{9}{18 + 4R_{DW}} \frac{h}{e^2} \tag{.0.5}$$

Appendix B. LIST OF SAMPLES USED IN THIS THESIS

Table 1.
List of samples used in this thesis.

Sample	n 10^{11}cm^{-2}	μ $10^{6}\text{cm}^{2}/\text{Vs}$	Spacer nm	depth nm	$\Delta B^{*}/\Delta B_{2/3}$	Comment
LE23	2.7	2.4	40	135		used in chapter 3
LE24	1.6	4.1	70	135	1	
LE25	1.3	3.8	110	135	0.14	
LE26			330	135		no ohmic contacts
LE27	0.5	1.6	220	135	0.5	used in chapter 3
LE29			270	135		no ohmic contacts
LE30	0.3	2.1	270	185		
LE34	0.76	4.9	270	185	0.065	unstable $\Delta B^{*}/\Delta B_{2/3}$
LE39	0.8	3.7	270	185	0.7	
LE40	0.8	5	160	135	0.25	used in chapter 4

Appendix C. MATLAB CODES

B.1 BTK model for Andreev reflection Simulation

This code can be used to produce Fig. 1.1.2 a data.

```
clear all
q=1.6E-19;
k=q*8.617E-5;%eV/K
Z=0.1;
TT=4;
x=zeros(1,1001);
Tau = 0.1E-3*q;
for T=TT:0.5:11;
      Delta=(1.6E-3*q)*1.74*sqrt(1-T/12);
Volt=[-5E-3:0.01E-3:5E-3];
for p=1:size(Volt,2)
     V=Volt(p);
     EE=[(-10E-3*q):(1E-5*q):(10E-3*q)];%E<Delta
     n=size(EE,2);
     integrall = 0;
     for tt=1:n-1
          E=EE(tt);

          k=1/2*(1+sqrt(1-(Delta/(E+Tau*1i))^2)/(E+Tau*1i));
          AAA=real(k);
          NNN=imag(k);
```

```
            BBB=1-AAA;
            gg=(AAA+(Z^2)*(AAA-BBB))^2+(NNN*(2*Z^2+1))^2;
            A=sqrt((AAA^2+NNN^2)*(BBB^2+NNN^2))/(gg^2);
            B=(Z^2)*(((AAA-BBB)*Z-2*NNN)^2+(2*NNN*Z+(AAA-BBB))^2)/(gg
                ^2);
            An(tt)=A;
            Bn(tt)= B;
            H=(1+A-B);
            II=0.5*exp((E-q*V)/(k*T))/(k*T*(1+exp((E-q*V)/(k*T)))^2)*H
                ;
            integrall=II*(EE(tt+1)-EE(tt))+integrall;

        end
        An(n)=An(n-1);
        Bn(n)=Bn(n-1);
        Current(p)=integrall;


end
figure(2);
plot(Volt,1./Current);
hold on;
end
```

B.2 CPR simulation

This code can be used to produce Fig. 3.4.2.

```
% constant%
figure
```

```
e=1.6E-19;
hbar=6.55E-16% plank constant ev*s
%V=100E-6;
kB=8.617E-5;%eV/K
T=0.015;  %T of sample
Tc=1.2    % Tc of Al
Tn=1    % transmission
for Tn = 0.2 :0.2 :1
      phi=[0:0.001:pi]    %phase
      delta=1.76*kB*Tc;
      En=delta*sqrt(1-Tn*sin(phi/2).^2) % energy level
      Ic2=100*e.*(delta.^2)/(2.*hbar).*sin(phi).*(Tn./En).*tanh(En
          ./2./kB./T)*10e5;
 Ifit=Ic2


a=1-phi/3.14
plot(a,-Ifit);
plot(phi/3.14,Ifit);
hold on;
end
%Ifit=rot90(Ifit);
xlim([0,1]);
```

B.3 differential resistance calculation and I_C subtraction

This code can be used to subtract I_C in chapter 3.

```
aa=diff(transpose(InAs028));
xx=aa(140:280,1:181);
```

```
dInAs426=transpose(xx);
%dInAs426=smooth(10,'sgolay')
%%
dVth=0.25;
dI=0.5;
j0=1;
Ic=zeros(length(dInAs426(:,1)));
for n = 1:length(dInAs426(:,1))
    j=1;
    for tt=1:length(dInAs426(1,:))
        if (dInAs426(n,j)<dVth )
            j=j+1;
                end
        end;
    Ic(n)=(j-j0)*dI;
end
Ic2=Ic(:,1);
```

REFERENCES

REFERENCES

[1] T. D. Clark, R. J. Prance, and A. D. C. Grassie, Journal of Applied Physics **51**, 2736 (1980).

[2] H. Takayanagi and T. Kawakami, Phys. Rev. Lett. **54**, 2449 (1985).

[3] T. Akazaki, H. Takayanagi, J. Nitta, and T. Enoki, Applied Physics Letters **68**, 418 (1996).

[4] H. B. Heersche, P. Jarillo-Herrero, J. B. Oostinga, L. M. K. Vandersypen, and A. F. Morpurgo, Nature **446**, 56 (2007).

[5] B. Sacépé et al., Nat. Commun. **2**, 575 (2011).

[6] J. R. Williams et al., Physical Review Letters **109**, 056803 (2012).

[7] M. Veldhorst et al., Nat. Mater. **11**, 1 (2012).

[8] F. Qu et al., Sci. Rep. **2**, 339 (2012).

[9] V. S. Pribiag et al., Nat Nano **10**, 593 (2015).

[10] Y.-J. Doh et al., Science **309**, 272 (2005).

[11] P. Jarillo-Herrero, J. A. van Dam, and L. P. Kouwenhoven, Nature **439**, 953 (2006).

[12] J. Xiang, A. Vidan, M. Tinkham, R. Westervelt, and C. Lieber, Nature Nanotechnology **1**, 208 (2006).

[13] S. Hart et al., Nat. Phys **10**, 638 (2014).

[14] W. Yu et al., Appl. Phys. Lett. **105**, 192107 (2014).

[15] L. P. Rokhinson, X. Liu, and J. K. Furdyna, Nat. Phys. **8**, 795 (2012).

[16] V. Mourik et al., Science **336**, 1003 (2012).

[17] L. Fu and C. L. Kane, Phys. Rev. B **79**, 161408 (2009).

[18] R. M. Lutchyn, J. D. Sau, and S. D. Sarma, Phys. Rev. Lett. **105**, 077001 (2010).

[19] J. Alicea, Phys. Rev. B **81**, 125318 (2010).

[20] D. J. Clarke, J. Alicea, and K. Shtengel, Nat. Commun. **4**, 1348 (2012).

[21] R. S. K. Mong et al., Phys. Rev. X **4**, 011036 (2014).

[22] Z.-W. Zuo, L. Sheng, and D. Xing, Solid State Communications **184**, 17 (2014).

[23] E. M. Stoudenmire, D. J. Clarke, R. S. K. Mong, and J. Alicea, Phys. Rev. B **91**, 235112 (2015).

[24] J. Alicea and P. Fendley, Annual Review of Condensed Matter Physics **7**, 119 (2016).

[25] M. P. A. Fisher, Phys. Rev. B **49**, 14550 (1994).

[26] K.-M. H. Lenssen et al., Applied Physics Letters **63**, 2079 (1993).

[27] T. D. Moore and D. A. Williams, Phys. Rev. B **59**, 7308 (1999).

[28] A. Verevkin et al., semiconductors **33**, 551 (1999).

[29] H. Takayanagi, T. Akazaki, M. Kawamura, Y. Harada, and J. Nitta, Physica E **4**, 922 (2002).

[30] J. Kutchinsky, R. Taboryski, C. B. Srensen, J. B. Hansen, and P. E. Lindelof, Physica C: Superconductivity **352**, 4 (2001).

[31] A. Marsh, D. A. Williams, and H. Ahmed, Phys. Rev. B **50**, 8118 (1994).

[32] J. Bardeen, L. N. Cooper, and J. R. Schrieffer, Phys. Rev. **106**, 162 (1957).

[33] A. Andreev, Sov. Phys. JETP **19**, 1228 (1964).

[34] G. E. Blonder, M. Tinkham, and T. M. Klapwijk, Phys. Rev. B **25**, 4515 (1982).

[35] T. Klapwijk, Journal of Superconductivity **17**, 593 (2004).

[36] T. Schäpers, *Superconductor/semiconductor junctions*, volume 174, Springer, 2001.

[37] H. Takayanagi and T. Akazaki, Physica B: Condensed Matter **249**, 462 (1998).

[38] ChangW. et al., Nat. Nano **10**, 232 (2015).

[39] J. Shabani et al., Physical Review B **93**, 155402 (2015).

[40] M. K. Ma et al., Physical Review B **96**, 241301 (2017).

[41] K. I. Bolotin, F. Ghahari, M. D. Shulman, H. L. Stormer, and P. Kim, Nature **475**, 122 (2011).

[42] K. V. Klitzing, G. Dorda, and M. Pepper, Phys. Rev. Lett. **45**, 494 (1980).

[43] B. Kramer and A. MacKinnon, Localization: theory and experiment, 1993.

[44] J. T. Chalker, P. Carra, and K. A. Benedict, Europhys. Lett. **5**, 163 (1988).

[45] R. B. Laughlin, Phy. Rev. B **23**, 5632 (1981).

[46] M. Büttiker, Phy. Rev. B **38**, 9375 (1988).

[47] T. Heinzel, *Mesoscopic Electronics in Solid State Nanostructures*, Wiley-VCH Verlag GmbH Co. KGaA, Weinheim, 2007.

[48] Supriyo Datta, *Quantum Transport*, Cambridge University Press, 1995.

[49] D. C. Tsui, H. L. Stormer, and A. C. Gossard, Phys. Rev. Lett. **48**, 1559 (1982).

[50] J. K. Jain, prl **63**, 199 (1989).

[51] B. I. Halperin, P. A. Lee, and N. Read, prb **47**, 7312 (1993).

[52] V. J. Goldman, B. Su, and J. K. Jain, prl **72**, 2065 (1994).

[53] R. L. Willett, R. R. Ruel, K. W. West, and L. N. Pfeiffer, prl **71**, 3846 (1993).

[54] M. D. Johnson and A. H. MacDonald, Phys. Rev. Lett. **67**, 2060 (1991).

[55] C. L. Kane, M. P. A. Fisher, and J. Polchinski, Phys. Rev. Lett. **72**, 4129 (1994).

[56] A. Bid et al., Nature **466**, 585 (2010).

[57] V. Venkatachalam, S. Hart, L. Pfeiffer, K. West, and A. Yacoby, Nat Phys **8**, 676 (2012).

[58] C. W. J. Beenakker, Phys. Rev. Lett. **64**, 216 (1990).

[59] R. Sabo et al., Nature Physics **13**, 491 (2017).

[60] S. Sondhi, A. Karlhede, S. Kivelson, and E. Rezayi, Phys. Rev. B **47**, 16419 (1993).

[61] S. E. Barrett, G. Dabbagh, L. N. Pfeiffer, K. W. West, and R. Tycko, Phys. Rev. Lett. **74**, 5112 (1995).

[62] E. H. Aifer, B. B. Goldberg, and D. A. Broido, Phys. Rev. Lett. **76**, 680 (1996).

[63] G. Gervais et al., Phys. Rev. Lett. **94**, 196803 (2005).

[64] Tapash and F. C. Zhang, Physical Review B **29**, 7032 (1984).

[65] V. M. Apalkov, T. Chakraborty, P. Pietiläinen, and K. Niemelä, Physical Review Letters **86**, 1311 (2001).

[66] R. G. Clark, J. R. M. P. A. W. J. J. H. S. R. Haynes, A. M. Suckling, and C. T. Foxon, Phys. Rev. Lett. **62**, 1536 (1989).

[67] L. W. Engel, S. W. Hwang, T. Sajoto, D. C. Tsui, and M. Shayegan, Phys. Rev. B **45**, 3418 (1992).

[68] J. P. Eisenstein, H. L. Stormer, L. N. Pfeiffer, and K. W. West, Phys. Rev. B **41**, 7910 (1990).

[69] I. V. Kukushkin, K. v. Klitzing, and K. Eberl, Phys. Rev. Lett. **82**, 3665 (1999).

[70] J. H. Smet, R. A. Deutschmann, W. Wegscheider, G. Abstreiter, and K. von Klitzing, Phys. Rev. Lett. **86**, 2412 (2001).

[71] S. Melinte et al., PRL **84**, 354 (2000).

[72] M. Stern et al., Phys. Rev. Lett. **108**, 066810 (2012).

[73] O. I. Stern, *Spin Phenomena in the Fractional Quantum Hall Effect: NMR and Magnetotransport Studies*, PhD thesis, Physik der Universitt Stuttgart, 2005.

[74] A. Kazakov et al., Phys. Rev. Lett. **119**, 046803 (2017).

[75] Calculations were performed using G. L. Sniders 1D Poisson solver.

[76] G. L. Snider, I.-H. Tan, and E. L. Hu, J. Appl. Phys. **68**, 2849 (1990).

[77] D. M. Glowacka et al., Development of a NbN deposition process for superconducting quantum sensors, 2014.

[78] I. Kulik and A. Omel'yanchuk, Sov. J. Low Temp. Phys. **3**, 459 (1977).

[79] I. Kulik and A. Omel'yanchuk, Sov. Phys. JETP **21**, 96 (1975).

[80] P. F. Bagwell, Phys. Rev. B **46**, 12573 (1992).

[81] W. Haberkorn, H. Knauer, and J. Richter, Physics Status Solidi **47**, K161 (1978).

[82] J. Gao et al., Surface Science **305**, 470 (1994).

[83] X. Shi, W. Yu, S. D. Hawkins, J. F. Klem, and W. Pan, Applied Physics Letters **107**, 052601 (2015).

[84] J. M. Rowell and W. L. McMillan, Phys. Rev. Lett. **16**, 453 (1966).

[85] J. D. Sau, S. Tewari, and S. Das Sarma, Phys. Rev. B **85**, 064512 (2012).

[86] K. Neurohr et al., Phys. Rev. B **54**, 17018 (1996).

[87] D. J. Clarke, J. Alicea, and K. Shtengel, Nat Phys **10**, 877 (2014).

[88] A. Y. Kitaev, Physics-Uspekhi **44**, 131 (2001).

[89] J. Sau, R. Lutchyn, S. Tewari, and S. Das Sarma, Physical Review Letters **104**, 040502 (2010).

[90] S. M. Albrecht et al., Physical Review Letters **118**, 137701 (2017).

[91] W. Chang et al., Nature Nanotechnology **10**, 232236 (2015).

[92] T. Karzig et al., (2016).

[93] B. Shojaei et al., Physical Review B **94**, 245306 (2016).

[94] J. Kutchinsky, R. Taboryski, C. B. Sørensen, J. B. Hansen, and P. E. Lindelof, Phys. Rev. Lett. **83**, 4856 (1999).

[95] A. C. C. Drachmann et al., Nano Letters **17**, 1200 (2017).

[96] M. Kjaergaard et al., Nature Communications **7**, 12841 (2016).

[97] M. Kjaergaard et al., Physical Review Applied **7**, 034029 (2017).

[98] G. Giuliani and G. Vignale, *Quantum theory of the electron liquid*, Cambridge Univeristy Press, 2005.

[99] M. Baraban, N. E. Bonesteel, and S. H. Simon, Phys. Rev. A **81**, 062317 (2010).

[100] P. Fendley, J. Stat. Mech. , P11020 (2012), arXiv:1209.0472.

[101] J. Maciejko, T. L. Hughes, and S.-C. Zhang, Annual Review of Condensed Matter Physics **2**, 31 (2011).

[102] M. Z. Hasan and J. E. Moore, Annual Review of Condensed Matter Physics **2**, 55 (2011).

[103] Y. Oreg, G. Refael, and F. von Oppen, Phys. Rev. Lett. **105**, 177002 (2010).

[104] V. Fal'ko and S. Iordanskii, Phys. Rev. Lett. **84**, 127 (2000).

[105] G. E. Simion, A. Kazakov, L. P. Rokhinson, T. Wojtowicz, and Y. B. Lyanda-Geller, Disorder-generated non-abelions, 2017.

[106] B. Verdene et al., Nat Phys **3**, 392 (2007).

[107] J. Hayakawa, K. Muraki, and G. Yusa, Nature Nanotechnology **8**, 31 (2012).

[108] T. Machida, T. Yamazaki, and S. Komiyama, Applied Physics Letters **80**, 4178 (2002).

[109] A. V. Shchepetilnikov et al., PHYSICAL REVIEW B **96** (2017).

[110] D. J. Clarke, J. Alicea, and K. Shtengel, Nat. Phys. **10**, 877 (2014).

VITA

VITA

Zhong Wan

Department of Physics and Astronomy, Purdue University, 525 Northwestern Avenue, West Lafayette, IN, 47906, USA

Education

Ph.D. Degree Program (2011-2018), Department of Physics, Purdue University, USA

B.S. Degree Program (2007-2011), Department of Physics, JiLin University, China

Employment

2012-2018 Research Assistant, Department of Physics, Purdue University

2011-2012 Teaching Assistant, Department of Physics, Purdue University

Publications

1. Z. Wan, A. Kazakov, M. J. Manfra, L. N. Pfeiffer, K. West, L. P. Rokhinson, Induced superconductivity in high-mobility two-dimensional electron gas in gallium arsenide heterostructures, Nature Communications **6**, 7426 (2015).

2. T. Wu, Z. Wan, A. Kazakov, Y. Wang, G. Simion, J. Liang, K. West, K. Baldwin, L. N. Pfeiffer, Y. Lyanda-Geller, L. P. Rokhinson, Parafermion supporting platform based on spin transitions in the fractional quantum Hall effect regime, submitted to PRB.

3. K. Ramadoss, M. Mandal, X. Dai, Z. Wan, Y. Zhou, L. P. Rokhinson, Y. P. chen, J. Hu, S. Ramanathan, Sign reversal of magnetoresistance in a perovskite nickelate by electron doping, Phys. Rev. B **94**, 235124, (2016)

3. B. Yi, X. Chen, K. Guo, Z. Wan, Q. Qian, H. Yan and J. Chen, Gelatin-based Activated Carbon with Carbon Nanotubes as Framework for Electric Double-Layer Capacitors, J. Porous Mat. **19**, 37 (2012).

4. X. Liu, Z. Wan, Q. Qian, X. Han and J. Wang, Coating with Al_2O_3-SiO_2-B_2O_3 Film on Diamond Surface in Sol-Gel Method, Super Hard Material Engineering (in Chinese) **23**, 5 (2011).

5. W. Hu, L. Wan, X. Liu, M. Chen, Z. Wan and Q. Qian, Preparation and Properties of Diamond Surface Coating with TiO_2/Al_2O_3 Film, Journal of the Chinese Ceramic Society (in Chinese) **39**, 829 (2011).